UNIVERSITY OF CALIFORNIA

Santa Barbara

The Effect of (Counter-)ions on the Electronic and Crystalline Structure of Doped Polymeric Semiconductors

A dissertation submitted in partial satisfaction of the

requirements for the degree Doctor of Philosophy

in Materials

by

Elayne Morgan Thomas

Committee in charge:

Professor Michael L. Chabinyc, Co-chair

Professor Rachel A. Segalman, Co-chair

Professor Glenn H. Fredrickson

Professor Stephen D. Wilson

December 2019

The dissertation of Elayne Morgan Thomas is approved.

_____

Stephen D. Wilson

_____

Glenn H. Fredrickson

_____

Rachel A. Segalman, Committee Co-chair

_____

Michael L. Chabinyc, Committee Co-chair

December 2019

The Effect of (Counter-)ions on the Electronic and Crystalline Structure of

Doped Polymeric Semiconductors

Elayne Morgan Thomas

ACKNOWLEDGEMENTS

To my parents, who gave me every chance to realize my full potential.

VITA OF ELAYNE MORGAN THOMAS
December 2019

EDUCATION

University of California, Santa Barbara — December 2019
Santa Barbara, CA
Doctor of Philosophy in Materials

University of Michigan College of Engineering — May 2015
Ann Arbor, MI
Bachelor of Science in Materials Science and Engineering

AWARDS AND HONORS

2017 – 2019 (x3) **Travel Fellowship**
Dow Materials Institute & UCSB Materials Research Laboratory

2017 – 2019 **NSF Graduate Research Fellowship**
National Science Foundation

2017 **Science and Engineering Graduate Fellowship**
American Society for Engineering Education

2016 **Best Poster Award**
Materials Research Outreach Symposium (MROP)

2014 **Union Plus Scholarship**
American Federation of Government Employees

2013 **Brian Worth Memorial Scholarship**
University of Michigan

PUBLICATIONS

1. Peterson, K. A., **Thomas, E. M.**, and Chabinyc, M. L. Thermoelectric Properties of Semiconducting Polymers. *Annu. Rev. Mater. Sci.* Submitted.
2. Rawlings, D., **Thomas, E. M.**, Chabinyc, M. L., and Segalman, R. A. Controlling the Doping Mechanism in Thin Film Transistors Through Design of Polymeric Ionic Liquid-gate Dielectrics. *Chem. Mater.* (**2019**) 31, 8820-8829. DOI: 10.1021/acs.chemmater.9b02803
3. Mazaheripour, A., **Thomas, E. M.**, Segalman, R. A., and Chabinyc, M. L. Nonaggregating Doped Polymers Based on Poly(3,4-Propylenedioxythiophene). *Macromolecules* (**2019**) 52, 2203-2213. DOI: 10.1021/acs.macromol.8b02389

4. **Thomas, E. M.**, Davidson, E. C., Katsumata, R., Segalman R. A., and Chabinyc, M. L. Branched Side Chains Govern Counterion Position and Doping Mechanism in Conjugated Polythiophenes. *ACS Macro Letters* (**2018**) 7, 1492−1497. DOI: 10.1021/acsmacrolett.8b00778
5. Bridges, C. R., Ford, M. J., **Thomas, E. M.**, Gomez, C., Bazan, G. C., and Segalman, R. A. Effects of Side Chain Branch Point on Self Assembly, Structure, and Electronic Properties of High Mobility Semiconducting Polymers. *Macromolecules* (**2018**) 51, 8597−8604. DOI: 10.1021/acs.macromol.8b01906
6. **Thomas, E. M.**, Brady, M. A., Nakayama, N., Popere, B. C., Segalman R. A., and Chabinyc, M. L. X-ray Scattering Reveals Ion-induced Microstructural Changes During Electrochemical Gating of Poly(3-hexylthiophene). *Adv. Funct. Mater.* (**2018**) 28, 1803687. DOI: 10.1002/adfm.201803687
7. Mazaheripour, A. M., Majumdar, S., Hanemann-Rawlings, D., **Thomas, E. M.**, McGuiness C., d'Alecon, L., Chabinyc, M. L., and Segalman, R. A. Tailoring the Seebeck Coefficient of PEDOT:PSS by Controlling Ion Stoichiometry in Ionic Liquid Additives. *Chem. Mater.* (**2018**) 30, 4816-4822. DOI: 10.1021/acs.chemmater.8b02114
8. **Thomas, E. M.**, Popere, B. C., Fang, H., Chabinyc, M. L., and Segalman, R. A. Role of Disorder Induced by Doping on the Thermoelectric Properties of Semiconducting Polymers. *Chem. Mater.* (**2018**) 30, 2965-2972. DOI: 10.1021/acs.chemmater.8b00394
9. Popere, B. C., Sanoja, G. E., **Thomas, E. M.**, Schauser, N. S., Jones, S. D., Bartels, J. M., Helgeson, M. E., Chabinyc, M. L., and Segalman, R. A. Photocrosslinking Polymeric Ionic Liquids *via* Anthracene Cycloaddition for Organic Electronics. *J. Mater. Chem. C.* (**2018**) 6, 8762. DOI: 10.1039/C8TC02561D
10. Patel, S. N., Glaudell, A. M., Peterson, K. A., **Thomas, E. M.**, O'Hara, K. A., Lim, E., and Chabinyc, M. L. Morphology Controls the Thermoelectric Power Factor of a Doped Semiconducting Polymer. *Sci. Adv.* (**2017**) 3, e1700434. DOI: 10.1126/sciadv.1700434
11. Fang, H.*, Popere, B. C.*, **Thomas, E. M.**, Mai, C.-K., Chang, W. B., Bazan, G. C., Chabinyc, M. L., and Segalman, R. A. Large-scale Integration of Flexible Materials into Rolled and Corrugated Thermoelectric Modules. *J. Appl. Polym. Sci.* (**2016**) 134, 44208. (* = equal contribution) DOI: 10.1002/app.44208
12. Sambur, J. B., Chen, T. Y., Choudhary, E., Chen, G., Nissen, E. J., **Thomas, E. M.**, Zou, N., and Chen, P. Sub-particle Reaction and Photocurrent Mapping to Optimize Catalyst-modified Photoanodes. *Nature* (**2016**) 530, 77. DOI: 10.1038/nature16534

ORAL PRESENTATIONS

E. M. Thomas, "The impact of counter-ions on the structure and doping mechanism of polymeric semiconductors", *Invited Speaker*, Harvey Mudd College Seminar, Claremont CA (2019).

E. M. Thomas, "Branched side chains control the counter-ion position and doping mechanism in conjugated polythiophenes", American Physical Society (APS) March Meeting, Boston MA (2019).

E. M. Thomas, "Operando X-ray scattering reveals ion-induced structural changes during electrochemical gating of poly(3-hexylthiophene)", Materials Research Society (MRS) Fall Meeting, Boston MA (2018).

E. M. Thomas, "Correlation between microstructural changes and electrical properties in doped organic semiconductors using in operando X-ray scattering", American Physical Society (APS) March Meeting, Los Angeles CA (2018).

E. M. Thomas, "Structural changes in doped organic semiconductors observed in operando using polymeric ionic liquids", Materials Research Society (MRS) Fall Meeting, Boston MA (2017).

E. M. Thomas, "Exploring ionic effects in disorder and charge transport of organic thermoelectrics", Chalmers/UCSB Colloqium, Goteborg Sweden (2017).

E. M. Thomas, "Effect of ions on structure and charge transport in organic thermoelectrics", *Invited Speaker*, Southern School of Computational Chemistry and Materials Science, Jackson MI (2017).

E. M. Thomas, "Thermoelectric charge transport in organic semiconductors using polymerized ionic liquid gate dielectrics", American Physical Society (APS) March Meeting, New Orleans LA (2017).

E. M. Thomas, "Probing thermoelectric transport in organic semiconductors using polymerized ionic liquids", Materials Research Society (MRS) Fall Meeting, Boston MA (2016).

E. M. Thomas, "Gated seebeck using polymerized ionic liquid gate dielectrics", American Physical Society (APS) March Meeting, Baltimore MD (2016).

POSTER PRESENTATIONS

Using Polymeric Ionic Liquids to Observe Structural Changes in Doped Semiconductors in operando, Materials Research Outreach Symposium, Santa Barbara CA (February 2018).

Thermoelectric Charge Transport in Organic Semiconductors Using Polymerized Ionic Liquids, International Summer School on Thermoelectrics, Golden CO (July 2016).

Gated Seebeck Using Polymerized Ionic Liquid Gate Dielectrics, Materials Research Outreach Symposium, Santa Barbara CA (January 2016).

TECHNICAL SKILLS

Structural and surface-sensitive characterization: XRD, WAXS, SAXS, RSoXS, NEXAFS, XPS
Electronic characterization: mobility, thermopower, Fermi level, carrier concentration

Spectroscopic characterization: UV-visible absorbance spectroscopy, fluorescence spectroscopy, FTIR spectroscopy, X-ray photoelectron spectroscopy, Raman spectroscopy, NMR spectroscopy, secondary ion mass spectroscopy
Microscopy: scanning electron microscopy, atomic force microscopy
Clean-room characterization: thermal and E-beam evaporation, photolithography, microfabrication
Computer software: Igor, MATLAB, Mathematica, Adobe Illustrator

ABSTRACT

The Effect of (Counter-)ions on the Electronic and Crystalline Structure of Doped Polymeric Semiconductors

by

Elayne Morgan Thomas

Polymeric semiconductors show potential as materials for electronic applications unrealizable by inorganic semiconductors, such as wearable and biocompatible devices. An important process to increase the electrical conductivity in polymers is through doping, where small molecules infiltrate the material to oxidize or reduce the polymeric backbone. Once the reaction takes place, the dopant molecule becomes ionized. A central concept that is not understood in polymeric semiconductors today is how these counter-ions and electrons (or holes) interact when in close proximity to one another, and how those interactions affect their respective conduction mechanisms. Additionally, the semi-crystalline nature of most semiconducting polymers complicates the relationship between morphology and electronic conduction.

We aim to develop a better understanding of ionic effects on the electronic and morphological properties of semiconducting polymers using a combination of spectroscopic measurements, X-ray scattering, and electrical characterization. From this work, we find that the presence of dopant counter-ions manifest throughout a multitude of length scales that partially govern the electronic behavior at the device scale. This work indicates that significant differences exist between a doped polymer and its insulating state, signifying the importance of integrating doping-induced disorder into transport models for organic semiconductors.

TABLE OF CONTENTS

Chapter 1

Introduction

The mobile phone, arguably one of the powerful inventions in modern history, utilizes all facets of materials science and engineering. Metals, like aluminum alloys, create the phone housing lightweight but durable for prolonged use. Dielectric ceramics provide the inductors, antennas, and radiofrequency components for device connectivity to wireless networks and cell towers. Traditionally, elastic polymers like rubbers are used to protect the device from scratches and cracks. However, recent advances in display technologies have created a new haven for organic materials in electronics: the screen. Organic light-emitting diodes (OLEDs) have enabled features previously unimaginable with other displays, evidenced by the first foldable smart phone produced by Samsung in February of 2019.[1] This sub-class of materials is known as organic semiconductors.

Since organic semiconductors often rely on vacuum techniques for deposition, alternative materials are desired that exhibit similar properties but are easily processed. Polymeric semiconductors can be synthetically tailored to offer solution processability in a variety of solvents, which opens the door to scalable and low-cost deposition techniques like ink-jet printing and blade coating.[2] Additionally, carbon-based semiconductors are inherently more biocompatible than inorganic semiconductors, which motivates research efforts focusing on their use in wearable and implantable bioelectronics and sensors.[3,4] Polymeric

semiconductors yield promise not as an alternative to crystalline silicon, but as an active material in applications previously unrealizable with inorganic semiconductors.

Organic semiconductors can also conduct ions and electrons simultaneously. Ion-conducting polymers been widely studied within the battery community for all-polymer charge storage devices.[5] However, as explained within the following sections, the presence of counter-ions is necessary for polymers to stably conduct electricity and maintain charge neutrality within the material. Mixed transport is therefore essential to create a stable conducting polymer. A fundamental concept that is not understood in polymeric semiconductors today is how these counter-ions and electrons (or holes) interact when in close proximity to one another, and how those interactions affect their respective conduction mechanisms.

The studies detailed within this Dissertation aim to develop a better understanding of ionic effects on the electronic and morphological properties of semiconducting polymers. The remainder of Chapter 1 gives an overview on the fundamentals of polymeric semiconductors and the current understanding of ion and electronic transport. Chapter 2 details a study on how changing the side chain chemistry of a polymeric semiconductor influences the mechanism of charge transfer. Chapter 3 focuses on work to understand how the crystalline structure of polymeric semiconductors evolves as a function of the concentration of carriers (and ions) in the material. The fourth Chapter details thermopower measurements in a transistor architecture used to study the evolution of the electronic structure as more ions are introduced into crystalline and amorphous regions of a film. Chapter 5 reports the study of how ion diffusivity can influence the degree of localization between the ion and hole at the molecular scale through a counter-ion exchange process. In Chapter 6, I describe some of the

experiments that did not work throughout my graduate career and share some guidelines that I learned along the way to make the projects in previous Chapters successful. This Dissertation ends with a short conclusions chapter describing the future directions I foresee in the field and in my experimental work.

1.1 The fundamental principles of semiconducting polymers

The ability for a polymer to conduct charge arises from its molecular structure. Semiconducting polymers possess backbones with sp^2–hybridized carbon atoms (or other sp^2–hybridized atoms with a lone pair). The unhybridized p orbital forms a π–bond with one neighboring carbon atom, which results in alternating double and single bonds along the polymeric backbone. Polymers with this backbone structure are characterized as conjugated polymers.

Polyacetylene is the simplest conjugated polymer (**Figure 1.1a**). Although not studied widely today, polyacetylene is responsible for launching the field of semiconducting polymers to where it is today. In the late 1970s, it was found that the electrical conductivity of polyacetylene could be enhanced by exposure to bromine and other oxidizing agents. Similar processing conditions led to electrical conductivity approaching 1000 S cm^{-1}, seven orders of magnitude higher than its pristine state.[6,7] Doped polyacetylene is unstable in air and insoluble in most solvents, which shifted the focus in the field to polymers that were more stable and easier to process.

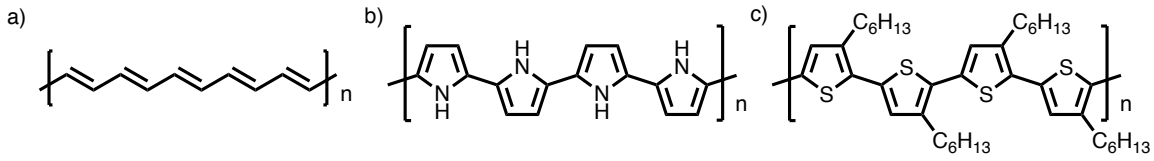

Figure 1.1. Chemical structures of common semiconducting polymers. (a) (trans-)Polyacetylene is the simplest semiconducting polymer, exhibiting a conjugated backbone. (b) Polypyrrole maintains its conjugation because the hybridized nitrogen atom contains a lone pair that forms a π-orbital. (c) Poly(3-hexylthiophene) (P3HT) is a commonly studied semiconducting polymer. Each monomer is functionalized with an alkyl side chain, which leads to increased solubility and processability with respect to polyacetylene.

A conjugated polymer contains molecular orbitals (MOs) that are typically delocalized over several repeat units. Electrons are filled from the lowest energy orbitals to the highest energy orbitals, with two electrons (of opposite spin states) per orbital according to the Pauli exclusion principle. The orbital of the highest energy that is occupied is referred to as the highest occupied molecular orbital (HOMO), while the next highest orbital in energy that is unfilled is referred to as the lowest unoccupied molecular orbital (LUMO). The energy difference between the HOMO and LUMO is defined as the band gap, E_G. Since the band gap is governed by the interaction of MOs along the backbone, variations in conformation and synthetic architecture will modify these electronic levels. As a result, the chemical structure and morphology of semiconducting polymers governs their properties.

Due to the number of possible conformations within all macromolecules, disorder is a common attribute of their morphology. The ratio of ordered and disordered regions within a polymeric film is defined as the percent crystallinity. Disorder can originate from polymer synthesis, such as dispersity of the number of repeat units, or from kinetically trapping chains in an unfavorable conformation during processing. Film treatments after casting, such as thermal or solvent annealing, provide mobility to the polymer chains to assemble in a more stable arrangement, typically increasing the crystallinity.[8,9] Logic dictates that amorphous

regions of the polymer have a different band gap than that of the crystalline regions due to the differences in π–bond overlap. Morphological changes induced by ions can also contribute to evolution in the electronic levels of the polymer.

Several methods have been developed to probe the microstructure of polymeric semiconductors. Microscopy is the most direct route to visualize the alignment of polymeric films; high-resolution transmission electron microscopy (HR-TEM) has been used to measure the length scale of alignment within thin films.[10,11] X-ray scattering also provides morphological information about polymers in the film state based on contrast from dipole moments (soft X-rays) or electron density (hard X-rays).[12] Spectroscopy is a third, but less direct, characterization tool for probing crystalline and amorphous domains within a film. Formalisms have been developed to deconvolute contributions of amorphous and aggregated regions to a material's UV-visible spectrum,[13,14] although it should be noted that aggregates can exist in both amorphous and crystalline domains of a film.

1.2 How are charges induced in polymeric semiconductors?

The band gap of semiconducting polymers, determined by the energetic difference between the HOMO and LUMO, is typically 2 – 3 eV, deeming them insulators in their pristine state. Electrons must be removed or added to the polymeric backbone in order to generate charge within the material. This can be achieved through temporary means using field-effect transistors or through permanent means using doping.

1.2.1 Field-effect transistors

Polymeric field-effect transistors (FETs) have been an active field of research since the early 1980s.[15] Field-effect transistors have three components, as shown in **Figure 1.2a**: electrodes (the gate, source, and drain), the active semiconductor layer, and the gate dielectric. Metals or conducting polymers are used as the electrodes, and SiO_2 is commonly employed as the gate dielectric.

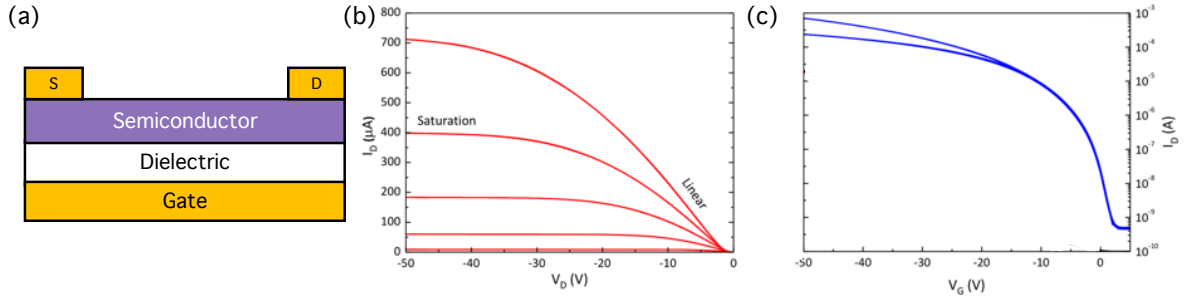

Figure 1.2. (a) Schematic of field effect transistor. (b) Representative output characteristics of a *p*-type FET indicating the linear and saturation regimes. (b) Representative transfer characteristics of a *p*-type FET.

To operate a field-effect transistor, a bias is first applied between the gate electrode and the source or drain (defined as a gate voltage, V_G). The electric field generated by the gate voltage builds up charge on either side of the dielectric layer. The device turns ON once sufficient charge has been generated to create a conducting channel between the source and drain. The gate voltage at which the device turns on is defined as the threshold gate voltage (V_{Th}). A source/drain bias is applied (V_{SD}) to measure the current through the semiconductor. Current can be monitored as a function of V_G at a constant V_{SD}, or it can be measured at a constant V_G as a function of V_{SD}. The former is known as the transfer characteristics, and the latter is known as the output characteristics of the device (**Figure 1.2b** and **1.2c**).

The gradual channel approximation is typically applied to FETs to calculate the mobility of the semiconductor based on the current-voltage characteristics. The gradual channel approximation assumes that the electric field perpendicular to the device generated by the gate voltage is much greater than the field created by applying a source/drain voltage. This approximation is typically valid for when $L > 10d_{dielectric}$.[16] It is also important to note that these equations are built upon the fact that carrier mobility of the device, μ, is independent of V_G. With these assumptions, the source/drain current in the transistor is quantified as Equation 1.1:

$$I_D = \frac{W}{L}\mu C_i[(V_G - V_{Th})V_{SD} - \frac{1}{2}V_{SD}^2] \qquad \text{Equation 1.1}$$

where C_i is the capacitance per area of the dielectric, I_D is the current in the channel, and μ is the carrier mobility of the semiconductor.[17] Here, the dielectric breakdown strength of the gate insulator governs the maximum current (and carrier concentration, p) achievable in the device. Since the areal capacitance of a dielectric is defined as the product of the total charge (Q_T) multiplied by the applied voltage, charge injected in the semiconductor is calculated through Equation 1.2:

$$Q_T = \frac{C_i}{V_G} \qquad \text{Equation 1.2}$$

Quantitatively determining the amount of charge in the active layer is an important advantage of field-effect transistors, but these values are typically limited to 10^{19} carriers cm^{-3} in the case of gate dielectrics operating through polarization mechanisms.

Field-effect transistors act as a switch in integrated circuits, meaning that charge generated in the device is impermanent. Once the gate voltage is removed, holes (or electrons)

will exit the device, which switches the transistor to its OFF state. Therefore, polymers in FETs are only transiently conductive.

1.2.2 Doping

Introducing charge to a polymeric semiconductor through doping operates through a different mechanism than field-effect transistors. Where charge originates from an electrode in field-effect transistors, doped semiconductors receive charge from an extrinsic molecule through a chemical reaction. This mechanism is significantly different from doping of inorganic semiconductors, where atoms with greater or fewer valence electrons substitutionally replace atoms within the lattice structure.

For most polymers, three primary doping methods are used. Charge transfer doping utilizes electron-deficient or electron-rich molecules to oxidize or reduce the polymeric backbone. The probability that charge transfer will occur is generally predicted by offset of the donor HOMO and acceptor LUMO. For the case of *p*-type doping, the LUMO level of the dopant should lie below the HOMO level of the polymer. Several *p*-type and *n*-type dopants have been developed, with common examples including tetrafluorotetracyanoquinodimethane (F_4TCNQ), iron trichloride ($FeCl_3$), 4-(2,3-Dihydro-1,3-dimethyl-1H-benzimidazol-2-yl)-N,N-demthylbenzenamine (N-DMBI), and classes of organometallics.[18] Acidic dopants also fall under this category, although the dopant acts as a protonation site rather than the direct charge transfer site. After charge transfer occurs, the (now charged) dopant acts as the counter-ion to the charge induced on the polymeric backbone.

Chemical dopants are another class of molecules who mechanism involves charge transfer, but simultaneously undergo a chemical change upon oxidation or reduction. These dopants are usually ionic salts that can readily disassociate. Common examples of these dopants include nitric oxide-based salts, such as $NOBF_4$ and $NOPF_6$. In these cases, NO^+ is responsible for oxidizing the polymeric backbone to become NO, which evolves as a gas as shown in Equation 1.3:

$$Polymer + NOPF_6 \rightarrow Polymer^+ + PF_6^- + NO(g) \qquad \text{Equation 1.3}$$

The corresponding counter-ion of the salt (BF_4^- or PF_6^-) is the final counter-ion to the charge induced by reduction of NO^+. Other organic salts have been observed to have a similar effect, such as trityl tetrakis(pentafluorophenyl)borate (TrTPFB) and tetrabutyl ammonium bromide (TBABr).[19] For chemical dopants, it is the hope that the reacted species either remains in the polymer as a spectator molecule or exits the film in the gas phase.

1.2.3 Electrochemical doping

Electrochemical doping is the third subset of doping techniques, but this mechanism merits its own section due to the unique overlap of field-effect transistors and doping. In the basic sense, electrochemical doping occurs whenever a charge carrier is sourced from an electrode in contact with the polymer. This is sometimes utilized in commercial synthesis to generate polymers like PEDOT, polypyrrole, and polyaniline. These polymers must be paired with anionic moieties to maintain charge neutrality.

Another subset of electrochemical doping that has garnered attention within polymeric semiconductors is the organic electrochemical transistor (OECT). OECTs have the same components as field-effect transistors and typically adopt similar geometries. One

distinguishing component is what is used as the dielectric. OECTs employ gate insulators that contain cations and ions that polarize as a result of an applied gate bias.[20] Due to the porous nature of polymeric semiconductors, ions can then infiltrate the semiconducting layer rather than remaining at the semiconductor/dielectric interface, as shown in **Figure 1.3**.

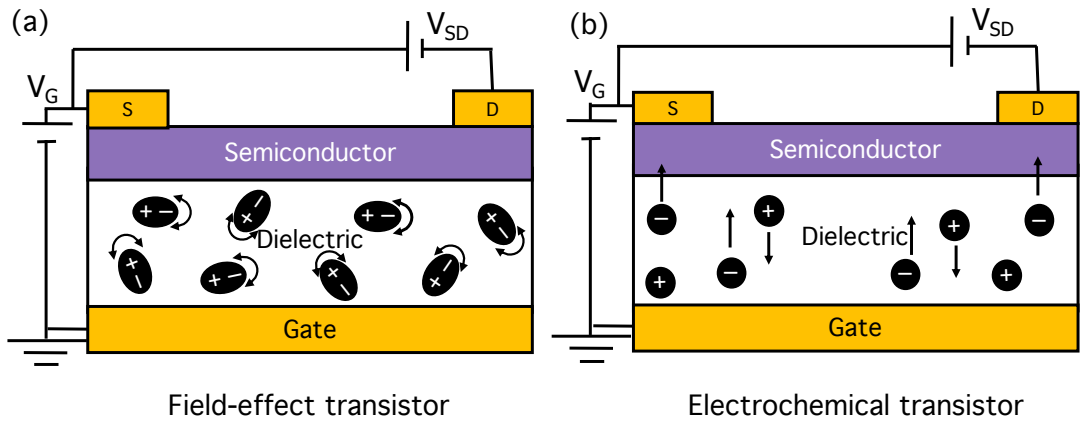

Figure 1.3. Schematic representations of a field-effect transistor (a) and an electrochemical transistor (b). Ions within the dielectric can infiltrate the active layer in an electrochemical transistor unless tethered to the dielectric material. This phenomenon leads to charge generated throughout the bulk of the semiconductor.

As a result, the semiconductor can sustain charge throughout the bulk of the layer rather than only at the interface, which is the case for field-effect transistors. This phenomenon enables a larger range of achievable carrier concentration since doping is carried out in the bulk. An impermeable semiconductor, such as organic single crystals, used with an ion-containing dielectric is considered an electrical double layer (EDL) transistor, which operates in a way similar to field-effect transistors that polarize at the semiconductor/dielectric interface.[21]

Another distinguishing component of OECTs compared to other doping methods is the ability to directly quantify the carrier concentration of the polymeric semiconductor for a

given gate bias. Carrier concentration is calculatable by integrating the gate current with time and normalizing through the volume of the channel through Equation 1.4:

$$p = \frac{Q_T}{V} = \frac{\int (I_G - I_L)\, dt}{eAt} \qquad \text{Equation 1.4}$$

where Q_T is the same quantity calculable with FETs. Using this calculation provides a strong benefit to electrochemical doping, as other doping methods require further characterization to ascertain carrier concentration, such as UV-Vis, EPR, or Hall effect measurements.

Electrochemical transistors have enormous scientific potential as a platform to study doped semiconductors while exerting greater control over the doping level compared to charge transfer and chemical doping. This geometry allows us to answer several questions that are somewhat difficult to answer using other doping methods. Chapters 3 and 4 utilize the electrochemical doping platform to address fundamental questions at the core of how doped semiconducting polymers operate.

1.3 Polymeric semiconductors as mixed conductors

As evidenced in Section 1.2, all doped semiconducting polymers require conduction of ions and electrons for their operation. Although mixed conductors are more strictly defined as materials where the conductivity of ions and electrons are comparable, most polymers exhibit some degree of ionic mobility. The communities that study mixed conductors have a responsibility not to simply apply principles from ion conductors and electron conductors separately, but to understand how the motion of one impacts the transport properties of the other.

1.3.1 Chemical and morphological contributions to mixed conduction

The chemical structure of a polymer is critical to its electrical and ionic conductivity. As mentioned in Section 1.1, the delocalization of molecular orbitals along the backbone is partially influenced by the molecular structure. The polymeric side chains partially control the morphology of the polymer, but do not contribute to the electronic conductivity. The side chains thus provide a useful route to potentially optimize mixed conduction within a single materials system.

Side chains that solvate ionic charge have been used to exhibit ionic and electronic conduction. This idea was first demonstrated in 1987 for insertion electrodes by synthesizing polypyrrole with ethylene oxide pendant groups.[22] Ether-oxygen-based side chains are a natural choice to potentially utilize the ion-conducting properties of poly(ethylene oxide) (PEO), which exhibits some of the highest ionic conductivity values to date (10^{-3} S/cm with Li^+).[23] Polyelectrolytes, conjugated polymers with charge-containing side groups, also increase the ionic conductivity by adding solvation sites within the side chains. These strategies simultaneously change the dielectric environment of the polymer, where polar groups are more hydrophilic and more effective at charge disassociation. Other approaches to mixed conductivity include two-component blends[24] and block copolymers[25] that combine electron- and ion-conducting components.

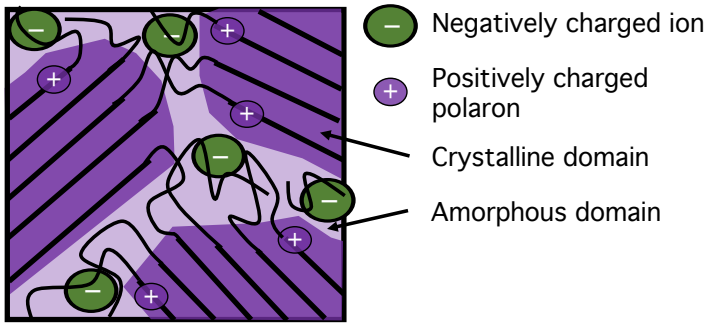

Figure 1.4. Schematic of preferential segregation of charge carriers (ions and polarons) within the domains of a semi-crystalline polymer.

An optimized morphology remains an active area of research in polymeric mixed conductors, as each carrier type requires seemingly orthogonal properties. While an ordered structure increases electronic mobility, ionic mobility relies on segmental motion and free volume of flexible chains. These differences lead to segregation of electrons and ions within the more crystalline and amorphous regions of the polymer system, respectively (**Figure 1.4**). An open question in mixed conductors is the threshold necessary for both ion and electron conduction to occur. In the context of electron-conducting polymers, the minimum crystallinity necessary is surprisingly small; an aggregate fraction as small as 40% in P3EHT was enough to create a percolated network of ordered regions for charge transport.[26] For a highly-doped P3HT/PEO blend, the electrical conductivity remains the same as a function of increasing PEO content until approximately 80% PEO by weight.[27]

1.3.1 The diagonal effects of ion/electron conduction in polymeric semiconductors

One pressing challenge in the field of doped polymeric semiconductors is determining the degree of coupling between charges on the backbone and their corresponding counter-ion. How these charge carriers interact depends on a multitude of factors, including the dielectric

constant and the microstructure. However, these properties have been observed to evolve as a function of doping level, which makes unconvoluted studies difficult to realize.

Although the assumption remains that more favorable conditions for ionic conduction will lead to lower electronic conductivity and vice versa, there is evidence that synergistic effects may be present in semiconducting polymer systems. It was found that the intrinsic electrical conductivity of asymmetric P3HT-PEO block copolymers was higher than the P3HT homopolymer, indicating that a non-electrically conducting microphase can aid in structuring the electrically conducting microphase.[25] Structural changes induced by ion insertion, proposed to be a phase transition, was found to be coupled with increased electronic mobility, indicating that an increased degree of coupling could lead to superior properties.[28,29] It is therefore the obligation of the polymeric electronics community to not ignore the presence of the charge-neutralizing counter-ion, but to understand their effects, positive or negative, on the resulting transport properties.

1.4 References

(1) Hill, S. The Samsung Galaxy Fold is finally available for purchase. https://www.digitaltrends.com/mobile/samsung-galaxy-fold-news/ (accessed Oct 27, 2019).

(2) Gu, X.; Shaw, L.; Gu, K.; Toney, M. F.; Bao, Z. The Meniscus-Guided Deposition of Semiconducting Polymers. *Nature Communications* **2018**, *9* (1). https://doi.org/10.1038/s41467-018-02833-9.

(3) Eckstein, R.; Strobel, N.; Rödlmeier, T.; Glaser, K.; Lemmer, U.; Hernandez-Sosa, G. Fully Digitally Printed Image Sensor Based on Organic Photodiodes. *Advanced Optical Materials* **2018**, *6* (5), 1701108. https://doi.org/10.1002/adom.201701108.

(4) Rivnay, J.; Owens, R. M.; Malliaras, G. G. The Rise of Organic Bioelectronics. *Chemistry of Materials* **2014**, *26* (1), 679–685. https://doi.org/10.1021/cm4022003.

(5) Muench, S.; Wild, A.; Friebe, C.; Häupler, B.; Janoschka, T.; Schubert, U. S. Polymer-Based Organic Batteries. *Chemical Reviews* **2016**, *116* (16), 9438–9484. https://doi.org/10.1021/acs.chemrev.6b00070.

(6) Chiang, C. K.; Fincher, C. R.; Park, Y. W.; Heeger, A. J.; Shirakawa, H.; Louis, E. J.; Gau, S. C.; MacDiarmid, A. G. Electrical Conductivity in Doped Polyacetylene. *Phys. Rev. Lett.* **1977**, *39* (17), 1098–1101. https://doi.org/10.1103/PhysRevLett.39.1098.
(7) Gill, W. D.; Bludau, W.; Geiss, R. H.; Grant, P. M.; Greene, R. L.; Mayerle, J. J.; Street, G. B. Structure and Electronic Properties of Polymeric Sulfur Nitride ${(\mathrm{SN})}_{x}$ Modified by Bromine. *Phys. Rev. Lett.* **1977**, *38* (22), 1305–1308. https://doi.org/10.1103/PhysRevLett.38.1305.
(8) Dickey, K. C.; Anthony, J. E.; Loo, Y.-L. Improving Organic Thin-Film Transistor Performance through Solvent-Vapor Annealing of Solution-Processable Triethylsilylethynyl Anthradithiophene. *Advanced Materials* **2006**, *18* (13), 1721–1726. https://doi.org/10.1002/adma.200600188.
(9) Cho, S.; Lee, K.; Yuen, J.; Wang, G.; Moses, D.; Heeger, A. J.; Surin, M.; Lazzaroni, R. Thermal Annealing-Induced Enhancement of the Field-Effect Mobility of Regioregular Poly(3-Hexylthiophene) Films. *Journal of Applied Physics* **2006**, *100* (11), 114503. https://doi.org/10.1063/1.2400796.
(10) Martin, D. C.; Chen, J.; Yang, J.; Drummy, L. F.; Kübel, C. High Resolution Electron Microscopy of Ordered Polymers and Organic Molecular Crystals: Recent Developments and Future Possibilities. *Journal of Polymer Science Part B: Polymer Physics* **2005**, *43* (14), 1749–1778. https://doi.org/10.1002/polb.20419.
(11) Kuei, B.; Aplan, M. P.; Litofsky, J. H.; Gomez, E. D. New Opportunities in Transmission Electron Microscopy of Polymers. *Materials Science and Engineering: R: Reports* **2019**, 100516. https://doi.org/10.1016/j.mser.2019.100516.
(12) Rivnay, J.; Mannsfeld, S. C. B.; Miller, C. E.; Salleo, A.; Toney, M. F. Quantitative Determination of Organic Semiconductor Microstructure from the Molecular to Device Scale. *Chem. Rev.* **2012**, *112* (10), 5488–5519. https://doi.org/10.1021/cr3001109.
(13) Spano, F. C. Modeling Disorder in Polymer Aggregates: The Optical Spectroscopy of Regioregular Poly(3-Hexylthiophene) Thin Films. *J. Chem. Phys.* **2005**, *122* (23), 234701. https://doi.org/10.1063/1.1914768.
(14) Clark, J.; Chang, J.-F.; Spano, F. C.; Friend, R. H.; Silva, C. Determining Exciton Bandwidth and Film Microstructure in Polythiophene Films Using Linear Absorption Spectroscopy. *Applied Physics Letters* **2009**, *94* (16), 163306. https://doi.org/10.1063/1.3110904.
(15) Ebisawa, F.; Kurokawa, T.; Nara, S. Electrical Properties of Polyacetylene/Polysiloxane Interface. *Journal of Applied Physics* **1983**, *54* (6), 3255–3259. https://doi.org/10.1063/1.332488.
(16) Zaumseil, J.; Sirringhaus, H. Electron and Ambipolar Transport in Organic Field-Effect Transistors. *Chem. Rev.* **2007**, *107* (4), 1296–1323. https://doi.org/10.1021/cr0501543.
(17) Shur, M. *Physics of Semiconductor Devices*, first edition edition.; Pearson: Englewood Cliffs, N.J, 1990.
(18) Guo, S.; Kim, S. B.; Mohapatra, S. K.; Qi, Y.; Sajoto, T.; Kahn, A.; Marder, S. R.; Barlow, S. N-Doping of Organic Electronic Materials Using Air-Stable Organometallics. *Advanced Materials* **2012**, *24* (5), 699–703. https://doi.org/10.1002/adma.201103238.

(19) Hu, Y.; Rengert, Z. D.; McDowell, C.; Ford, M. J.; Wang, M.; Karki, A.; Lill, A. T.; Bazan, G. C.; Nguyen, T.-Q. Doping Polymer Semiconductors by Organic Salts: Toward High-Performance Solution-Processed Organic Field-Effect Transistors. *ACS Nano* **2018**, *12* (4), 3938–3946. https://doi.org/10.1021/acsnano.8b01460.
(20) White, H. S.; Kittlesen, G. P.; Wrighton, M. S. Chemical Derivatization of an Array of Three Gold Microelectrodes with Polypyrrole: Fabrication of a Molecule-Based Transistor. *J. Am. Chem. Soc.* **1984**, *106* (18), 5375–5377. https://doi.org/10.1021/ja00330a070.
(21) Shimotani, H.; Asanuma, H.; Iwasa, Y. Electric Double Layer Transistor of Organic Semiconductor Crystals in a Four-Probe Configuration. *Jpn. J. Appl. Phys.* **2007**, *46* (6R), 3613. https://doi.org/10.1143/JJAP.46.3613.
(22) Minett, M. G.; Owen, J. R. Polymeric Insertion Electrodes. *Solid State Ionics* **1988**, *28–30*, 1192–1196. https://doi.org/10.1016/0167-2738(88)90355-4.
(23) Ratner, M. A.; Shriver, D. F. Ion Transport in Solvent-Free Polymers. *Chem. Rev.* **1988**, *88* (1), 109–124. https://doi.org/10.1021/cr00083a006.
(24) Cao, Y.; Yu, G.; Heeger, A. J.; Yang, C. Y. Efficient, Fast Response Light-emitting Electrochemical Cells: Electroluminescent and Solid Electrolyte Polymers with Interpenetrating Network Morphology. *Appl. Phys. Lett.* **1996**, *68* (23), 3218–3220. https://doi.org/10.1063/1.116442.
(25) Patel, S. N.; Javier, A. E.; Stone, G. M.; Mullin, S. A.; Balsara, N. P. Simultaneous Conduction of Electronic Charge and Lithium Ions in Block Copolymers. *ACS Nano* **2012**, *6* (2), 1589–1600. https://doi.org/10.1021/nn2045664.
(26) Duong, D. T.; Ho, V.; Shang, Z.; Mollinger, S.; Mannsfeld, S. C. B.; Dacuña, J.; Toney, M. F.; Segalman, R.; Salleo, A. Mechanism of Crystallization and Implications for Charge Transport in Poly(3-Ethylhexylthiophene) Thin Films. *Advanced Functional Materials* **2014**, *24* (28), 4515–4521. https://doi.org/10.1002/adfm.201304247.
(27) Kiefer, D.; Yu, L.; Fransson, E.; Gómez, A.; Primetzhofer, D.; Amassian, A.; Campoy-Quiles, M.; Müller, C. A Solution-Doped Polymer Semiconductor:Insulator Blend for Thermoelectrics. *Advanced Science* **2017**, *4* (1). https://doi.org/10.1002/advs.201600203.
(28) Thomas, E. M.; Brady, M. A.; Nakayama, H.; Popere, B. C.; Segalman, R. A.; Chabinyc, M. L. X-Ray Scattering Reveals Ion-Induced Microstructural Changes During Electrochemical Gating of Poly(3-Hexylthiophene). *Advanced Functional Materials* **2018**, *28* (44), 1803687. https://doi.org/10.1002/adfm.201803687.
(29) Bischak, C. G.; Flagg, L. Q.; Yan, K.; Rehman, T.; Davies, D. W.; Quezada, R. J.; Onorato, J. W.; Luscombe, C. K.; Diao, Y.; Li, C.-Z.; et al. A Reversible Structural Phase Transition by Electrochemical Ion Injection into a Conjugated Polymer. *arXiv:1910.06440 [cond-mat, physics:physics]* **2019**.

Chapter 2

Side chains impact the doping mechanism in conjugated polythiophenes

Predicting the interactions between a semiconducting polymer and dopant is not straightforward due to the intrinsic structural and energetic disorder in polymeric systems. Although the driving force for efficient charge transfer depends on a favorable offset between the electron donor and acceptor, we demonstrate that the efficacy of doping also relies on structural constraints of incorporating a dopant molecule into the semiconducting polymer film. Here, we report the evolution in spectroscopic and electrical properties of a model conjugated polymer upon exposure to two dopant types: one that directly oxidizes the polymeric backbone and one that protonates the polymer backbone. Through vapor phase infiltration, the common charge transfer dopant, F_4TCNQ, forms a charge transfer complex (CTC) with the polymer poly(3-(2′-ethyl)hexylthiophene) (P3EHT), a conjugated polymer with the same backbone as the well-characterized polymer P3HT, resulting in a maximum electrical conductivity of 3×10^{-5} S cm^{-1}. We postulate that the branched side chains of P3EHT force F_4TCNQ to reside between the π-faces of the crystallites, resulting in partial charge transfer between the donor and the acceptor. Conversely, protonation of the polymeric backbone using the strong acid, HTFSI, increases the electrical conductivity of P3EHT to a maximum of 4×10^{-3} S cm^{-1}, 2 orders of magnitude higher than when a charge transfer dopant

is used. The ability for the backbone of P3EHT to be protonated by an acid dopant, but not oxidized directly by F_4TCNQ, suggests that steric hindrance plays a significant role in the degree of charge transfer between dopant and polymer, even when the driving force for charge transfer is sufficient.

2.1 Introduction

The principles that govern effective charge transfer between the dopant and polymer are poorly understood, despite the fact that doping is essential to increase the electrical conductivity in semiconducting polymers. Previously, offset between the LUMO of the dopant and the HOMO of the polymer for p-type doping has been considered sufficient to predict effective charge transfer;[1] however, some organic semiconductors exhibit minimal change in electrical conductivity when exposed to dopants, even with a favorable driving force for oxidation or reduction to occur.[2,3] Additionally, it is difficult to develop structure–property relationships for the mechanisms of doping in organic semiconductors due to the abundance of semiconductors, dopants, and processing conditions. To access the potential of semiconducting polymers for applications in thermoelectrics,[4] bioelectronics,[5] and ohmic contacts,[6] we must develop a better understanding of the interactions necessary for efficient charge transfer between a dopant molecule and its polymeric host.

By studying a branched side chain analogue of the widely used polymeric semiconductor poly(3-hexylthiophene) (P3HT), we find that steric hindrance induced by branched side chains can control the final degree of charge transfer with an acceptor. Steric hindrance inhibits integer charge transfer from poly(3-(2′-ethyl)hexylthiophene) (P3EHT) by

the small-molecule 2,3,5,6-tetrafluoro-7,7,8,8-tetracyanoquinodimethane (F_4TCNQ) by constraining the molecule to reside in the π-stacks of the crystallites rather than in the side chains, resulting in the formation of a charge transfer complex between the two. In contrast, the acidic dopant bis(trifluoromethanesulfonyl)imide (HTFSI), which first protonates the polymeric backbone, leads to carrier formation in P3EHT and higher electrical conductivity. This work shows that charge transfer between a dopant and polymer can be modified by steric factors and offers a model system to further understand the implications of different doping mechanisms on the resulting electrical properties.

2.2 Experimental Methods

Materials. Regioregular P3EHT was synthesized using a previously reported method (M_n = 16000 g mol^{-1}).[7] P3HT was purchased from Rieke Metals (M_n = 58000 g mol^{-1}) and used as received. F_4TCNQ was purchased from TCI America, and HTFSI was purchased from Acros Organics and used as received. Anhydrous chlorobenzene was purchased from Sigma-Aldrich.

Thin Film Preparation. Thin films were prepared on silicon substrates (300 nm thermal oxide, University Wafer) for atomic force microscopy, and z-cut quartz substrates (University Wafer) for conductivity and UV-Vis measurements. Substrates were sonicated for 10 minutes sequentially in soapy water, DI water, and an IPA/acetone mixture, followed by exposure to UV-ozone (Jelight, Model 18) for 5 minutes. Gold contacts (20 nm) were thermally evaporated on the quartz substrates using a shadow mask. Neat P3EHT (10 mg ml^{-1}, chlorobenzene) was

spun cast at 1500 rpm to afford 40-nm thick films. Films were annealed at 100 °C for 10 minutes under nitrogen and quenched to 25 °C for 80 minutes.

Vapor Doping. Vapor doping was performed using a sealed vessel, described in a previous publication.[8] In short, pristine films are attached to the lid of a jar that contains crystals of solid dopant. The jar is closed and heated for a set of exposure times on a hot plate. The HTFSI-doping vessel was heated at 40 °C and the F_4TCNQ-doping vessel was heated at 210 °C. Exposures were done incrementally in order to capture several doping levels of the films.

X-ray Characterization. X-ray scattering was conducted on beamline 7.3.3 at the Advanced Light Source (ALS).[9] Silver behenate was used as a calibration for the beam center and sample-to-detector distance. 2D GIWAXS scattering images were collected using a Pilatus 2M area detector at an incidence angle of 0.12° with 5–60 s exposure times. The samples were kept under a helium environment during X-ray exposure to minimize sample degradation and air scattering. The collected data were processed using Nika, a 2D data reduction macro on Igor Pro using established procedures. To correct for the grazing incidence geometry, scattering intensity was integrated along a small sector near the missing wedge to obtain 1D profiles near $q_z = 0$.

Atomic Force Microscopy. Topological images were captured using tapping mode with an NT-MDT custom-built atomic force microscope (controller model NTEGRA P9) under ambient conditions. Bruker OTESPA-R3 probes (0.01–0.02 Ω-cm Si, f_0 = 300 kHz) were used to complete these measurements. The scan size of each image was 2 μm x 2 μm.

UV-visible Spectroscopy. UV-visible measurements were taken using an Agilent Cary 60 UV-Vis Spectrophotometer. Spectra were taken on 0.5 mm-thick quartz substrates.

FTIR Spectroscopy. FTIR spectroscopy was performed in a nitrogen atmosphere using a Nicolet Magna 850 FTIR Spectrometer with an InSb detector. Samples were spincast on KBr salt plates (13 x 2 mm, PIKE Technologies) using the same conditions as for other characterization techniques.

Electrical Characterization. All electrical measurements were performed under a nitrogen environment inside a glovebox. Electrical conductivity was measured using a Keithley 6485 picoammeter. Measurements were taken in the in-plane direction using the TLM method to eliminate contact resistance for samples with low conductivity.

2.3 Results and Discussion

Two primary charge transfer processes have been observed in organic semiconductors, but it remains unclear what factors determine the process for a given donor and acceptor pair.[10,11] Integer charge transfer (ICT) between the organic semiconductor and dopant results in an integer-charged counterion to stabilize the polaron formed within the semiconductor. If only partial charge transfer occurs between dopant and semiconductor, a charge transfer complex (CTC) forms due to strong electronic coupling of the dopant and polymer states. Charge transfer complexes have been observed for oligomeric and some polymeric semiconductors,[2,12–14] but it is not clear whether energetic or structural features control the degree of charge transfer. For instance, the prototypical semiconductor/dopant pair, poly(3-hexylthiophene) (P3HT):F_4TCNQ, which typically undergoes ICT, was found to form a CTC if specific processing conditions were used during film formation.[15] The amount of aggregation, as well as the degree of intrachain order,[16] has also been shown to influence the degree of charge transfer in the solution state, indicating that structural constraints are

important to consider for pairs of dopants and semiconductors.[17] Despite these results, little rationalization has been made to justify why one process would be favorable with respect to the other.

Incorporating branched side chains onto the backbone of a semiconducting polymer forces a greater degree of energetic overlap between a counterion and backbone without modifying the polymer's ionization energy. Here, we use the p-type semiconductor regioregular poly(3-(2′-ethyl)hexylthiophene) (P3EHT), whose backbone is identical to poly(3-hexylthiophene) (P3HT) but contains an ethyl group on the second carbon of the alkyl side chain (**Figure 2.1**). The effect of the branched side chains of P3EHT is to decrease its melting point to approximately 80 °C and slow the rate of crystallization upon film formation relative to its linear alkyl side chain analogue.[19–22] Because P3EHT has the same backbone as P3HT, their ionization potentials are within 0.1 eV of one another in solution (~5.2 eV).[23] While P3EHT has a slightly deeper IE than P3HT, we still expect that ICT should be possible. ICT with F_4TCNQ has been observed for polymers with an even deeper IE and also with acceptors with a smaller EA.[24,25]

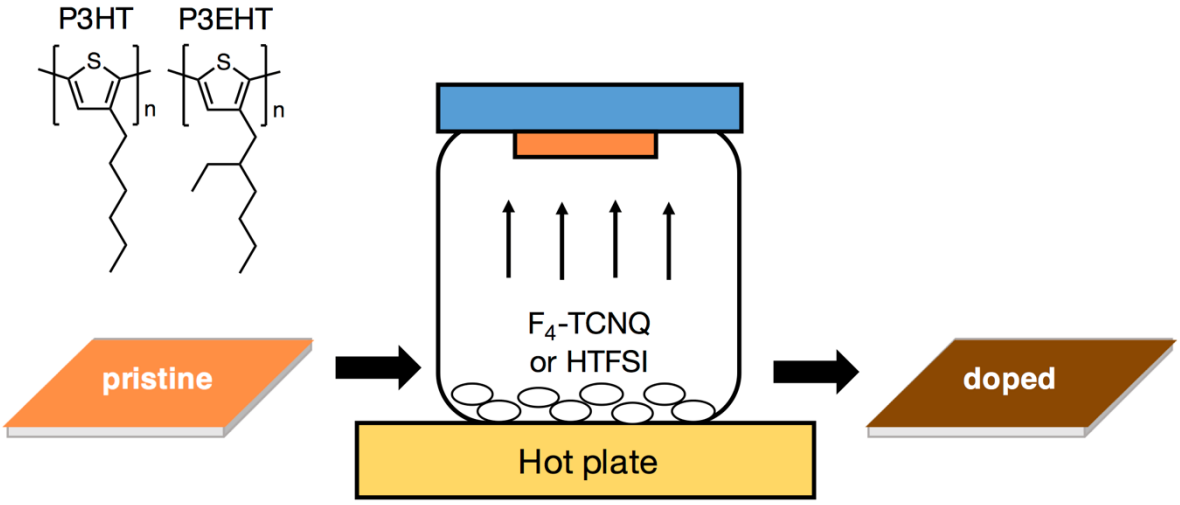

Figure 2.1. Chemical structure of P3EHT and schematic illustrating the method of vapor doping. The molecule F_4TCNQ is used as the charge transfer dopant, and HTFSI is used as the acid dopant.

Diffusion of a dopant molecule from the vapor phase into the semiconducting polymer enables control over doping level while minimizing confounding variables introduced through the use of solvents.[26,27] In this work, we examine two dopants: one that oxidizes the polymer backbone by intermolecular electron transfer ("charge-transfer dopant") and one that protonates the polymer backbone causing formation of carriers ("acid dopant"). Here, the small-molecule F_4TCNQ is used as the charge-transfer dopant for its favorable electron affinity (EA = 5.2 eV) and its previous success in doping P3HT through the vapor phase.[26] We use HTFSI as the acid dopant because it is a strong acid (pKa ~ −12),[28] it has a low melting point (TM = 53 °C), and it has been used previously as an effective dopant in the vapor phase.[29] For acidic dopants, it is postulated that the carbocation generated from backbone protonation oxidizes a neighboring chain, leading to the traditional radical-hole pair and the associated Brønsted base.[30]

The formation of free charge carriers in P3EHT when doped with F_4TCNQ is impeded in the solid state, indicated by the absence of polaronic features in the optical spectra of the doped films. Undoped regioregular P3EHT films form highly structured aggregates that exhibit well-defined 0–0, 0–1, and 0–2 transitions, as shown in **Figure 2.2**. The optical spectrum of an undoped film provides quantitative information about how much of the film is aggregated as well as the primary type of aggregate in the film, developed through the work of Spano *et al.*[31] A least-squares fitting analysis of the spectrum of an undoped P3EHT film (**Figure A1**) using this model yields that the fully crystallized film consists of approximately 40% primarily H-type aggregates, in agreement with previous work[19] and similar to what is typically observed for P3HT. These values are also comparable to bulk DSC measurements of P3EHT.[18] As a function of exposure time to F_4TCNQ vapor, the UV–vis spectra of P3EHT show a decrease of the optical transition of the neutral polymer centered around 2.4 eV. The optical transitions corresponding to F_4TCNQ^- at 1.43 and 1.62 eV (red dashed lines) are not present at any doping level, indicating that ICT does not occur even at low doping concentrations.[12] With increased F_4TCNQ content, new features appear near 1.0, 1.8, and 3.4 eV (denoted C1, C2, and C3 in **Figure 2.2a**). We postulate that these transitions correspond to optical transitions of the charge transfer complex formed between F_4TCNQ and P3EHT. A CTC also occurs in solution-cast films (**Figure A2**), which indicates that the dopant and polymer form a complex independent of processing route. Surprisingly, spectral signatures of the F_4TCNQ anion are observed in a solution of F_4TCNQ and P3EHT, indicating that ICT occurs between the donor and acceptor prior to casting the solid film. (**Figure A2**). These observations are in stark contrast to the linear side chain analogue P3HT, which has been shown to exhibit ICT by F_4TCNQ when doped in either the solution or vapor phase.[32,33,27] To

quantify the degree of charge transfer, the C≡N stretching vibration of F_4TCNQ in a doped film provides a route because the frequency of this stretching mode is sensitive to the charge of the molecule.[34] In a vapor-doped film of P3EHT with F_4TCNQ, the nitrile stretching mode shifts from its value in neutral form of 2227 cm^{-1} to 2209 cm^{-1}, corresponding to a degree of charge transfer (δ) of approximately 0.6 (**Figure A3**) based on an empirical model developed for donor:acceptor salts.[35,36] A degree of charge transfer less than unity confirms that the dopant forms a CTC with the polymer.

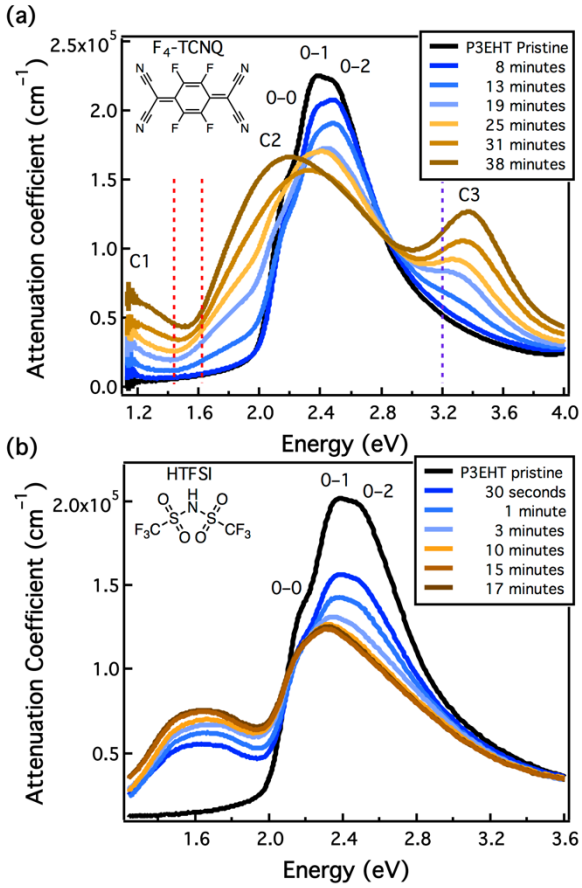

Figure 2.2. UV–vis spectra of P3EHT films upon exposure to (a) F_4TCNQ and (b) HTFSI vapor. Dashed lines correspond to the absorption features characteristic of the F_4TCNQ anion (1.43 and 1.62 eV) and neutral F_4TCNQ (3.2 eV). A clear polaron signature appears when exposed to an acid, while features indicative of complexation are observed when exposed to the charge transfer dopant.

The branched side chains of P3EHT do not inhibit polaron formation upon exposure to HTFSI vapor. The absorption spectra of P3EHT with increasing exposure time to HTFSI show a decrease in the neutral polymer species along with an increase of a subgap feature at

1.6 eV, corresponding to the presence of polaronic carriers within the film (**Figure 2.2b**).[37] The absorption spectra contain an isosbestic point at 1.97 eV, evidence of conversion between the neutral and charged polymer species. A similar feature, centered around 1.55 eV, is observed when P3HT is doped using HTFSI as a control (**Figure A4**), consistent with previous reports of acid doping with other thiophene-backbone semiconductors.[29] We do not expect formation of a CTC when using HTFSI as a dopant. HTFSI initially transfers a proton that subsequently generates a carrier, and the closed-shell counterion $TFSI^-$ is unlikely to interact electronically with the backbone. For example, structural characterization of electrochemical transistors of P3HT shows that $TFSI^-$ resides in the side chains after oxidation of the backbone.[38] This difference in doping mechanism, along with the smaller size of $TFSI^-$ with respect to F_4TCNQ^-, is likely why polaronic carriers form within the acid-doped films of P3EHT.

The crystallites within the film of P3EHT exhibit different behavior depending on which dopant the film is exposed to, indicating the role of structural changes during doping. Crystallites of pristine P3EHT exhibit an edge-on texture with an alkyl stacking distance of 14.4 Å (**Figure 2.3a**), approximately 1 Å smaller than that of P3HT. While the side chains of P3EHT are racemic due to the chiral center, GIWAXS still shows higher-order peaks in the scattering pattern. The chiral center in the side chains likely leads to disorder in the packing of the side chains but does not prevent ordering of the backbones.[21] When exposed to HTFSI vapor, higher-order peaks seen in the neutral pattern disappear, and the alkyl stacking distance of the crystallites begins to increase (shift to lower q values) (**Figure 2.3b**) at low exposure times. With increasing exposure to HTFSI, the alkyl stacking increases further to

approximately 15.4 Å, indicating that the acidic dopant resides primarily in the side chains of the crystallites. Although the changes in alkyl spacing are smaller than the nominal size of $TFSI^-$ (~7.2 Å in length and ~2.5 Å in width from DFT calculations), we attribute these small shifts to free volume within the side chains of the crystallites before doping. When the film is exposed to F_4TCNQ vapor, little change in the alkyl spacing in crystalline domains is observed at short exposure times (**Figure 2.3c**). Further exposure to F_4TCNQ vapor leads to a slight decrease in the alkyl stacking distance to approximately 14.1 Å, contrary to the behavior of many polymer:dopant combinations,[27,32,39] but previously observed for a form of blend of P3HT:F_4TCNQ that yields a CTC.[15] For this reason along with the spectroscopic evidence for a CTC, we expect the dopant not to reside in the side chains of the crystallites but rather near the π-face of the backbone. This geometry is consistent with DFT calculations on donor:acceptor complexes[40,41] and the need for significant overlap of the wave functions between donor and acceptor to form a CTC. Additionally, the alkyl stacking peaks broaden, and the majority of scattering peaks of the neutral pattern disappears with higher exposure times to F_4TCNQ, indicating that the crystallites of the film are becoming more disordered as the dopant infiltrates the film. The emergence of a new scattering peak near 1.85 $Å^{-1}$ in doped films of P3EHT suggests a significant change in the structural ordering of the crystalline domains (see Appendix B). There are, unfortunately, not enough peaks in the 2D X-ray scattering pattern of the doped films to determine a unique unit cell.

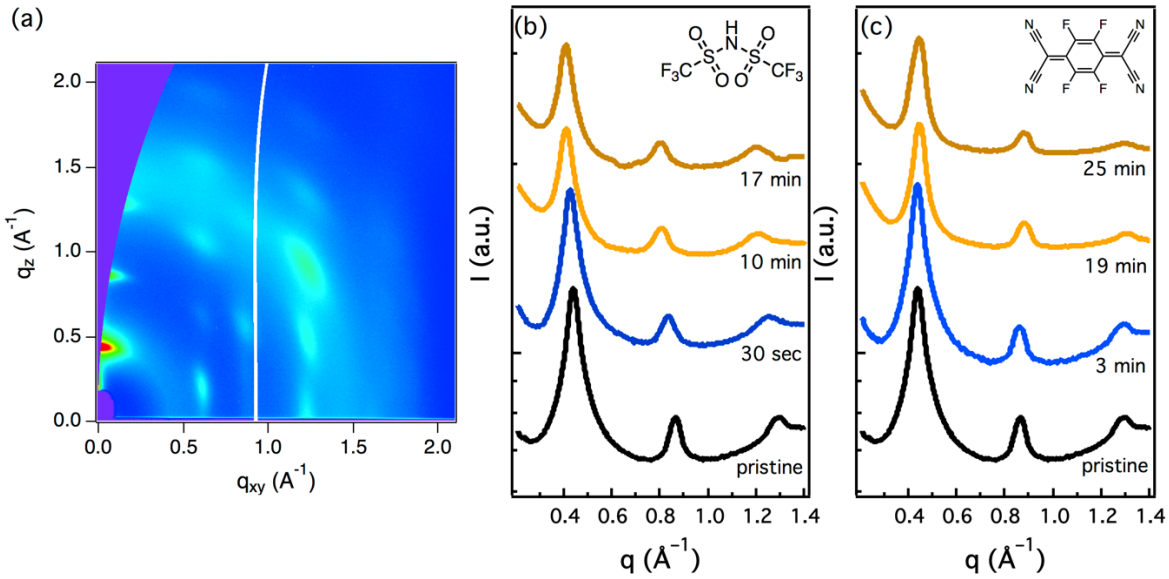

Figure 2.3. GIWAXS of P3EHT-doped films. (a) A 2D scattering image of a pristine P3EHT film. The crystallites are primarily edge-on, with the alkyl stacking direction along the out-of-plane direction. Line cuts taken near the missing wedge in the out-of-plane direction for (b) HTFSI-doped films indicate an increase in the alkyl stacking direction, indicating that this dopant resides in the side chains of the P3EHT crystallites. The alkyl stacking distance of the F_4TCNQ-doped films (c) slightly decreases as a function of exposure time along with peak broadening, which indicates disordering of the crystallites within the film.

The formation of free carriers caused by HTFSI exposure leads to an increase in the electrical conductivity by more than 2 orders of magnitude compared to F_4TCNQ. The electrical conductivity of P3EHT increases rapidly as a function of exposure to HTFSI (**Figure 2.4**, brown diamonds), followed by a slow increase in conductivity with further exposure time with a maximum value of $\sim 4 \times 10^{-3}$ S cm^{-1}. As the mobility measured with thin-film transistors of P3EHT is lower than P3HT by approximately 3 orders of magnitude,[20] we expect the maximal conductivity of P3EHT to approach 10^{-2} S cm^{-1} at high doping levels ($\sim 1 \times 10^{21}$ cm^{-3}). In contrast, the electrical conductivity of P3EHT when exposed to F_4TCNQ increases by approximately a factor of 10 to 3×10^{-5} S cm^{-1}. Longer exposure times for both dopants lead to the presence of aggregates on the surface by atomic force microscopy (see Appendix B). The complex formed between F_4TCNQ and P3EHT creates few free carriers in the film, as only partial charge transfer occurs between the two species. As a result, these films exhibit a

lower electrical conductivity than the HTFSI-doped films that provide a benchmark for the expected conductivity of P3EHT at high carrier concentration.

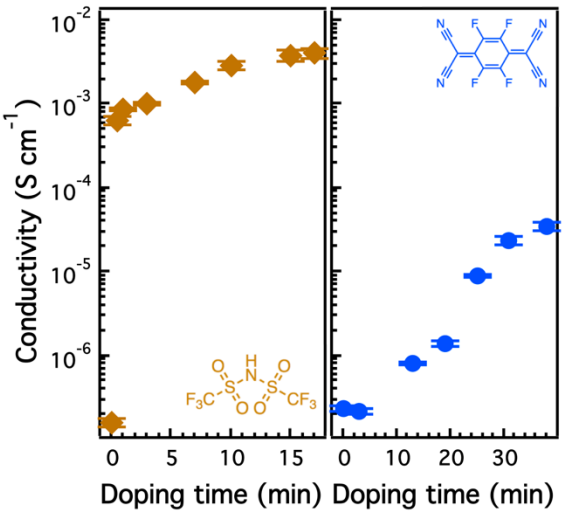

Figure 2.4. Electrical conductivity as a function of exposure time of HTFSI vapor (brown diamonds) and F_4TCNQ vapor (blue circles). Formation of a charge transfer complex leads to a maximal conductivity 2 orders of magnitude lower than from integer charge transfer. Error bars correspond to ± one standard deviation from triplicate measurements.

2.4 Conclusions

The results herein indicate that side chain functionalization can drastically impact whether ICT or formation of a CTC occurs. Through UV–vis spectroscopy and electrical conductivity measurements, we show that vapor-phase infiltration of two molecules that dope through either direct oxidation or protonation exhibits significantly different doping efficacies for P3EHT. As both dopants diffuse into the bulk of the film, we posit that the steric hindrance introduced through the branched side chains allows $TFSI^-$ to reside in the side chains but forces F_4TCNQ to interact with the π-face of the polymeric backbone. The position of F_4TCNQ facilitates a strong electronic interaction between donor and acceptor, leading to a CTC rather than ITC that is observed for polymers where F_4TCNQ resides in the side chains. The importance of having a weak electronic interaction between the dopant and semiconductor to form carriers has been discussed in the context of crystalline molecular

semiconductors.[13] Investigating the role of dopant size to control charge transfer between polymeric donors and acceptors would offer greater predictive power for dopant/polymer pairs.

Although two primary doping mechanisms have been reported for semiconducting polymers, it is less clear whether the two can coexist within one materials system. Indeed, features consistent with the optical transition at 2 eV (peak C2 in **Figure 2.2**) have been observed in UV–vis spectra of doped polythiophenes, but the assignment of the peak remains unclear.[37,42] Investigating polymers that can exhibit CTC formation can lead to a broader understanding of whether additional doping mechanisms exist and if the electrical properties of charge transfer complexes can be improved. Because the difference between ionization energy and electron affinity for many dopant:polymer combinations is often 0.2 eV or less, it is surprising that a CTC is not more commonly seen in doped semiconducting polymers. The fact that an integer charge transfer mechanism is common raises questions regarding the role of spatial separation during charge transfer between donor and acceptor. The role of steric hindrance also has implications for the design of low-voltage loss organic solar cells where donor:acceptor complexes are the sites of charge generation and recombination.[43] Future work will also lead to a more unified picture for charge transfer in organic semiconductors to disentangle the role of energetics and steric constraints.

2.5 Acknowledgements

The authors acknowledge funding support from the Department of Energy Office of Basic Energy Sciences under grant no. DE-SC0016390 for final spectroscopic and electrical

characterization. Atomic force microscopy measurements were supported by the Dow Chemical Company. Initial spectroscopic measurements made use of shared facilities of the UCSB MRSEC (NSF DMR 1720256), a member of the Materials Research Facilities Network (www.mrfn.org). This research used resources of the Advanced Light Source, which is a U.S. Department of Energy Office of Science User Facility under contract no. DE-AC02-05CH11231. E.M.T. gratefully acknowledges support from the NSF Graduate Fellowship (DGE-1650114). The authors thank Clayton Dahlman and Naveen Venkatesan for initial scattering results and Mikayla Barry for assistance with FTIR measurements.

2.6 Appendix A

2.6.1 Analysis of Aggregate Absorption

The model developed by Spano *et al.*[44,45] describes the absorption spectra, *A*, of P3HT by Equation A1:

$$\mathrm{A} = C \sum_{m=0} \left(\frac{e^{-S} S^m}{m!}\right)\left(1 - \frac{We^{-S}}{2E_p} \sum_{n \neq m} \frac{S^n}{n!\,(n-m)!}\right)^2 \exp\left(-\frac{\left(E - E_{0-0} - mE_p - 0.5WS^m e^{-S}\right)^2}{2\sigma^2}\right) \Big/ \sigma\sqrt{2\pi}$$

Equation A1

The Huang-Rhys factor, S, is assumed to be unity. The proportionality constant (*C*), excitonic bandwidth (*W*), Gaussian width (σ), and the 0-0 intrachain transition ($E_{0\text{-}0}$) are varying parameters in this model. The characteristic C=C phonon stretch is 0.179 eV for P3EHT. A Matlab code was utilized to perform a least-square fit for the 0–0, 0–1, 0–2, 0–3, and 0–4 transitions as a function of carrier density. A typical fit is shown in **Figure A1**.

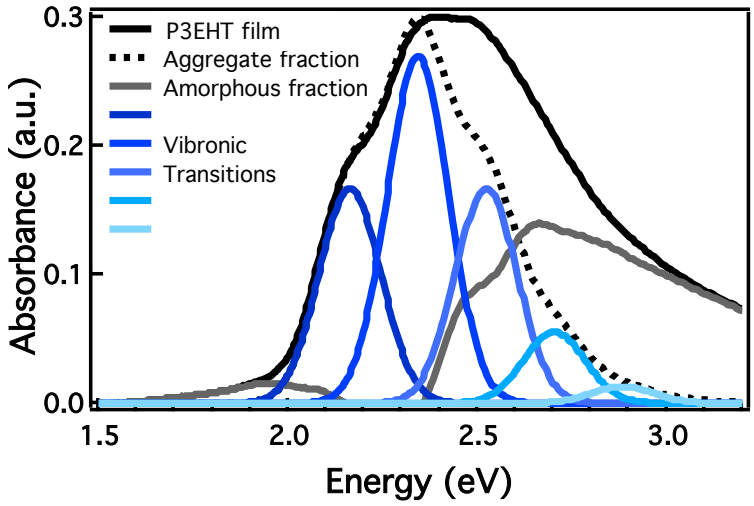

Figure A1: Analysis of P3EHT spectra. The model by Spano *et al.* indicates that about 40% of the P3EHT film is aggregated.

2.6.2 Doped solution spectra

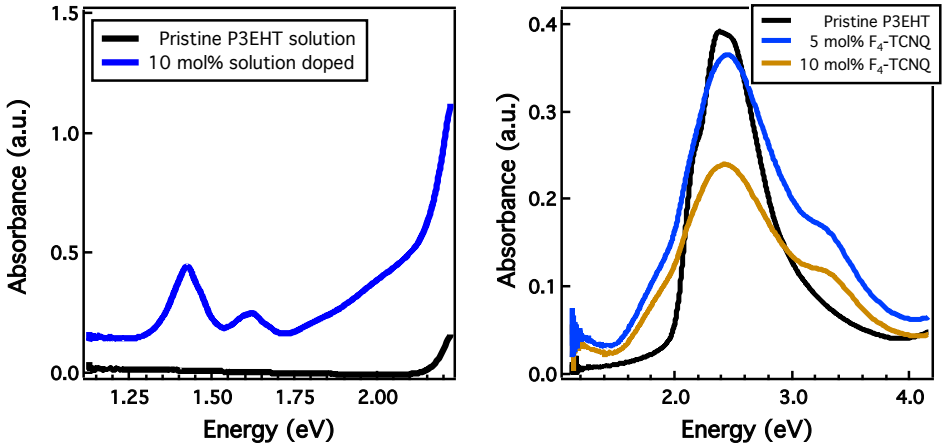

Figure A2: (a) Solution spectra of pristine P3EHT and P3EHT with 10 mol% F_4TCNQ. The familiar peaks corresponding to the anion of F_4TCNQ appear at 1.4 and 1.6 eV, indicating that the dopant does not complex with the polymer while in solution. Here, data is shown to 2.5 eV since the solvent obscures the spectra at higher energy. Upon film formation from a doped solution (b), a charge transfer complex forms evidenced by the emergence of similar features as the vapor doped films (**Figure 2.2** in main text) near 3.4 eV, 1.8 eV, and 1 eV.

2.6.3 FTIR Spectroscopy

The C≡N vibrational stretch of F_4TCNQ is sensitive to the charge of the molecule. The degree of charge transfer, δ, between F_4TCNQ and the corresponding acceptor is found using Equation A2:

$$\delta = \frac{2\Delta\nu}{\nu_0}\left[1 - \frac{\nu_1^2}{\nu_0^2}\right]^{-1} \qquad \text{Equation A2}$$

where ν_0 corresponds to the neutral value of the C≡N stretch (2227 cm^{-1}), ν_1 corresponds to the frequency of the C≡N stretch for the radical anion (2194 cm^{-1} corresponding to integer charge transfer (ICT)), and $\Delta\nu$ is the difference between the observed stretch and the neutral C≡N stretch.[46,47]

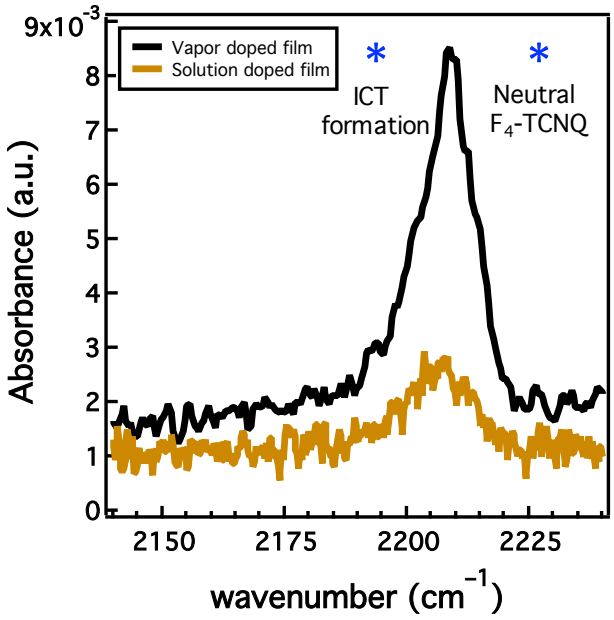

Figure A3: FTIR of heavily-doped P3EHT films from vapor infiltration (black) and from solution casting (orange). The peak corresponding to the C≡N vibrational stretch occurs at 2209 cm^{-1} for the vapor doped film and 2206 cm^{-1} for the solution doped film, corresponding to a degree of charge transfer of 0.6. A value of 1 is expected for ICT, such as between P3HT and F_4TCNQ.

2.6.4 P3HT Acid Doping

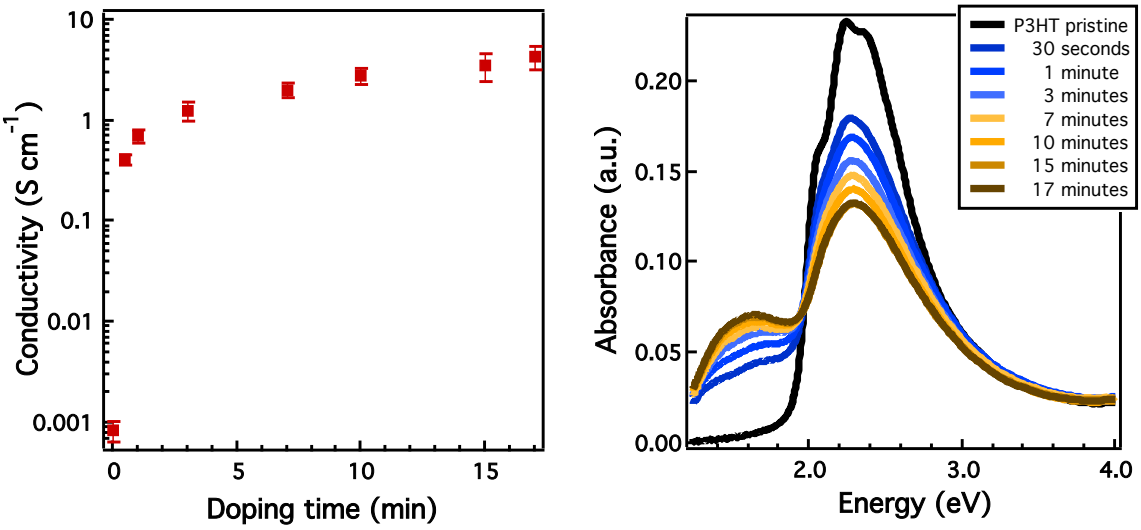

Figure A4: Electrical conductivity (left) and absorption (right) of a film of P3HT with exposure to HTFSI. The resulting electrical conductivity of P3HT is higher than for P3EHT when using the same dopant, potentially due to the differences in intrachain order between the two polymers.[48] Error bars represent one standard deviation from the average value, taken from triplicate measurements.

2.6.5 2D GIWAXS images of vapor and acid doping

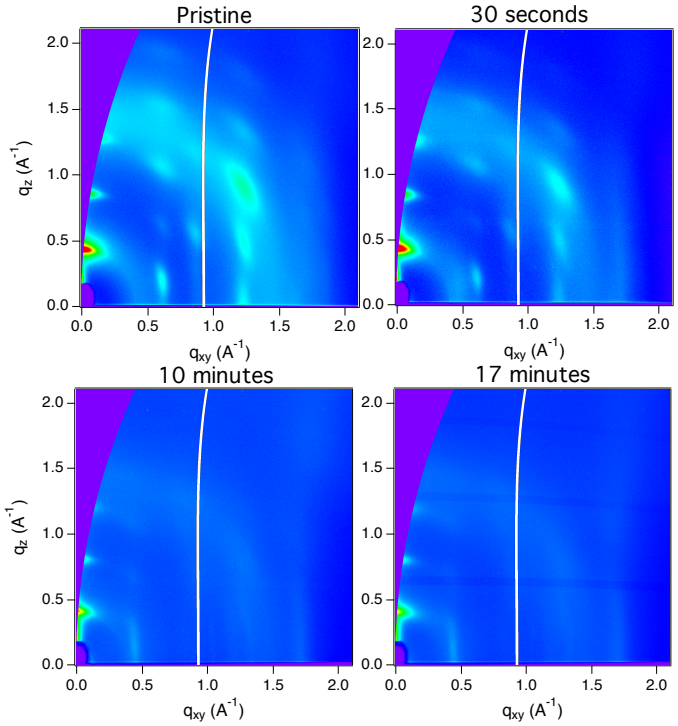

Figure A5: 2D images of P3EHT when exposed to HTFSI. Long exposure times leads to a modified crystal structure and loss of higher order peaks, seen clearly in the 10 minute and 17 minute images.

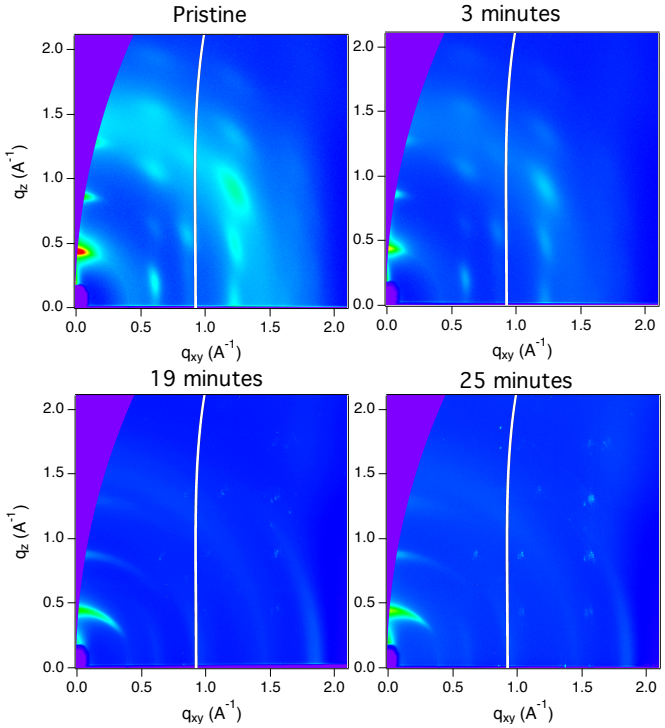

Figure A6: 2D images of P3EHT when exposed to F_4TCNQ. Broadening of the peaks along with new features with increasing exposure times is indicative of disorder and a modified crystal structure induced upon infiltration of the dopant. Sharp features seen in the 25 minute image may correspond to F_4TCNQ at the surface.

2.6.6 Atomic Force Microscopy

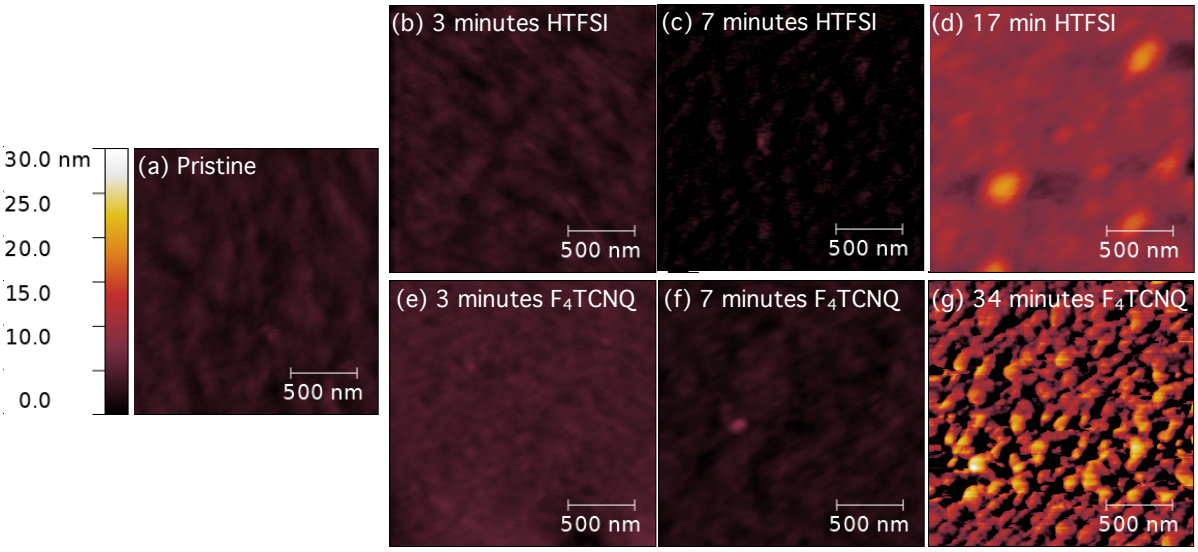

Figure A7: AFM height images of thin films of P3EHT in its pristine form (a) and when exposed to HTFSI and F_4TCNQ vapor (b-g). Doping with the HTFSI for 3 minutes (b) and 7 minutes (c) introduces little change to the microstructure. Exposure times greater than 17 minutes (d) result in large droplets on the film surface, indicating that the vapor no longer infiltrates the film. A similar effect occurs for F_4TCNQ vapor after 3 minutes (e) and 19 minutes (f) of exposure time, followed by eventual F_4TCNQ crystals aggregating at the film surface after 34 minutes (g). All images have the same color map scale bar.

2.7 References

(1) Pfeiffer, M.; Leo, K.; Zhou, X.; Huang, J. S.; Hofmann, M.; Werner, A.; Blochwitz-Nimoth, J. Doped Organic Semiconductors: Physics and Application in Light Emitting Diodes. Org. Electron. 2003, 4 (2–3), 89–103.

(2) Salzmann, I.; Heimel, G.; Duhm, S.; Oehzelt, M.; Pingel, P.; George, B. M.; Schnegg, A.; Lips, K.; Blum, R.-P.; Vollmer, A.; Koch, N. Intermolecular Hybridization Governs Molecular Electrical Doping. Phys. Rev. Lett. 2012, 108 (3), 035502.

(3) Nikolka, M.; Nasrallah, I.; Rose, B.; Ravva, M. K.; Broch, K.; Sadhanala, A.; Harkin, D.; Charmet, J.; Hurhangee, M.; Brown, A.; Illig, S.; Too, P.; Jongman, J.; McCulloch, I.; Brédas, J.-L.; Sirringhaus, H. High Operational and Environmental Stability of High-Mobility Conjugated Polymer Field-Effect Transistors through the Use of Molecular Additives. Nat. Mater. 2017, 16 (3), 356–362.

(4) Russ, B.; Glaudell, A.; Urban, J. J.; Chabinyc, M. L.; Segalman, R. A. Organic Thermoelectric Materials for Energy Harvesting and Temperature Control. Nat. Rev. Mater. 2016, 1 (10), 16050.

(5) Inal, S.; Rivnay, J.; Suiu, A.-O.; Malliaras, G. G.; McCulloch, I. Conjugated Polymers in Bioelectronics. Acc. Chem. Res. 2018, 51 (6), 1368–1376.

(6) Ma, H.; Yip, H.-L.; Huang, F.; Jen, A. K.-Y. Interface Engineering for Organic Electronics. Adv. Funct. Mater. 2010, 20 (9), 1371–1388.

(7) Ho, V.; Boudouris, B. W.; Segalman, R. A. Tuning Polythiophene Crystallization through Systematic Side Chain Functionalization. Macromolecules 2010, 43 (19), 7895–7899.

(8) Patel, S. N.; Glaudell, A. M.; Kiefer, D.; Chabinyc, M. L. Increasing the Thermoelectric Power Factor of a Semiconducting Polymer by Doping from the Vapor Phase. ACS Macro Lett. 2016, 5, 268–272.

(9) Hexemer, A.; Bras, W.; Glossinger, J.; Schaible, E.; Gann, E.; Kirian, R.; MacDowell, A.; Church, M.; Rude, B.; Padmore, H. A SAXS/WAXS/GISAXS Beamline with Multilayer Monochromator. J. Phys. Conf. Ser. 2010, 247, 012007.

(10) Jacobs, I. E.; Moulé, A. J. Controlling Molecular Doping in Organic Semiconductors. Adv. Mater. 2017, 1703063:1-39.

(11) Salzmann, I.; Heimel, G.; Oehzelt, M.; Winkler, S.; Koch, N. Molecular Electrical Doping of Organic Semiconductors: Fundamental Mechanisms and Emerging Dopant Design Rules. Acc. Chem. Res. 2016, 49 (3), 370–378.

(12) Méndez, H.; Heimel, G.; Winkler, S.; Frisch, J.; Opitz, A.; Sauer, K.; Wegner, B.; Oehzelt, M.; Röthel, C.; Duhm, S.; Többens, D.; Koch, N.; Salzmann, I. Charge-Transfer Crystallites as Molecular Electrical Dopants. Nat. Commun. 2015, 6 (1).

(13) Méndez, H.; Heimel, G.; Opitz, A.; Sauer, K.; Barkowski, P.; Oehzelt, M.; Soeda, J.; Okamoto, T.; Takeya, J.; Arlin, J.-B.; Balandier, J.Y.; Geerts, Y.; Koch, N.; Salzmann, I. Doping of Organic Semiconductors: Impact of Dopant Strength and Electronic Coupling. Angew. Chem. Int. Ed. 2013, 52 (30), 7751–7755.

(14) Yang, J.; Li, Y.; Duhm, S.; Tang, J.; Kera, S.; Ueno, N. Molecular Structure-Dependent Charge Injection and Doping Efficiencies of Organic Semiconductors: Impact of Side Chain Substitution. Adv. Mater. Interfaces 2014, 1 (3), 1300128.

(15) Jacobs, I. E.; Cendra, C.; Harrelson, T. F.; Bedolla Valdez, Z. I.; Faller, R.; Salleo, A.; Moulé, A. J. Polymorphism Controls the Degree of Charge Transfer in a Molecularly Doped Semiconducting Polymer. Mater. Horiz. 2018, 5 (4), 655–660.
(16) Chew, A. R.; Salleo, A. Spectroscopic Studies of Dopant-Induced Conformational Changes in Poly (3-Hexylthiophene) Thin Films. Mrs Commun. 2017, 7, 728–734.
(17) Gao, J.; Niles, E. T.; Grey, J. K. Aggregates Promote Efficient Charge Transfer Doping of Poly(3-Hexylthiophene). J. Phys. Chem. Lett. 2013, 4 (17), 2953–2957.
(18) Ho, V.; Boudouris, B. W.; Segalman, R. A. Tuning Polythiophene Crystallization through Systematic Side Chain Functionalization. Macromolecules 2010, 43 (19), 7895–7899.
(19) Boudouris, B. W.; Ho, V.; Jimison, L. H.; Toney, M. F.; Salleo, A.; Segalman, R. A. Real-Time Observation of Poly(3-Alkylthiophene) Crystallization and Correlation with Transient Optoelectronic Properties. Macromolecules 2011, 44 (17), 6653–6658.
(20) Duong, D. T.; Ho, V.; Shang, Z.; Mollinger, S.; Mannsfeld, S. C. B.; Dacuña, J.; Toney, M. F.; Segalman, R.; Salleo, A. Mechanism of Crystallization and Implications for Charge Transport in Poly(3-Ethylhexylthiophene) Thin Films. Adv. Funct. Mater. 2014, 24 (28), 4515–4521.
(21) Himmelberger, S.; Duong, D. T.; Northrup, J. E.; Rivnay, J.; Koch, F. P. V.; Beckingham, B. S.; Stingelin, N.; Segalman, R. A.; Mannsfeld, S. C. B.; Salleo, A. Role of Side-Chain Branching on Thin-Film Structure and Electronic Properties of Polythiophenes. Adv. Funct. Mater. 2015, 25 (17), 2616–2624.
(22) Yu, L.; Davidson, E.; Sharma, A.; Andersson, M. R.; Segalman, R.; Müller, C. Isothermal Crystallization Kinetics and Time–Temperature–Transformation of the Conjugated Polymer: Poly(3-(2′-Ethyl)Hexylthiophene). Chem. Mater. 2017, 29 (13), 5654–5662.
(23) Burkhart, B.; Khlyabich, P. P.; Thompson, B. C. Influence of the Ethylhexyl Side-Chain Content on the Open-Circuit Voltage in Rr-Poly(3-Hexylthiophene- Co -3-(2-Ethylhexyl)Thiophene) Copolymers. Macromolecules 2012, 45 (9), 3740–3748.
(24) Patel, S. N.; Glaudell, A. M.; Peterson, K. A.; Thomas, E. M.; O'Hara, K. A.; Lim, E.; Chabinyc, M. L. Morphology Controls the Thermoelectric Power Factor of a Doped Semiconducting Polymer. Sci. Adv. 2017, 3 (6), e1700434.
(25) Li, J.; Zhang, G.; Holm, D. M.; Jacobs, I. E.; Yin, B.; Stroeve, P.; Mascal, M.; Moulé, A. J. Introducing Solubility Control for Improved Organic P-Type Dopants. Chem. Mater. 2015, 27 (16), 5765–5774.
(26) Lim, E.; Peterson, K. A.; Su, G. M.; Chabinyc, M. L. Thermoelectric Properties of Poly(3-Hexylthiophene) (P3HT) Doped with 2,3,5,6-Tetrafluoro-7,7,8,8-Tetracyanoquinodimethane (F_4TCNQ) by Vapor-Phase Infiltration. Chem. Mater. 2018, 30 (3), 998–1010.
(27) Patel, S. N.; Glaudell, A. M.; Kiefer, D.; Chabinyc, M. L. Increasing the Thermoelectric Power Factor of a Semiconducting Polymer by Doping from the Vapor Phase. ACS Macro Lett. 2016, 5, 268–272.
(28) Kütt, A.; Rodima, T.; Saame, J.; Raamat, E.; Mäemets, V.; Kaljurand, I.; Koppel, I. A.; Garlyauskayte, R. Y.; Yagupolskii, Y. L.; Yagupolskii, L. M.; Bernhardt, E.; Willner, H.; Leito, I. Equilibrium Acidities of Superacids. J. Org. Chem. 2011, 76 (2), 391–395.

(29) Hofmann, A. I.; Kroon, R.; Yu, L.; Müller, C. Highly Stable Doping of a Polar Polythiophene through Co-Processing with Sulfonic Acids and Bistriflimide. J. Mater. Chem. C 2018, 6 (26), 6905–6910.
(30) Han, C. C.; Elsenbaumer, R. L. Protonic Acids: Generally Applicable Dopants for Conducting Polymers. Synth. Met. 1989, 30 (1), 123–131.
(31) Clark, J.; Chang, J.-F.; Spano, F. C.; Friend, R. H.; Silva, C. Determining Exciton Bandwidth and Film Microstructure in Polythiophene Films Using Linear Absorption Spectroscopy. Appl. Phys. Lett. 2009, 94 (16), 163306.
(32) Duong, D. T.; Wang, C.; Antono, E.; Toney, M. F.; Salleo, A. The Chemical and Structural Origin of Efficient P-Type Doping in P3HT. Org. Electron. 2013, 14 (5), 1330–1336.
(33) Jacobs, I. E.; Aasen, E. W.; Oliveira, J. L.; Fonseca, T. N.; Roehling, J. D.; Li, J.; Zhang, G.; Augustine, M. P.; Mascal, M.; Moulé, A. J. Comparison of Solution-Mixed and Sequentially Processed P3HT:F4TCNQ Films: Effect of Doping-Induced Aggregation on Film Morphology. J Mater Chem C 2016, 4 (16), 3454–3466.
(34) Zanon, I.; Pecile, C. Vibronic Structure of the Near-Infrared and Visible Electronic Transitions of 7,7,8,8-Tetracyanoquinodimethane Radical Anion. J. Phys. Chem. 1983, 87 (19), 3657–3664.
(35) Kampar, E.; Neilands, O. Degree of Charge Transfer in Donor–Acceptor Systems of the π–π Type. Russ. Chem. Rev. 1986, 55 (4), 334.
(36) Chappell, J. S.; Bloch, A. N.; Bryden, W. A.; Maxfield, M.; Poehler, T. O.; Cowan, D. O. Degree of Charge Transfer in Organic Conductors by Infrared Absorption Spectroscopy. J. Am. Chem. Soc. 1981, 103 (9), 2442–2443.
(37) Colaneri, N.; Nowak, M.; Spiegel, D.; Hotta, S.; Heeger, A. J. Bipolarons in Poly(3-Methylthiophene): Spectroscopic, Magnetic, and Electrochemical Measurements. Phys. Rev. B 1987, 36 (15), 7964–7968.
(38) Thomas, E. M.; Brady, M. A.; Nakayama, H.; Popere, B. C.; Segalman, R. A.; Chabinyc, M. L. X-Ray Scattering Reveals Ion-Induced Microstructural Changes During Electrochemical Gating of Poly(3-Hexylthiophene). Adv. Funct. Mater. 2018, 28 (44), 1803687.
(39) Scholes, D. T.; Hawks, S. A.; Yee, P. Y.; Wu, H.; Lindemuth, J. R.; Tolbert, S. H.; Schwartz, B. J. Overcoming Film Quality Issues for Conjugated Polymers Doped with F_4TCNQ by Solution Sequential Processing: Hall Effect, Structural, and Optical Measurements. J. Phys. Chem. Lett. 2015, 6 (23), 4786–4793.
(40) Zhu, L.; Kim, E.-G.; Yi, Y.; Brédas, J.-L. Charge Transfer in Molecular Complexes with 2,3,5,6-Tetrafluoro-7,7,8,8-Tetracyanoquinodimethane (F_4-TCNQ): A Density Functional Theory Study. Chem. Mater. 2011, 23 (23), 5149–5159.
(41) Sini, G.; Sears, J. S.; Brédas, J.-L. Evaluating the Performance of DFT Functionals in Assessing the Interaction Energy and Ground-State Charge Transfer of Donor/Acceptor Complexes: Tetrathiafulvalene–Tetracyanoquinodimethane (TTF–TCNQ) as a Model Case. J. Chem. Theory Comput. 2011, 7 (3), 602–609.
(42) Wang, C.; Duong, D. T.; Vandewal, K.; Rivnay, J.; Salleo, A. Optical Measurement of Doping Efficiency in Poly(3-Hexylthiophene) Solutions and Thin Films. Phys. Rev. B 2015, 91 (8).

(43) Qian, D.; Zheng, Z.; Yao, H.; Tress, W.; Hopper, T. R.; Chen, S.; Li, S.; Liu, J.; Chen, S.; Zhang, J.; Liu, X.-K.; Gao, B.; Ouyang, L.; Jin, Y.; Pozina, G.; Buyanova, I. A.; Chen, W. M.; Inganäs, O.; Coropceanu, V.; Brédas, J.-L.; Yan, H.; Hou, J.; Zhang, F.; Bakulin, A. A.; Gao, F. Design Rules for Minimizing Voltage Losses in High-Efficiency Organic Solar Cells. Nat. Mater. 2018, 17 (8), 703–709.

(44) Clark, J.; Silva, C.; Friend, R. H.; Spano, F. C. Role of Intermolecular Coupling in the Photophysics of Disordered Organic Semiconductors: Aggregate Emission in Regioregular Polythiophene. Phys. Rev. Lett. 2007, 98 (20), 206406:1-4.

(45) Clark, J.; Chang, J.-F.; Spano, F. C.; Friend, R. H.; Silva, C. Determining Exciton Bandwidth and Film Microstructure in Polythiophene Films Using Linear Absorption Spectroscopy. Appl. Phys. Lett. 2009, 94 (16), 163306.

(46) Kampar, E.; Neilands, O. Degree of Charge Transfer in Donor–Acceptor Systems of the π–π Type. Russ. Chem. Rev. 1986, 55 (4), 334.

(47) Chappell, J. S.; Bloch, A. N.; Bryden, W. A.; Maxfield, M.; Poehler, T. O.; Cowan, D. O. Degree of Charge Transfer in Organic Conductors by Infrared Absorption Spectroscopy. J. Am. Chem. Soc. 1981, 103 (9), 2442–2443.

(48) Chew, A. R.; Ghosh, R.; Pakhnyuk, V.; Onorato, J.; Davidson, E. C.; Segalman, R. A.; Luscombe, C. K.; Spano, F. C.; Salleo, A. Unraveling the Effect of Conformational and Electronic Disorder in the Charge Transport Processes of Semiconducting Polymers. Adv. Funct. Mater. 2018, 1804142.

Chapter 3

Microstructural and Electronic Properties Are Correlated During Electrochemical Gating of Poly(3-Hexylthiophene)

The heterogeneous microstructure of semicrystalline polymers complicates the relationship between their electrical conductivity and carrier concentration. Charge transport models typically describe conductivity with an assumption of uniform doping throughout the material. Here, the evolution in morphology and optoelectronic properties of poly(3-hexylthiophene) (P3HT) is reported as a function of carrier concentration in an organic electrochemical transistor using a polymeric ionic liquid (PIL) as the gate insulator. *Operando* grazing incidence X-ray scattering reveals that negatively charged ions from the dielectric first infiltrate the amorphous regions of the semiconductor, and then penetrate the crystalline regions at a critical carrier density of 4×10^{20} cm^{-3}. Upon infiltration, the crystallites expand by 12% in the alkyl stacking direction and compress by 4% in the π–π stacking direction. The change in crystal structure of P3HT correlates with a sharply increasing effective carrier mobility. UV–visible spectroscopy reveals that holes induced in P3HT first reside in the crystalline regions of the polymer, which verifies that a charge carrier need not be in the same physical domain as its associated counterion. The dopant-induced morphological changes of P3HT rationalize the dependence of mobility on carrier concentration, suggesting a phase transition of crystalline regions at high carrier concentration.

3.1 Introduction

The value of electrical conductivity in semiconducting materials is related to the product between carrier concentration (p) and carrier mobility (μ). In polymeric semiconductors, the conductivity[1] and mobility[2] increase non-linearly as a function of carrier density. Efforts to explain this phenomenon have shown that a static density of states (DOS) fails to capture the transport behavior of semiconducting polymers, particularly at high carrier concentrations.[3-5] As a result, the super-linear relationship is commonly attributed to changes in the distribution in transport sites as the DOS broadens with increasing energetic disorder.[6] An important factor generally overlooked in models of charge transport is how the microstructure of the semiconducting polymer evolves over the same range of carrier concentration, which will also contribute to the DOS. To realize the full potential of semiconducting polymers for applications such as bioelectronics[7] and thermoelectrics,[8] we must develop a more robust understanding of how the morphology of a polymer evolves as carriers are introduced.

By using an organic electrochemical transistor (OECT), we observed how the microstructure, absorption spectra, and electronic mobility of poly(3-hexylthiophene) (P3HT) evolve as a function of carrier concentration. The unique sample geometry used here enables structural and spectroscopic characterization of the semiconductor while exerting control over carrier density. The combination of methods allows us to deconvolute the competing effects that determine the electrical conductivity in P3HT as a function of charge carrier concentration.

Introducing charge carriers by doping is an important process to control the electrical properties of semiconductors.[9] Doping in polymers occurs by chemical reactions with molecular species that oxidize (or reduce) the polymer backbone.[10,11] To ensure charge neutrality, the reduced (or oxidized) dopant acts as the counterion to the charged backbone. Small molecules that dope polymers by charge transfer are typically added to the polymer in solution (either before or after the film is cast),[11,12] or through vapor phase infiltration.[10] Addition of dopants increases the concentration of carriers in the polymer but has been shown to induce morphological changes with increasing dopant concentration,[13-15] which influences the degree of energetic disorder and complicates the rationalization of doping effects on charge transport.

Electrochemical doping provides a way to modify the electrical properties of semiconducting polymers through control over the carrier density.[16] Conventional transistors that operate using the field effect permit a ≈2 nm conducting channel at the interface of the semiconductor and gate dielectric.[17] More recently, ion-containing dielectrics have been used to dope semiconductors electrochemically by the diffusion of ions into the semiconductor that neutralize charge generated from the electrode.[18] Infiltration of ions into the active layer creates a bulk channel of charge carriers, rather than forming a channel only at the dielectric-semiconductor interface. Integrating the current generated between the source and gate of the device determines the total charge generated in the semiconductor (Q), providing a way to quantitatively determine carrier concentration (p) in the active layer with doping. The maximum carrier density generated in semiconductors by using non-ionic dielectrics approaches 10^{19} cm^{-3}, above which dielectric breakdown occurs from the applied field.[17]

Electrochemical transistors, on the other hand, have accessed carrier densities exceeding 10^{21} cm^{-3} which enables the investigation of charge transport in the highly doped regime.[2,19]

Here, we use a polymeric ionic liquid (PIL) as a gate insulator in an OECT to examine the structural, optoelectronic, and electronic effects of doping a p-type semiconductor. In contrast to other ion-based gate insulators such as ionic liquids[16] and ion gels,[19] the single-ion conducting polymer restricts ion movement to the mobile species, which eliminates unwanted ion pair diffusion into the semiconductor. In combination with other experimental techniques, gating with a PIL permits us to examine the changes in both the crystalline and the amorphous regions of polymeric semiconductors as the carrier density approaches the number of monomeric units in the material. We find that at low carrier concentration, hole polarons tend to exist in the crystalline regions of the semiconductor. As the carrier concentration increases, the counterions penetrate the crystalline regions of the semiconductor, modifying the structure of the polymer's crystalline domains and indicating a contrast in preferential environment between carrier and counterion. The calculated mobility strongly correlates with the structural changes that are observed. Structural changes induced by dopants signify a new need for models that treat a polymer in its doped state as a different material than its pristine counterpart.

3.2 Experimental Methods

Materials: P3HT was obtained from Merck and used as received. The anthracene-functionalized PIL was synthesized using reversible addition-fragmentation chain-transfer polymerization (RAFT) as detailed in previous work.[25] Tri(chloro)octylsilane was purchased

from Sigma-Aldrich and stored in a nitrogen glovebox. All solvents were purchased in their anhydrous form from Sigma-Aldrich. Si/SiO_2 wafers were purchased from University Wafer, and gold-coated silicon wafers were purchased from Sigma-Aldrich. The elastomer and crosslinking agent used for PDMS were purchased from Dow Corning.

Device Fabrication: A solution of the PIL (50 mg/ml, acetonitrile) was dropcast on a gold-coated silicon substrate at 35 °C followed by annealing in vacuo for 12 hours. PIL films were crosslinked by exposure to 365 nm light for 45 minutes in a nitrogen glovebox. A solution of P3HT (50 mg/ml, chlorobenzene) was spun on OTS-functionalized Si/SiO_2 substrates at 1500 rpm for 45 seconds and annealed at 150 °C for 10 minutes, affording a thickness of approximately 250 nm as measured by profilometry. Annealed films were transferred to the crosslinked PIL film using a PDMS stamp according to previous methods. Gold Source/drain contacts (W = 2.7 mm, L = 150 μm, t = 80 nm) were thermally evaporated using a shadow mask. Output/transfer curves were obtained using a Keithley 2400 sourcemeter.

Beamline Device Fabrication: Devices for *operando* experiments followed an identical protocol to the lab devices but with a larger channel (W = 1 cm, L = 2 mm) to allow for the incident beam to pass through the channel with minimal scattering from the gold. The finalized device was mounted onto a glass slide using double-sided tape. Electrical wires were connected to the source, drain, and gate contacts using silver paste. Bias was controlled during scattering experiments using a Keithley 2400 with connection to the electrical wires.

UV-Vis Device Fabrication: Quartz substrates were cleaned using the same procedure detailed above. A thin (10 nm) layer of gold was evaporated on the substrates to minimize

electrochemical effects but be translucent. The gold-coated ITO substrates were then partially masked with Teflon tape to enable contact with external wires. P3HT and the PIL for *operando* UV-Vis measurements were spuncast and dropcast, respectively, following procedures detailed above. The films were sandwiched together and annealed at 50 °C under vacuum to ensure homogenous contact between the PIL and P3HT layers. The Teflon tape was removed and wires were connected to either substrate using double sided tape to control the bias between the device terminals. UV-Vis spectra were acquired using an Agilent Cary 60 UV-Vis Spectrophotometer. Spectra were taken at each voltage after 60 s of bias to ensure a uniform dopant profile in the semiconductor.

X-ray Characterization: X-ray scattering was conducted on beamline 7.3.3 at the Advanced Light Source (ALS). Silver behenate was used as a calibration for the beam center and sample-to-detector distance. 2D GIWAXS scattering images were collected using a Pilatus 2 M area detector at an incidence angle of 0.20° with 5 s exposure times. The samples were kept under a helium environment during X-ray exposure to minimize sample degradation and scattering from O_2. The collected data were processed using Nika, a 2D data reduction macro on Igor Pro using established procedures. 1D profiles along the in-plane direction were created by plotting intensities along line cuts near $q_{xy} = 0$. To correct for the grazing incidence geometry, scattering intensity was integrated along a small sector near the missing wedge to obtain 1D profiles near $q_z = 0$.

3.3 Results and Discussion

Electrochemical gating provides a quantitative value for carrier concentration in the semiconductor at each gate bias. Transistors were thus designed to attain high carrier concentrations in the semiconductor via bulk doping within the active layer. We chose the p-type semiconductor P3HT (**Figure 3.1a**) as a benchmark material with a well-studied morphology.[20-22] An aprotic PIL was used as the gate dielectric with an imidazolium-based cation (IM+) as a pendant group on the main chain and bis(trifluoromethane)sulfonimide ($TFSI^-$) as the free anion. Unlike other studies with polymer/ionic liquid gate insulators, only one ion can infiltrate the active layer. Integrating the current generated (I_G) and leakage current (I_L) upon applying a gate voltage (V_G) with time determines the total charge generated in the semiconductor (Q). Carrier density is calculated using Equation 3.1, where A is the area of charge accumulation and t is the thickness of the accumulation layer.[23] The high capacitance of the PIL dielectric has been shown to invoke a volumetric carrier density of 10^{20} –10^{21} cm^{-3} in the active layer using $V_G < |5|$ V due to the emergence of a conducting channel throughout the entire film.[3, 18, 24]

$$p = \frac{Q}{V} = \frac{\int (I_G - I_L)\, dt}{eAt} \qquad \text{Equation 3.1}$$

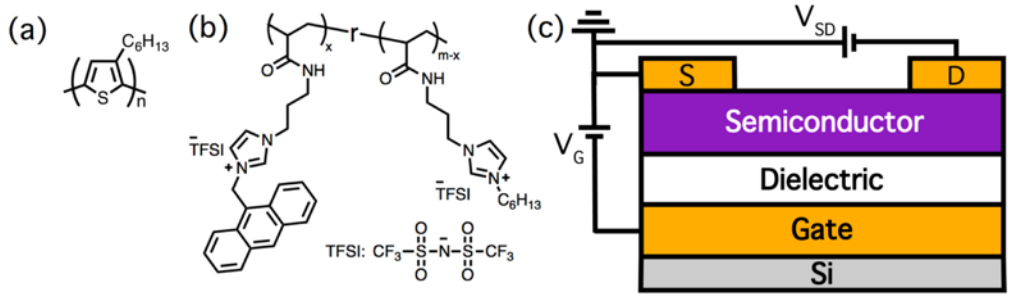

Figure 3.1. Chemical structures of (a) P3HT and (b) the anthracene-functionalized PIL IM-TFSI used as the gate dielectric. c) Schematic representation of the device used for electrical and structural characterization. L = 2 mm and W = 1 cm for structural characterization, and L = 150 μm and W = 2.7 mm for electrical characterization.

We positioned the semiconductor at a free interface within the transistor to enable morphological characterization to take place *operando* using X-ray scattering. Here, we utilized a cross-linked PIL to create a bottom-gate top-contact device geometry with P3HT supported by the gate insulator. Anthracene moieties were incorporated onto the PIL backbone to crosslink the polymer upon exposure to 365 nm light via a Diels–Alder dimerization reaction (**Figure 3.1b**). The anthracene dimers afford a free-standing crosslinked polymer film after irradiation without sacrificing ionic conductivity, as detailed in another publication.[25] To achieve a sharp semiconductor–dielectric interface, P3HT films were first spin cast and annealed on an OTS-treated substrate and then transferred to the PIL using a PDMS stamp (**Figure 3.1c**).

An important question in doped semicrystalline polymers is if charge carriers and their associated counterions are distributed homogenously among the crystalline and amorphous regions of the semiconductor. As a voltage is applied between the source and gate electrodes of the PIL-gated transistor (V_G), holes are injected into the semiconductor from the source along with TFSI− ions from the dielectric. A larger gate bias drives more charge carriers (and counterions) into the semiconductor. The transistor turns ON when enough charge is induced to create a conducting channel between the source and drain electrodes. The ON current of the OECT is also determined by the kinetics of the infiltration of ions into the semiconductor.[26] Current–voltage characteristics alone yield no information about whether the film is doped homogenously, or if there exist regions that are doped differently than others.

To address this issue, we examined the distribution of both charge carriers and counterions within the polymer's crystalline and amorphous domains.

Grazing incidence wide angle X-ray scattering (GIWAXS) measurements of the PIL-gated transistor indicate that in the unbiased state, no counterions penetrate the crystalline regions of the semiconductor film. A representative 2D GIWAXS image of the top-contact bottom-gate transistor (**Figure B1a**) shows that the P3HT crystallites in the transferred film exhibit an edge-on texture, where alkyl stacking is in the out-of-plane direction and π–π stacking is in the in-plane direction. Due to the device geometry and the incident angle, the 2D image also captures structural characteristics of the underlying PIL (**Figure B1b**, Supporting Information) evidenced by the amorphous haloes at 0.35, 0.80, and 1.35 $Å^{-1}$ (denoted P1, P2, and P3, respectively).[27] In its unbiased form, the alkyl stacking and π–π stacking distances of P3HT are 16.5 and 3.77 Å, similar to previously reported values[28] and imply that no ions have perturbed the crystalline packing prior to applying a voltage.

Gate biases larger than |1.5| V drive TFSI– counterions into the P3HT crystallites, leading to a modified structure within the crystalline regions. Because we sought to examine the doped state of P3HT rather than the kinetics of operation of OECTs, GIWAXS measurements are taken in the long time limit (once gate current is negligible) to determine the steady-state characteristics of the device. For these measurements, 60 s is sufficient to ensure the transistor is at steady state (Supplementary Information Section II). 1D line profiles in the out-of-plane (**Figure 3.2a**) and in-plane (**Figure 3.2b**) directions show that at gate bias less than |1.5| V, no structural changes are observed in the crystalline regions. At low bias, the TFSI– ions likely exist only in the amorphous regions of the film, consistent with electrochemical strain microscopy measurements of P3HT gated with an ionic liquid[29] and

from ex situ scattering experiments using ionic liquid gated OECTs.[30] Measurements performed ex situ prove useful to establish general changes in structure with gating, but a more quantitative understanding of the doping mechanism is difficult to ascertain due to issues arising from the cycled application and removal of the ionic liquid. As the magnitude of the bias increases, the alkyl stacking distance increases sharply to 18.5 Å (**Figure 3.2c**) along with a decrease in π–π stacking distance to 3.62 Å (**Figure 3.2d**). The structural changes observed suggest that the TFSI− counterions reside in the alkyl chains of the crystallites, consistent with other dopant molecules used for P3HT.[10, 31, 32] As expected, the positions of the scattering peaks of the PIL (P1, P2, and P3) are not influenced by application of a gate bias. Morphological changes exhibit reversibility at the onset of crystallite infiltration (−1.8 V), while higher negative bias (> |2| V) increases the time scale of reversibility (**Figure B2**). A device biased only under positive gate voltage does not induce any changes up to +3 V (**Figure B3**), indicating that IM+ cations tethered to the PIL backbone do not infiltrate the crystalline regions of the semiconductor layer.

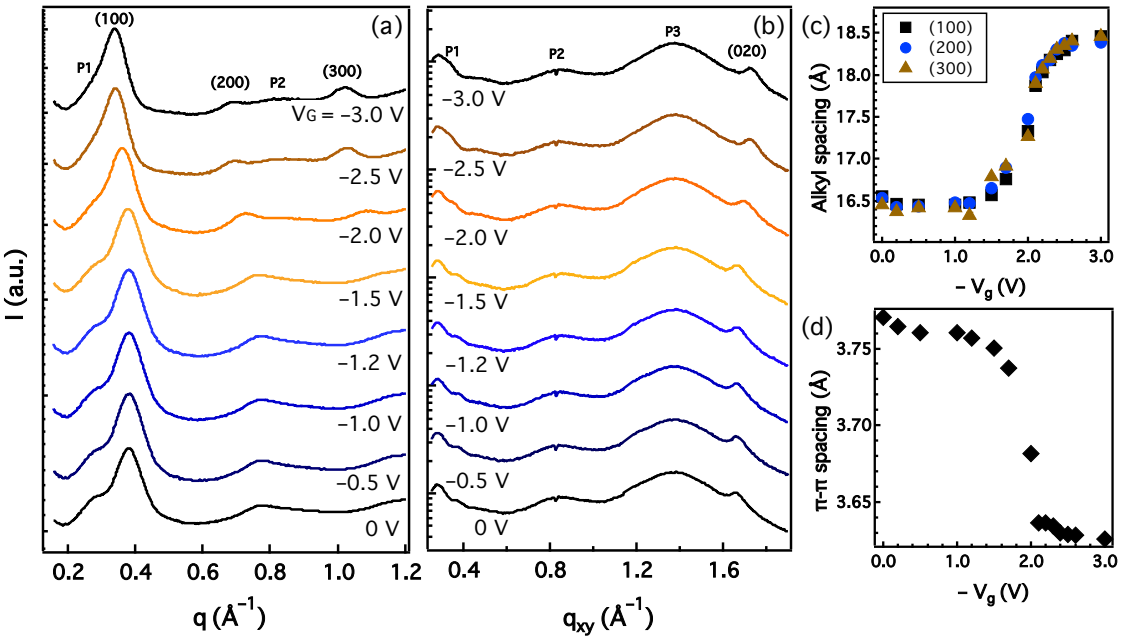

Figure 3.2. GIWAXS intensity along (a) a small sector near the inaccessible region of reciprocal space at grazing incidence near $q_z = 0$ and (b) the in-plane direction q_{xy} of P3HT as a function of gate bias. A bias is applied for 60 s before X-ray measurements take place to ensure a homogenous dopant profile in the semiconductor. Peaks arising from the underlying PIL dielectric are denoted as P1, P2, and P3. Peak fits show that at a critical bias of −1.5 V, the alkyl stacking distance begins to increase (c) with a concomitant decrease in the π–π stacking distance (d).

The 1D scattering profiles in **Figure 3.2** indicate that the crystallites expand as one population and do not become more disordered than their undoped state. Specifically, fits of the π–π stacking peak using a Lorentzian profile exhibit a constant full-width at half-maximum for all measurements, indicating that the disorder within the π stacks remain constant. Fits with two peaks either lead to unreasonable peak widths or peak areas inconsistent with the pristine film (**Figure B4**). Although the average ionic radius of TFSI– is approximately 4 Å,[33] the P3HT crystallites expand 2 Å (≈12%) in the out-of-plane direction and contract 0.15 Å (≈4%) in the in-plane direction. It is likely that the degree of free volume among the side chains of P3HT allows for ion intercalation with a small perturbation of the packing of the chains, consistent with other conjugated polymers.[34] For example, in P3HT

doped with the acceptor molecule F_4TCNQ, the alkyl spacing within the crystallites increases by approximately 2.5 Å with a counterion comparable to the size of TFSI–.[15] Upon TFSI– ion infiltration, new reflections do not emerge at any doping level, consistent with ex situ studies of ionic liquid gating[30] but unlike other dopants such as F_4TCNQ[35, 36] or I_2 vapor.[32] Previous studies have correlated new scattering peaks to polymer-dopant co-crystals or aggregation between dopant counterions, indicating that these events do not occur with the TFSI– counterion.

The sharp transition within the crystallites of P3HT upon doping takes place at carrier densities exceeding those achievable with non-ionic dielectrics. The onset of structural changes occurs at a carrier concentration of 4×10^{20} cm^{-3} in the PIL-gated device (**Figure 3.3**), which corresponds to approximately 5% of occupied sites assuming a density of 1.1 g cm^{-3} and two sites per monomer.[13] At lower carrier densities, the alkyl and π–π stacking distances remains unperturbed in the crystallites. For P3HT crystallites, injected polarons tend to delocalize over as many as 20 repeat units on one chain;[37, 38] thus, it is difficult to precisely quantify how many thiophene monomers each polaron affects upon oxidation. Structural changes stop at a carrier concentration of approximately 1×10^{21} cm^{-3} despite an increasing concentration of TFSI– counterions, which could indicate that further deformation in the crystallites becomes energetically unfavorable. These results capture the steady-state characteristics of the transistor, as the device is biased for sufficiently long times to ensure a distributed counterion profile within the film (**Figure B5**). The P3HT crystallites therefore exist in two distinct states as a function of carrier concentration: their pristine form for carrier density less than 4×10^{20} cm^{-3}, and their modified structure above 4×10^{20} cm^{-3} with a relatively abrupt transition in between.

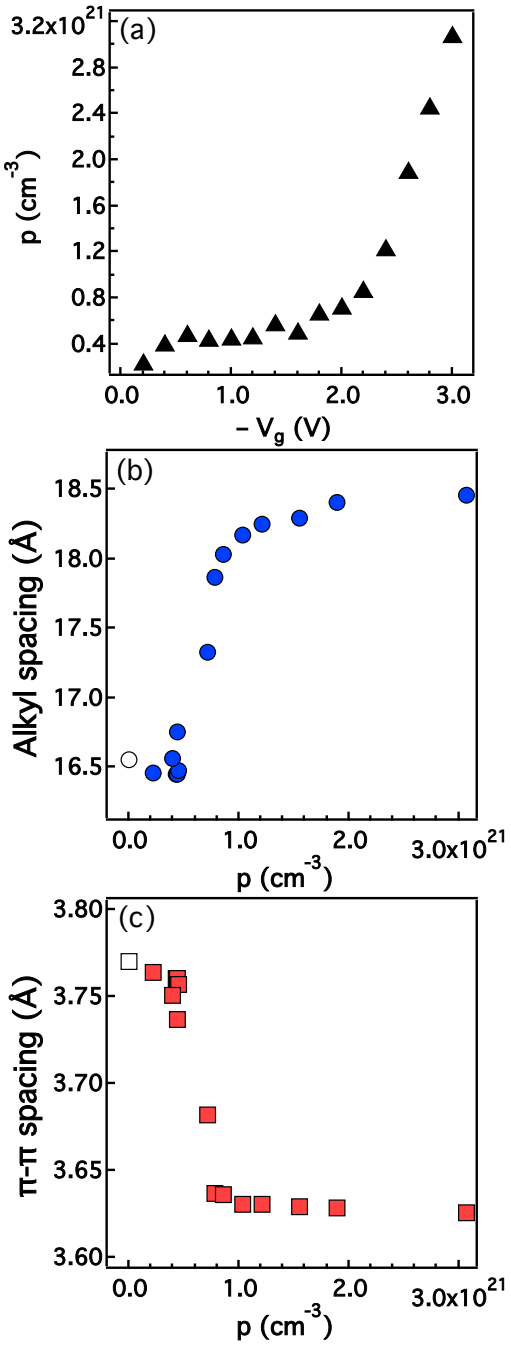

Figure 3.3. a) Carrier concentration calculated from integrating gate current (I_G) as a function of voltage. b) Alkyl and (c) π–π stacking distance as a function of carrier density. Unfilled symbols correspond to length scales at zero bias, which we assume corresponds to negligible carrier concentration.

While the distribution of counterions in the active layer is straightforward to interpret from **Figures 3.2** and **3.3**, the precise location of a charge carrier within semi-crystalline polymer films remains to be a topic of debate.[37, 39-44] The lower ionization energy in a crystallite of P3HT[45] has been shown to lead to increased doping efficiency and more delocalized polarons.[43,46] Some suggest that a carrier should be in close proximity to its associated counterion, regardless of the carrier concentration.[35,44] Previously, charge modulation spectroscopy, FTIR, and Raman spectroscopy have been used to study the local environment of polarons in conjugated polymers at low concentrations, typically to determine if holes exist as polarons or bipolarons.[37,39-41] It was found that P3HT undergoes charge-

induced conformational changes with doping,[47] but consensus has not been reached on if crystalline aggregates or amorphous regions are affected differently by the induced polarons.[48]

The aggregates formed within a P3HT film exhibit different UV–visible absorption spectra depending on the organization of neighboring chains within the aggregate. Chain segments that are staggered relative to each other will result in predominantly J-type behavior; these aggregates are known to exist in the less crystalline domains of P3HT. H-type aggregates exhibit an eclipsed chain orientation and exist in the more crystalline regions of the film.[49] Differences in chain orientation results in variation of the degree of excitonic coupling, evidenced by differences in the intensity of vibronic transitions between the ground and excited state (0–0, 0–1, etc.). As a result, H- and J-type aggregates of P3HT yield unique absorption spectra—namely, the ratio of the 0–0:0–1 transition is lower for H-type aggregates.[50] Spun-cast films of P3HT consist of primarily H-type aggregates, where the 0–0:0–1 ratio is typically between 0.6 and 0.8 in their undoped state. A larger 0–0:0–1 ratio corresponds to a longer conjugation length among the aggregates.[51] As the film is doped, tracking the intensity of the absorption at the 0–0 and 0–1 transition of the P3HT aggregates can reveal which aggregates are oxidized first, and therefore the preferential position of the injected hole polaron.

Optical spectroscopy of the PIL/P3HT bilayer show that the semiconductor exhibits primarily H-type aggregation in its unbiased state. Using a method developed by Spano et al., the optical spectra of an undoped P3HT film can be described using a modified Frank–Condon fit that incorporates effects of aggregation on the vibronic intensities of P3HT.[52] This model yields information about the primary aggregate type in the film and how much of the film is aggregated. Spectra are fit using a least-squares method with details in the

Supplementary Information (Section IV). Based on these calculations, the undoped film of P3HT contains approximately 50% aggregates, which is typical for spun-cast films of P3HT.

Hole polarons reside within the crystalline domains of the film for VG < |1| V, evidenced by the initial oxidation of H-type aggregates. Evolution of the absorption spectra of the P3HT/PIL bilayer with increasing gate bias (**Figure 3.4a**) contains an isosbestic point at 1.97 eV, indicating the transformation between coexisting neutral and charged polymer species. Mild undulations in the near-IR region corresponds to the interference between the electrodes of the bilayer (**Figure 3.4a**, inset). As the film is oxidized, the main optical transition of undoped P3HT decreases while the intensity of a sub-gap electronic transition at 1.6 eV increases, the latter being associated with the presence of polaronic carriers within the film.[53] At low carrier densities, the ratio between the 0–0 and 0–1 transition increases (**Figure 3.4b**), indicating that the neutral P3HT aggregates that remain exhibit more J-type behavior. Because the crystalline regions of the film exhibit predominantly H-type behavior,[49] we posit that the crystalline regions of the film are initially oxidized. This result is consistent with EPR and FTIR measurements with lightly doped P3HT.[43, 46] Since the TFSI– ions reside in the amorphous regions of the semiconductor at low carrier density (**Figure 3.3**), the crystallites are only oxidized at the interface between the amorphous and crystalline domains and neutralized by the counterions at the same interface. We conclude that all charges induced before the onset of structural changes reside in the crystalline regions of the film; thus, ≈10% of sites in the crystalline domains are occupied since about 50% of the film is amorphous. Although it is possible that a fraction of chains in the amorphous domains are oxidized initially, we expect this fraction to be small due to their small conjugation lengths (and thus, larger ionization energy) and the observed increase in the ratio between the 0–0 and 0–1 peak

intensity. As the carrier concentration increases, both H- and J-type aggregates are oxidized, evidenced by the elimination of vibronic structure in the optical spectra. Eventually, even the amorphous regions of the film are oxidized with an almost complete transition to the charged polymer species absorbing at 1.6 eV.

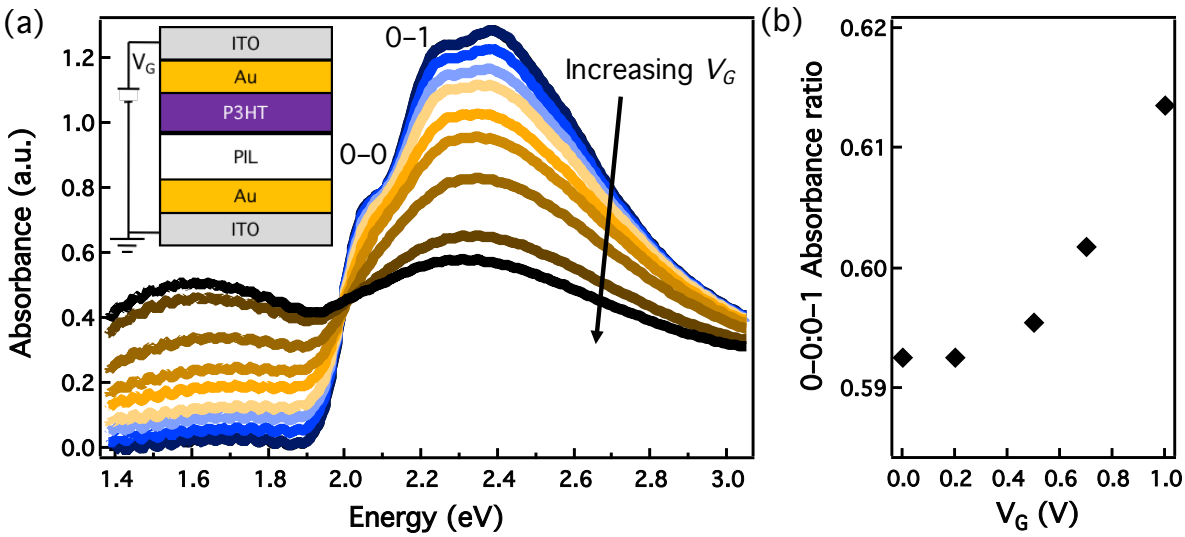

Figure 3.4. a) Evolution of the optical absorption spectrum of a P3HT/PIL bilayer with increasing bias. The inset shows a schematic representation of the bilayer device used for absorption measurements. b) Ratio between the 0–0 and 0–1 transition as a function of gate voltage.

The structural rearrangement in the crystallites of P3HT induced by counterion infiltration occurs alongside a drastic increase in the effective carrier mobility. Previous studies have postulated that mobility is a function of the degree of electronic disorder in conjugated polymers at high carrier density, where dopant-induced disorder dominates the breadth of the DOS.[2, 4, 5] Physical as well as electronic order strongly influence the electronic properties of a polymer, but a direct correlation between morphological changes and carrier mobility in doped polymers has yet to be established. The carrier mobility $\mu(p) = \sigma/ep$ increases sharply at the same carrier density as the onset of an apparent phase transition of the

P3HT crystallites as TFSI− enters (**Figure 3.5**). As more TFSI− ions enter the semiconductor, the mobility increases and reaches a maximum at a carrier density of 8×10^{20} cm^{-3}. This observation is consistent with previous work in P3HT when gated with an ionic liquid, where the mobility reached a plateau at comparable carrier concentration.[2] The maximum carrier mobility in the large devices examined was near 10^{-4} cm^2 V^{-1} s^{-1}. Factors such as interfacial roughness between the active layer and dielectric[54, 55] and mechanical cracks formed over the device size (>150 μm) during film transfer could contribute to a mobility that is lower than previous reports.[20, 56] A connection between the onset of crystalline phase changes and mobility enhancement should remain true regardless of the absolute mobility value.

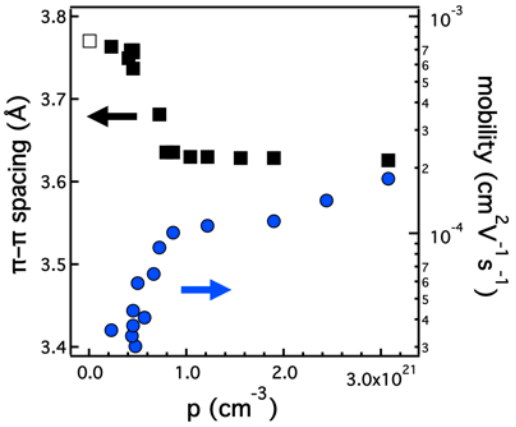

Figure 3.5. a) Dependence of carrier mobility with carrier concentration calculated from transistor output curves (blue circles) overlaid with the π–π stacking distance (black squares). Unfilled symbols correspond to length scales at zero bias, which we assume corresponds to negligible carrier concentration.

In light of these results, we suggest that a non-linear increase in the conductivity with doping is influenced by doping-induced structural rearrangement within the polymer crystallites. Previous reports of doping P3HT with F_4TCNQ suggest that charges induced in the semiconductor are strongly bound to their associated counterions, and disassociation between the charge and counterion leads to an increase in electrical conductivity.[1] Broadening

in the DOS due to the presence of counterions has also been postulated to cause the non-linear effects in electronic conduction.[2] In such cases, the carriers are suggested to be initially trapped and only become conductive as the DOS is filled. We offer an alternative explanation on the basis of our results. For this work, there exists three operational regimes within the steady-state limit of the PIL-gated transistor. For very low carrier density, TFSI− ions reside purely in the amorphous regions of P3HT with no disruption of the crystalline domains and holes primarily formed at the interface of the crystallites (**Figure 3.6a**). Higher carrier concentration leads to an expansion in the crystalline domains with a concomitant increase in carrier mobility (**Figure 3.6b**), where the J-aggregates are oxidized and act as tie chains between the crystalline regions. The changes in structure of the crystallites are weaker above carrier concentrations of $\approx 8 \times 10^{20}$ cm^{-3}. Finally, the amorphous regions dope at high carrier density, but do not have a strong influence on the carrier mobility (**Figure 3.6c**). The electrical conductivity and carrier mobility therefore increase from a combination of the formation of a percolated network within the film at high carrier density and the decrease in π–π stacking distance within the crystallites upon ion infiltration. While the presence of extended states in the semiconductor undoubtedly impacts the measured mobility,[1, 2] the location of the carriers within the ordered and disordered regions of the semiconducting polymer has been shown for the first time to play a critical role that is overlooked in many transport models.

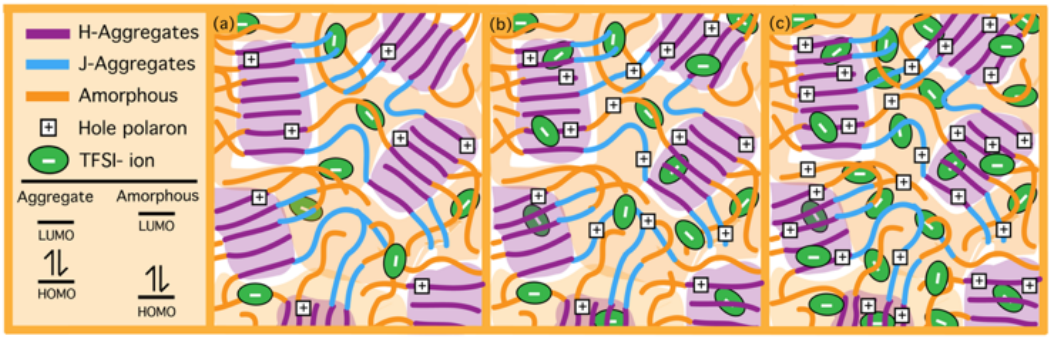

Figure 3.6. a) Schematic representation of the three operational regimes within the electrochemical transistor: prior to the onset of structural changes where the crystallite interfaces are oxidized, b) at the onset of structural changes when both H- and J- type aggregates are oxidized, and c) at high carrier concentration where both amorphous and aggregated regions of the film are oxidized.

3.4 Conclusions

The results herein indicate that a doped semiconducting polymer exhibits vastly different properties with respect to its pristine counterpart. From *operando* X-ray scattering experiments, we find that the crystalline structure of P3HT is perturbed at high carrier concentration by infiltration of counterions, which is correlated with an increase in carrier mobility. Additionally, hole polarons preferentially reside in the crystalline regions even at low carrier density, which may introduce a limit for the electrical conductivity at low carrier density if the crystalline regions are not well connected by extended tie chains. We expect that this effect could extend to other semicrystalline polymers, and that the structural rearrangement within the crystallites and connectivity of these domains dictates when methods that rely on delocalization of carriers, such as Hall effect measurements, can yield accurate data.[2]

The stark difference in the distribution of holes and counterions suggests that crystallinity and morphology both play an important role in how the semiconductor is doped. A sharp transition in crystal structure as a function of composition as shown in **Figure 3.3b** and **3.3c** likely signifies a phase transition within P3HT as it forms the alloy P3HT+:TFSI−. Doping-induced phase transitions have been observed in materials such as graphite intercalation compounds,[57, 58] but have not been widely studied with polymeric semiconductors. Exploring the role of crystallinity in electrochemically doped polymers, as well as strategies to reduce barriers to phase changes within a polymer film, as carrier concentration increases may yield insight into achieving an optimal morphology for high-performance organic electronics.

3.5 Acknowledgements

The authors acknowledge funding support from the Department of Energy Office of Basic Energy Sciences under grant no. DE-SC0016390 for all device fabrication, device characterization, and analysis. Synthesis of the anthracene-functionalized PIL made use of shared facilities of the UCSB MRSEC (NSF DMR 1720256), a member of the Materials Research Facilities Network (www.mrfn.org). E.M.T. gratefully acknowledges support from the w (DGE-1650114). This research used resources of the Advanced Light Source, which is a U.S. Department of Energy Office of Science User Facility under contract no. DE-AC02-05CH11231. The authors thank Christian

Müller, Jonna Hynynen, and Erik Fransson for useful discussion and the framework for fitting the optical spectra and Dr. Simon Bubel for early efforts on *operando* gating.

3.6 Appendix B

3.6.1 GIWAXS and line cut fitting analysis

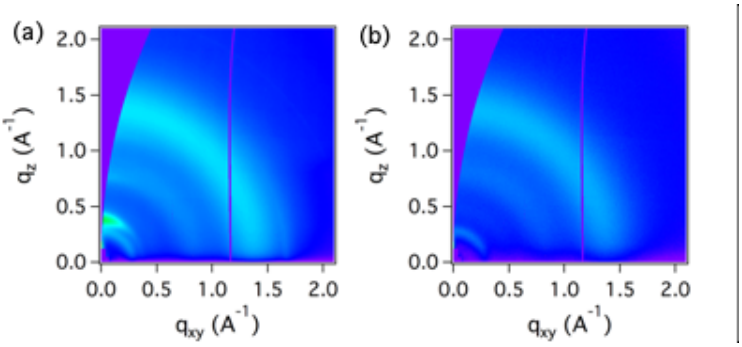

Figure B1. (a) Representative 2D GIWAXS image of the pristine P3HT/PIL device. Clear π–π stacking and alkyl stacking peaks are visible along with amorphous rings from the underlying PIL. (b) 2D GIWAXS of a crosslinked PIL film exhibits three amorphous halos at the same location as in the bilayer device.

As the structure of the crystallites evolve in the film upon ion infiltration, it is of interest to know the extent of reversibility of these changes. We find that soon after the onset of ion infiltration, the scattering pattern is able to revert back to its unbiased pattern within ten minutes, but only with the application of a gate bias of the opposite polarity (**Figure B2**, top). At very high gate bias, the pattern reverts back over much longer time scales than at lower gate voltages, even with positive bias (**Figure B2**, bottom).

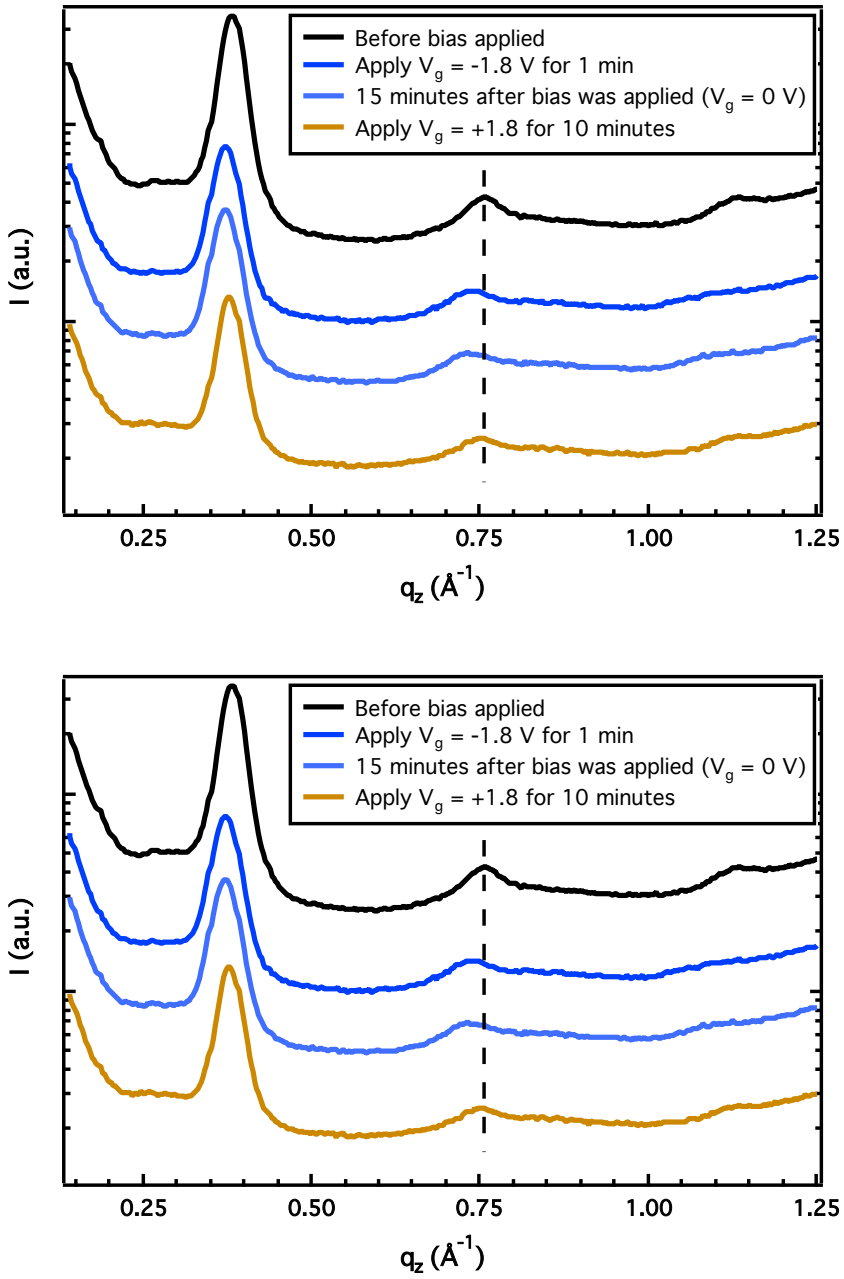

Figure B2. Reversibility of structural changes with various gate voltages. (Top) The P3HT crystallites exhibit reversibility in mid-range gate voltages, shortly after the critical bias was reached. (Bottom) After the sharp transition at sufficiently high bias, the crystallites revert back over much longer time scales. The crystallites do not completely revert back to their unbiased form after 15 minutes of positive biasing. Vertical dashed lines serve as a guide to the eye.

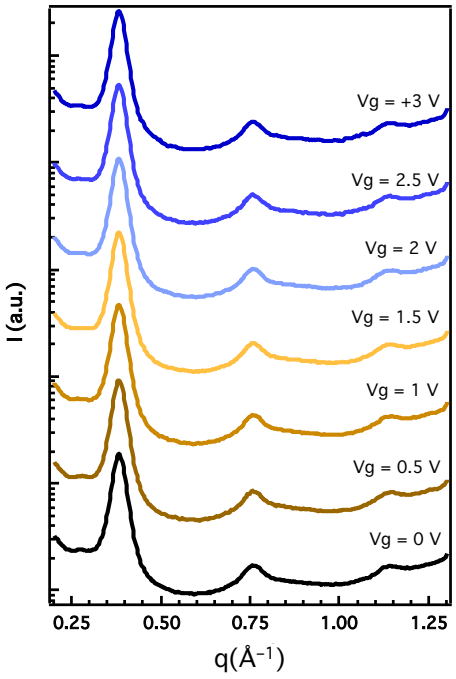

Figure B3. GIWAXS intensity along a small sector near the inaccessible region of reciprocal space at grazing incidence near $q_z = 0$ as a function of positive biasing of the PIL transistor. A positive gate bias drives the tethered IM+ cations to the semiconductor/dielectric interface and indicates that tethered ions do not penetrate the semiconductor layer.

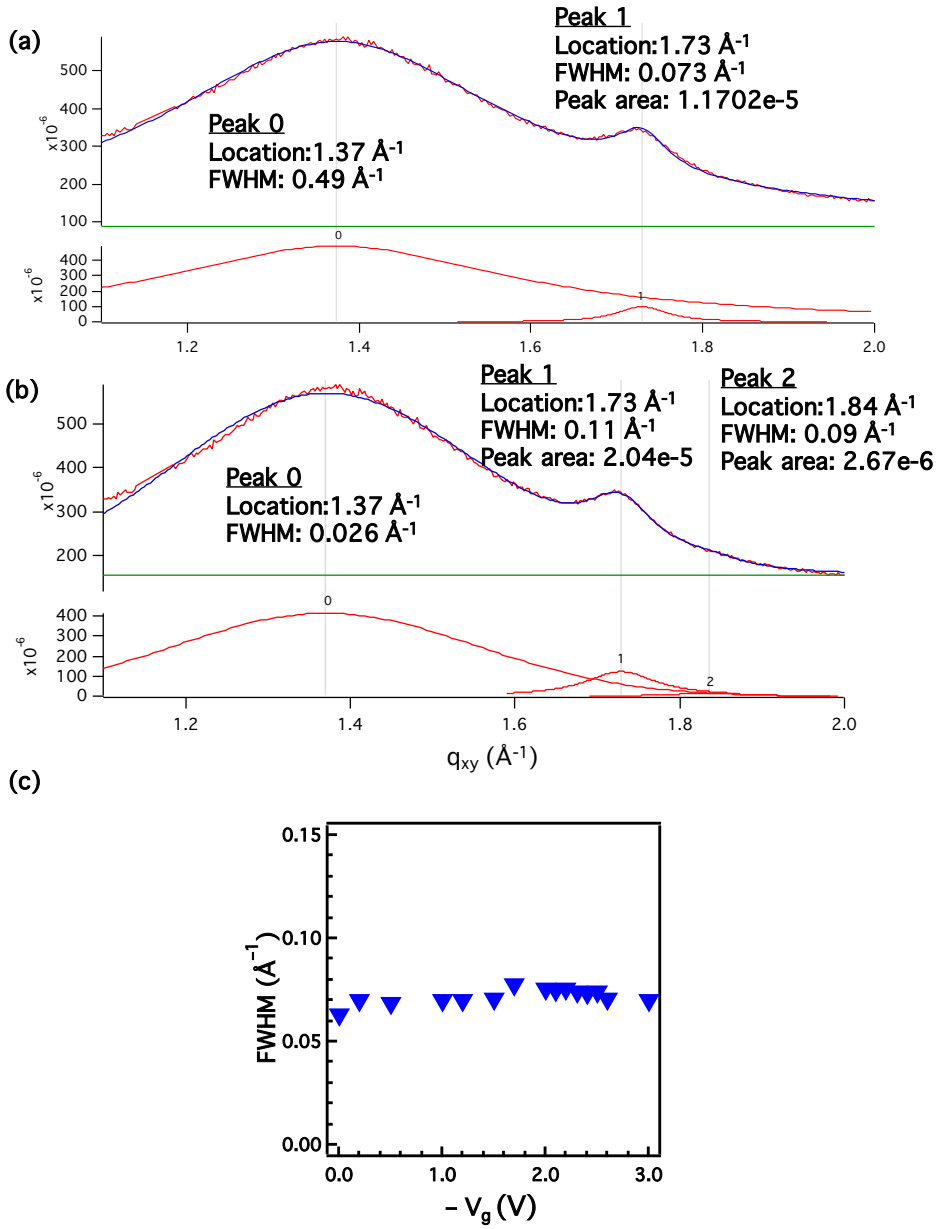

Figure B4. Peak fits testing the validity of one (a) versus two (b) π–π stacking peaks. The use of two Lorentzian peaks to fit the data near 1.7 Å^{-1} lead to a shift in the PIL peak at 1.37 Å^{-1} and with FWHM relatively larger than the FWHM for the π–stacking peak at low bias. Representative data is for -2.3 V. (c) Full width half maximum (FWHM) of P3HT π–π stacking peak with bias. There is no discernable change in the FWHM throughout the experimental range of gate voltage, indicating that two populations do not form within the crystallites and do not become more disordered as ions infiltrate the crystallites.

3.6.2 *Transistor characteristics*

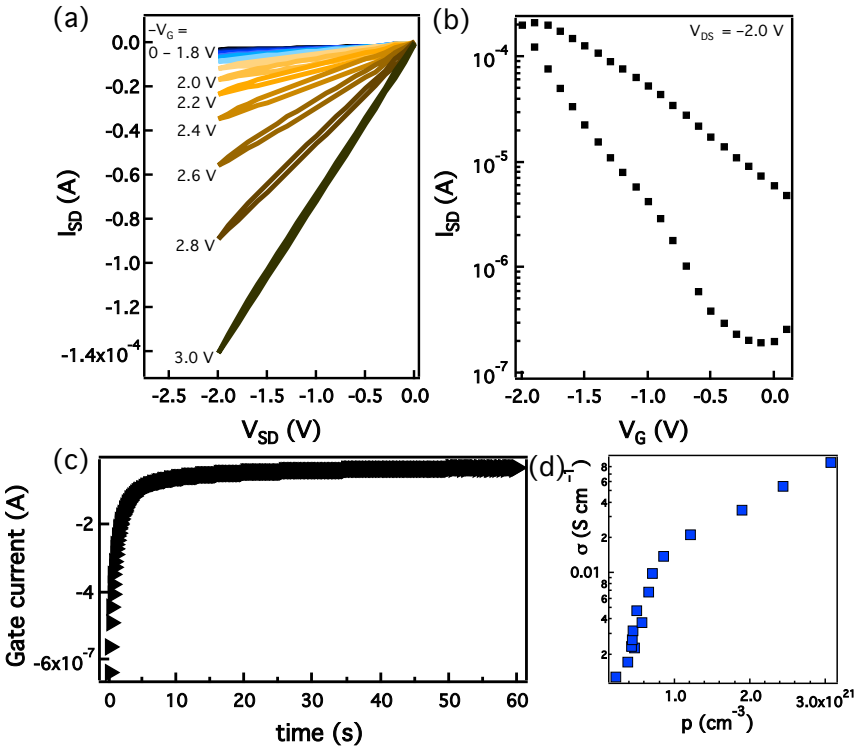

Figure B5. (a) Output and (b) transfer characteristics of the top-contact bottom-gate P3HT transistor. Here, W = 2.7 mm and L = 150 μm. (c) Representative plot of gate current as a function of time upon applying a bias at time t = 0. Measurements are taken after 60 seconds to ensure the device is at steady-state. (d) Electrical conductivity as a function of carrier concentration, obtained from linear current-voltage curves after 60 seconds of bias.

3.6.3 *Optical absorption analysis*

The model developed by Spano *et al.*[59, 60] describes the absorption spectra, *A*, of P3HT by the following:

$$A = C \sum_{m=0} \left(\frac{e^{-S} S^m}{m!}\right)\left(1 - \frac{W e^{-S}}{2E_p} \sum_{n \neq m} \frac{S^n}{n!\,(n-m)!}\right)^2 \exp\left(-\frac{\left(E - E_{0-0} - mE_p - 0.5WS^m e^{-S}\right)^2}{2\sigma^2}\right) \frac{}{\sigma\sqrt{2\pi}}$$

Equation B1

The Huang-Rhys factor, *S*, is assumed to be unity. The proportionality constant (*C*), excitonic bandwidth (*W*), Gaussian width (σ), and the 0-0 intrachain transition ($E_{0\text{-}0}$) are varying parameters in this model. The characteristic C=C phonon stretch is 0.179 eV for P3HT.

A Matlab code was utilized to perform a least-square fit for the 0–0, 0–1, 0–2, 0–3, and 0–4 transitions as a function of carrier density. A typical fit is shown in **Figure B6**. The 0–0:0–1 ratio is shown in the main text only for low charge density, as the model no longer fits at high doping levels.

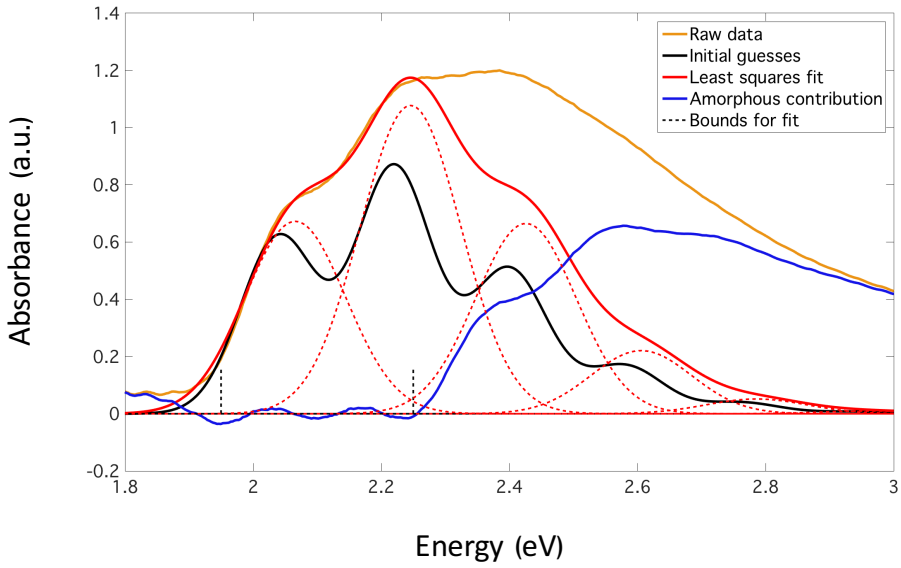

Figure B6. Fit of P3HT with the model developed by Spano *et al.* The intensity of the 0–0 and 0–1 transitions are compared as a function of gate bias to determine how the P3HT aggregates are oxidized in the low carrier density limit.

3.7 References

(1) P. Pingel, D. Neher, *Phys. Rev. B* 2013, **87**, 115209.
(2) S. Wang, M. Ha, M. Manno, C. D. Frisbie, C. Leighton, *Nat. Commun.* 2012, **3**, 1210.
(3) E. M. Thomas, B. C. Popere, H. Fang, M. L. Chabinyc, R. A. Segalman, *Chem. Mater.* 2018, **30**, 2965.
(4) V. I. Arkhipov, P. Heremans, E. V. Emelianova, H. Bässler, *Phys. Rev. B* 2005, **71**, 045214.
(5) G. Z. Zuo, Z. J. Li, O. Andersson, H. Abdalla, E. G. Wang, M. Kemerink, *J. Phys. Chem. C* 2017, **121**, 7767.
(6) M. L. Tietze, P. Pahner, K. Schmidt, K. Leo, B. Lüssem, *Adv. Funct. Mater.* 2015, **25**, 2701.

(7) J. Rivnay, R. M. Owens, G. G. Malliaras, *Chem. Mater.* 2014, **26**, 679.
(8) B. Russ, A. Glaudell, J. J. Urban, M. L. Chabinyc, R. A. Segalman, *Nat. Rev. Mater.* 2016, **1**, 16050.
(9) I. E. Jacobs, A. J. Moule, *Adv. Mater.* 2017, **29**, 1703063.
(10) S. N. Patel, A. M. Glaudell, D. Kiefer, M. L. Chabinyc, *ACS Macro Lett.* 2016, **5**, 268.
(11) K. H. Yim, G. L. Whiting, C. E. Murphy, J. J. M. Halls, J. H. Burroughes, R. H. Friend, J. S. Kim, *Adv. Mater.* 2008, **20**, 3319.
(12) I. E. Jacobs, E. W. Aasen, J. L. Oliveira, T. N. Fonseca, J. D. Roehling, J. Li, G. Zhang, M. P. Augustine, M. Mascal, A. J. Moulé, *J. Mater. Chem. C* 2016, **4**, 3454.
(13) T. J. Prosa, M. J. Winokur, J. Moulton, P. Smith, A. J. Heeger, *Phys. Rev. B* 1995, **51**, 159.
(14) J. L. Thelen, S.-L. Wu, A. E. Javier, V. Srinivasan, N. P. Balsara, S. N. Patel, *ACS Macro Lett.* 2015, **4**, 1386.
(15) S. N. Patel, A. M. Glaudell, K. A. Peterson, E. M. Thomas, K. A. O'Hara, E. Lim, M. L. Chabinyc, *Sci. Adv.* 2017, **3**, e1700434.
(16) J. Lee, L. G. Kaake, J. H. Cho, X. Y. Zhu, T. P. Lodge, C. D. Frisbie, *J. Phys. Chem. C* 2009, **113**, 8972.
(17) D. Venkateshvaran, M. Nikolka, A. Sadhanala, V. Lemaur, M. Zelazny, M. Kepa, M. Hurhangee, A. J. Kronemeijer, V. Pecunia, I. Nasrallah, I. Romanov, K. Broch, I. McCulloch, D. Emin, Y. Olivier, J. Cornil, D. Beljonne, H. Sirringhaus, *Nature* 2014, **515**, 384.
(18) D. Khodagholy, J. Rivnay, M. Sessolo, M. Gurfinkel, P. Leleux, L. H. Jimison, E. Stavrinidou, T. Herve, S. Sanaur, R. M. Owens, G. G. Malliaras, *Nat. Commun.* 2013, **4**, 2133.
(19) K. H. Lee, M. S. Kang, S. Zhang, Y. Gu, T. P. Lodge, C. D. Frisbie, *Adv. Mater.* 2012, **24**, 4457.
(20) H. Sirringhaus, P. J. Brown, R. H. Friend, M. M. Nielsen, K. Bechgaard, B. M. W. Langeveld-Voss, A. J. H. Spiering, *Adv. Mater.* 1999, **401**, 4.
(21) Y. Kim, S. Cook, S. M. Tuladhar, S. A. Choulis, J. Nelson, J. R. Durrant, D. D. C. Bradley, M. Giles, I. McCulloch, C.-S. Ha, M. Ree, *Nat. Mater.* 2006, **5**, 197.
(22) B. Grévin, P. Rannou, R. Payerne, A. Pron, J.-P. Travers, *Adv. Mater.* 2003, **15**, 881.
(23) T. Harada, H. Ito, Y. Ando, S. Watanabe, H. Tanaka, S. Kuroda, *Appl. Phys. Express* 2015, **8**, 021601.
(24) A. Giovannitti, D. T. Sbircea, S. Inal, C. B. Nielsen, E. Bandiello, D. A. Hanifi, M. Sessolo, G. G. Malliaras, I. McCulloch, J. Rivnay, *Proc. Natl. Acad. Sci. USA* 2016, **113**, 12017.
(25) B. C. Popere, G. E. Sanoja, J. M. Bartels, E. M. Thomas, M. E. Helgeson, M. L. Chabinyc, R. A. Segalman, *J. Mater. Chem. C* 2018, **6**, 8762.
(26) J. T. Friedlein, M. J. Donahue, S. E. Shaheen, G. G. Malliaras, R. R. McLeod, *Adv. Mater.* 2016, **28**, 8398.
(27) D. S. la Cruz, M. D. Green, Y. Ye, Y. A. Elabd, T. E. Long, K. I. Winey, *J. Polym. Sci. Part B Polym. Phys.* 2012, **50**, 338.
(28) D. T. Duong, C. Wang, E. Antono, M. F. Toney, A. Salleo, *Org. Electron.* 2013, **14**, 1330.

(29) R. Giridharagopal, L. Q. Flagg, J. S. Harrison, M. E. Ziffer, J. Onorato, C. K. Luscombe, D. S. Ginger, *Nat. Mater.* 2017, **16**, 737.
(30) J. O. Guardado, A. Salleo, *Adv. Funct. Mater.* 2017, **27**, 1701791.
(31) E. Lim, K. A. Peterson, G. M. Su, M. L. Chabinyc, *Chem. Mater.* 2018, **30**, 998.
(32) K. Tashiro, M. Kobayashi, T. Kawai, K. Yoshino, *Polymer* 1997, **38**, 2867.
(33) S. Zhang, N. Sun, X. He, X. Lu, X. Zhang, *J. Phys. Chem. Ref. Data* 2006, **35**, 1475.
(34) N. C. Miller, E. Cho, R. Gysel, C. Risko, V. Coropceanu, C. E. Miller, S. Sweetnam, A. Sellinger, M. Heeney, I. McCulloch, J.-L. Brédas, M. F. Toney, M. D. McGehee, *Adv. Energy Mater.* 2012, **2**, 1208.
(35) D. T. Scholes, P. Y. Yee, J. R. Lindemuth, H. Kang, J. Onorato, R. Ghosh, C. K. Luscombe, F. C. Spano, S. H. Tolbert, B. J. Schwartz, *Adv. Funct. Mater.* 2017, **27**, 1702654.
(36) H. Méndez, G. Heimel, S. Winkler, J. Frisch, A. Opitz, K. Sauer, B. Wegner, M. Oehzelt, C. Röthel, S. Duhm, D. Többens, N. Koch, I. Salzmann, *Nat. Commun.* 2015, **6**, 8560.
(37) T. Mills, L. G. Kaake, X.-Y. Zhu, *Appl. Phys. A* 2009, **95**, 291.
(38) S. Kuroda, K. Marumoto, T. Sakanaka, N. Takeuchi, Y. Shimoi, S. Abe, H. Kokubo, T. Yamamoto, *Chem. Phys. Lett.* 2007, **435**, 273.
(39) L. G. Kaake, X.-Y. Zhu, *J. Phys. Chem. C* 2008, **112**, 16174.
(40) P. J. Brown, H. Sirringhaus, M. Harrison, M. Shkunov, R. H. Friend, *Phys. Rev. B* 2001, **63**, 125204.
(41) N. Zhao, Y.-Y. Noh, J.-F. Chang, M. Heeney, I. McCulloch, H. Sirringhaus, *Adv. Mater.* 2009, **21**, 3759.
(42) J. Fuzell, I. E. Jacobs, S. Ackling, T. F. Harrelson, D. M. Huang, D. Larsen, A. J. Moulé, *J. Phys. Chem. Lett.* 2016, **7**, 4297.
(43) J. Gao, J. D. Roehling, Y. Li, H. Guo, A. J. Moulé, J. K. Grey, *J. Mater. Chem. C* 2013, **1**, 5638.
(44) A. R. Chew, R. Ghosh, Z. Shang, F. C. Spano, A. Salleo, *J. Phys. Chem. Lett.* 2017, **8**, 4974.
(45) K. R. Graham, C. Cabanetos, J. P. Jahnke, M. N. Idso, A. El Labban, G. O. Ngongang Ndjawa, T. Heumueller, K. Vandewal, A. Salleo, B. F. Chmelka, A. Amassian, P. M. Beaujuge, M. D. McGehee, *J. Am. Chem. Soc.* 2014, **136**, 9608.
(46) J. Gao, E. T. Niles, J. K. Grey, *J. Phys. Chem. Lett.* 2013, **4**, 2953.
(47) A. R. Chew, A. Salleo, *MRS Commun.* 2017, **7**, 728.
(48) P. Pingel, M. Arvind, L. Kölln, R. Steyrleuthner, F. Kraffert, J. Behrends, S. Janietz, D. Neher, *Adv. Electron. Mater.* 2016, **2**, 1600204:1.
(49) A. Köhler, H. Bässler, *Electronic Precesses in Organic Semiconductors: An Introduction*; Wiley-VCH: Weinheim, Germany, 2015.
(50) H. Yamagata, C. M. Pochas, F. C. Spano, *J. Phys. Chem. B* 2012, **116**, 14494.
(51) J. Hynynen, D. Kiefer, L. Y. Yu, R. Kroon, R. Munir, A. Amassian, M. Kemerink, C. Müller, *Macromolecules* 2017, **50**, 8140.
(52) J. Clark, J.-F. Chang, F. C. Spano, R. H. Friend, C. Silva, *Appl. Phys. Lett.* 2009, **94**, 163306.
(53) N. Colaneri, M. Nowak, D. Spiegel, S. Hotta, A. J. Heeger, *Phys. Rev. B* 1987, **36**, 7964.

(54) L.-L. Chua, P. K. H. Ho, H. Sirringhaus, R. H. Friend, *Adv. Mater.* 2004, **16**, 1609.
(55) M. L. Chabinyc, R. Lujan, F. Endicott, M. F. Toney, I. McCulloch, M. Heeney, *Appl. Phys. Lett.* 2007, **90**, 233508.
(56) Z. Bao, A. Dodabalapur, A. J. Lovinger, *Appl. Phys. Lett.* 1996, **69**, 4108.
(57) A. Van der Ven, J. Bhattacharya, A. A. Belak, *Acc. Chem. Res.* 2013, **46**, 1216.
(58) J. Zou, C. Sole, N. E. Drewett, M. Velický, L. J. Hardwick, *J. Phys. Chem. Lett.* 2016, **7**, 4291.
(59) Spano, F. C. *J. Chem. Phys*. 2005, *122*, 234701.
(60) Spano, F. C. *Chem. Phys*. 2006, *325*, 22–35.

Chapter 4

Doping-induced disorder affects the thermoelectric properties of polymeric semiconductors

A fundamental understanding of charge transport in polymeric semiconductors requires knowledge of how the electrical conductivity varies with carrier density. The thermopower of semiconducting polymers is also a complex function of carrier density making it difficult to assess structure–property relationships for the thermoelectric power factor. We examined the thermoelectric properties of poly[2,5-bis(3-tetradecylthiophen-2-yl)thieno[3,2-b]thiophene] (pBTTT-C_{14}) by measurements of an electrochemical transistor using a polymeric ionic liquid (PIL) gate dielectric that can modulate the carrier concentration from 4×10^{18} to 3×10^{20} cm^{-3}. As carrier density increases, so does the concentration of associated counterions, leading to a greater degree of energetic disorder within the semiconductor. Using thermopower measurements, we show experimentally that the electronic density-of-states broadens with increasing carrier density in the semiconducting polymer. The origin of a commonly observed power law relationship between thermopower and electrical conductivity is discussed and related to the changes in the electronic density-of-states upon doping.

4.1 Introduction

Doping is an important process for controlling the electrical properties of semiconductors.[1] In contrast to the substitution of atomic donors or acceptors into inorganic semiconductors,

a common method to modify the carrier concentration in semiconducting polymers is to introduce electron-deficient (or electron-rich) molecules, usually from solution or from the vapor phase, to oxidize (or reduce) the polymer backbone.[2,3] In this case, the dopant molecule, now ionized, is the counterion to the charged backbone. Protonating the polymer backbone with a Brönsted acid provides a similar effect with the proton donor acting as the counter-ion.[4] Alternatively, electrochemical methods can be used to supply or remove electrons but frequently require the polymer to be supported on a conductive substrate. Addition of dopants, or counterions, can increase the concentration of charge carriers in the polymer but concomitantly increase energetic disorder within the material due to structural perturbations.

Emerging applications for semiconducting polymers including thermoelectrics[5] and bioelectronics[6] rely on tuning the conductivity by either molecular or electrochemical doping. Here, we examine how changes in the electronic density-of-states (DOS) of a semiconducting polymer occur during electrochemical doping. By using an electrochemical transistor (OECT), we measured the changes in conductivity and thermopower of poly[2,5-bis(3-tetradecylthiophen-2-yl)thieno[3,2-b]thiophene] (pBTTT-C_{14}) as a function of carrier concentration. Controlling charge density provides a way to develop robust transport models for doped organic semiconductors and guide new materials design.

Studying the thermoelectric behavior in semiconducting polymers is one route to understand their transport properties and changes in the DOS upon doping. The carrier concentration, *p*, contributes to the physical properties of the semiconductor that determine its thermoelectric performance, including thermopower (α), electrical conductivity (σ), and thermal conductivity (κ). The general equation for thermopower is defined in Equation 4.1

where df(E)/dE = −f(E)(1 − f(E))/k_BT is the derivative of the Fermi–Dirac function f(E), E_F is the Fermi energy, and σ(E) is a transport function of electrical conductivity with energy.

$$\alpha = -\frac{k_B}{e}\int \frac{E-E_F}{k_BT}\frac{\sigma(E)}{\sigma}\frac{df(E)}{dE}dE \qquad \text{Equation 4.1}$$

If transport is mostly dominated by carriers around the Fermi level, thermopower can be rewritten as Equation 4.2.[7]

$$\alpha = \frac{\pi^2}{3}\frac{k_B^2T}{3}\left\{\frac{d(\ln\sigma(E))}{dE}\right\}_{E=E_F} \qquad \text{Equation 4.2}$$

The sign and magnitude of thermopower is determined by the slope of ln(σ(E)) at the Fermi level, which in turn is dependent on the occupancy of the electronic density-of-states.[7] Thermopower measurements are therefore an experimental method to ascertain the Fermi level if the functional form for σ(E) is known.

The electrical conductivity of semiconducting polymers is a complex function of the carrier concentration due to energetic disorder.[8-10] The majority of current transport models for semiconducting polymers use a hopping model with a density-of-states based on either a Gaussian function or a Mott-type model with a free-electron gas form combined with an exponential tail of states below a mobility edge.[11,12] For both of these models, the carrier density is required to rationalize transport data. Measuring the carrier concentration in doped polymers is notoriously difficult due to the emergence of bipolarons, which are silent in EPR,[13] and the energetic disorder present in many polymers, which makes interpretation of Hall effect measurements challenging.[14] A method to experimentally determine carrier density is thus imperative to evaluate transport models in disordered systems.

Field-effect gating controls carrier density in a semiconductor by applying biases to the terminal of a transistor.[15] An advantage of field-effect gating is quantification of the total

charge induced in the semiconductor, *p*, and the ease of changing it experimentally. In transistors, carriers are induced in the semiconductor in a thin, ~2 nm, conducting channel at the interface between the semiconductor and dielectric.[16] More recently, ion-containing gate dielectrics have been used to dope semiconductors through an electrical double layer or electrochemically by allowing ions in the dielectric to infiltrate the semiconductor layer.[17] Infiltration of ions into the active layer permits a 3D active channel of charge carriers rather than a channel only at the dielectric–semiconductor interface. As a result, the range of carrier density differs between the two devices. The maximum carrier density using conventional dielectrics, such as SiO_2, approach 10^{19} cm^{-3} above which dielectric breakdown occurs from the applied field, while electrochemical transistors have accessed carrier densities approaching 10^{21} cm^{-3}.[14,18,19] This broad range of carrier density can probe transport behavior over a wide range of doping levels from where traps may dominate ($<\sim10^{19}$ cm^{-3}) to concentrations where extended state conduction may occur.

Herein, we employ a polymeric ionic liquid (PIL) as the gate dielectric to investigate thermoelectric transport of a *p*-type semiconductor in an OECT geometry. To eliminate unwanted ion-pair diffusion into the semiconducting layer, a single-ion conducting PIL restricts ion motion to one species by tethering one ion to the polymer backbone. This unique OECT architecture therefore provides a model system to study the influence of doping on thermoelectric charge transport over a large range of carrier density. We find that high doping levels induce significant broadening in the polymer density-of-states, signifying that a balance exists between high electrical conductivity and a well-ordered electronic structure.

4.2 Experimental Methods

Materials: pBTTT-C14 was synthesized using a literature procedure.[48] All solvents were anhydrous and purchased from Sigma-Aldrich. Gold foil for top gates was purchased from Alfa Aesar. The IM-TFSI PIL was synthesized via reversible addition-fragmentation chain-transfer (RAFT) polymerization, with the detailed synthetic scheme in the Supporting Information.

Device Fabrication: Top-gate bottom-contact thin film transistors were fabricated in a nitrogen filled glovebox. Source and drain electrodes (20 nm Au) were thermally evaporated on glass substrates using a shadow mask. Channel lengths varied between 100 and 150 μm, and channel widths were 2700 μm. A solution of pBTTT-C_{14} (5 mg mL^{-1}, chlorobenzene) was spuncast at 1000 rpm for 1 min and annealed at 180 °C for 10 min affording a film thickness of approximately 25 nm as measured by atomic force microscopy. A PIL solution (50 mg mL^{-1}, acetonitrile) was dropcast in a PDMS mold to cover the semiconducting channels and annealed under vacuum at 70 °C overnight. Once annealed, the mold was removed to access the gold contacts. Gold foil was placed on top of the annealed PIL to act as the gate electrode.

Thermopower Metrology: The device geometry used in this work necessitated a protocol to measure S, σ, and n in the same experiment. To compensate for slow ion diffusion, measurements began several minutes after applying a gate bias. Thermopower was obtained by applying a series of four temperature differences between the source and drain; the resulting voltage was recorded. Electrical conductivity was calculated from resistance measurements. Carrier concentration was calculated using Equation 4.2, where the full semiconductor thickness was used as a conservative estimate of p. Thus, each gate bias yielded

a set of values for the thermoelectric properties of interest. More detail regarding the protocol is found in **Figure C3.**

4.3 A PIL-Gated Transistor Provides Controllable Carrier Concentration for Thermoelectric Transport

Gated measurements allow for the study of both thermopower and electrical conductivity of a material.[19–21] The device structure and materials examined here are shown in **Figure 4.1**. The p-type semiconducting polymer, pBTTT-C_{14} (**Figure 4.1a**), was chosen as the active layer due to its high carrier mobility in thin film transistors (~1 $cm^2 V^{-1} s^{-1}$).[22,23] An aprotic PIL was used as the gate dielectric with an imidazolium-based cation, denoted IM^+, on the main chain and bis(trifluoromethane)sulfonimide ($TFSI^-$) as the free anion (**Figure 4.1a**). In many ionic liquid-gated transistors, an ionic liquid is blended with a host polymer allowing both the cation and anion to be mobile.[24] Polyelectrolyte gate dielectrics, typically with a proton as the cation, can only *p*-dope the semiconductor interfacially which limits the range of achievable carrier concentration.[25,26] With the PIL, the cation is covalently linked the polymer backbone and immobile, while $TFSI^-$ is mobile and acts as the counterion to holes induced in the bulk of the semiconductor. Dielectric spectroscopy measurements show that the IM-TFSI PIL exhibits maximum capacitance of around 1 μF cm^{-2} at low frequencies (**Figure C1**), comparable to an IL with the same ionic species.[27] A high-capacitance dielectric allows for a large concentration of charge to be induced without the need to apply large biases; a block copolymer PIL synthesized previously[28] exhibited a maximum capacitance of 3 μF cm^{-2} and threshold voltage of −0.75 V in a transistor.

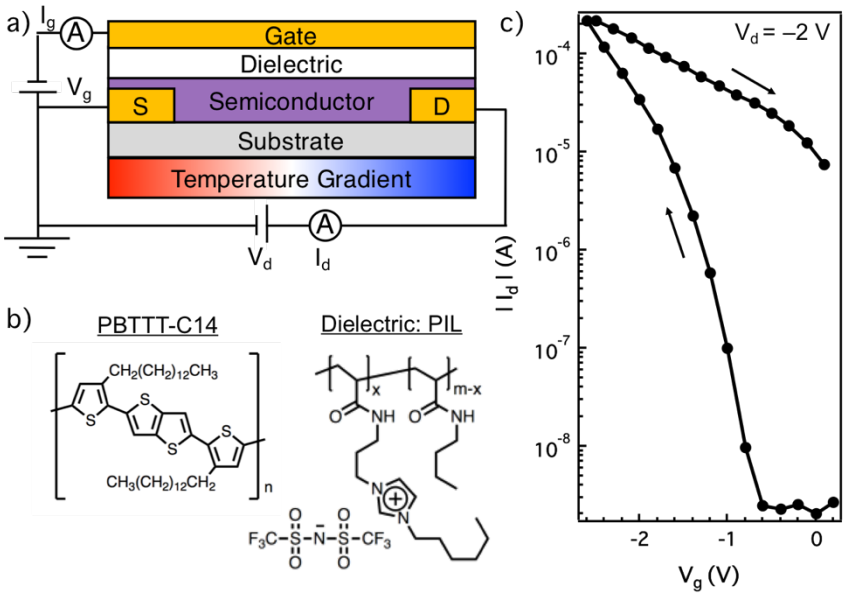

Figure 4.1. (a) Schematic representation of the TGBC OFET structure used for thermoelectric and electrical measurements; (b) Chemical structures of the polymeric ionic liquid (PIL) and p-type semiconductor (pBTTT-C_{14}) used in this work; x = 0.9. (c) PIL transistor transfer curve using a scan rate of 3.3 mV/sec.

The basic characteristics of the PIL-gated transistor are similar to IL-gated transistors (**Figure 4.1b**). As a negative bias between source and gate (V_G) is applied, the device acts similar to a capacitor, where charge builds up at both interfaces of the dielectric. Holes are injected into the semiconducting layer from the source electrode, whose charge is then compensated by $TFSI^-$ from the PIL dielectric. Tracking the current generated (I_G) with time determines the total charge generated in the semiconductor (Q). Carrier concentration is calculated by Equation 4.3, where A is the area of charge accumulation and t is the thickness of the accumulation layer.[29]

$$p = \frac{Q}{V} = \frac{\int I_G - I_L dt}{eAt} \qquad \text{Equation 4.3}$$

In this work, it is assumed that the semiconductor volume remains constant during gating. Previous work has shown that infiltration of external molecules can perturb the crystalline domains of the semiconductor, as observed by an ~10% increase in the alkyl stacking direction

and decrease in π–π stacking distance at high dopant concentration.[2,30] As there is no direct method available to measure polymer swelling as a function of gate bias in this work, we take this as a possible source of a small systematic error.

Charges induced in the semiconductor generate a current between source and drain, I_D, as a source-drain bias (V_D) is applied. Drain current is linearly proportional to V_D at low bias (i.e., the "linear regime"), with the slope related to the semiconductor resistance. The transfer characteristics of the PIL-gated transistor in **Figure 4.1c** show that the device turns ON at approximately −0.6 V, consistent with the high capacitance of the dielectric. Hysteresis between forward and backward sweeps in the transfer curve is also observed in **Figure 4.1c**, which is commonly seen in devices with ion-based gate dielectrics.[31]

The PIL gate provides a means to control thermopower and electrical conductivity over a large range of carrier concentration, shown in **Figure 4.2**. Because the PIL capacitance is frequency dependent, it is important that measurements reflect the relevant time scales of ion motion; ultimately, the steady-state properties of the semiconductor are of interest rather than sweep-rate dependent characteristics. As a result, a protocol to verify the measurement was carried out at steady state was used (see Experimental Section and Supporting Information). As the transistor turns ON, holes are injected from the source electrode along with $TFSI^-$ ions diffusing from the PIL dielectric to act as the countercharge. Higher bias leads to more occupied states in the semiconductor, thus increasing the doping level. As a result, larger bias leads to smaller thermopower as carrier concentration increases. On the basis of the crystallographic unit cell, we estimate a maximum number of states of approximately 2.0×10^{21} cm^{-3} in pBTTT, assuming each monomer can contribute 2 electrons.[16] The maximum calculated carrier density from the PIL is 3×10^{20} cm^{-3}, corresponding to 0.3 charges per

monomer. Incorporating a maximal swelling of the semiconductor layer upon ion infiltration introduces an error of approximately 10% for carrier concentration at the highest carrier densities. The ability to modulate the carrier concentration from 10^{18} to greater than 10^{20} cm^{-3} has been observed previously using ion gels and ionic liquids as gate dielectrics;[14,20] in this work, constraining the cation to remain in the dielectric ensures that one induced charge corresponds to only one additional ion within the semiconductor. This range of carrier density gives rise to a broad window to explore transport phenomena while maintaining control over Fermi level in the semiconductor.

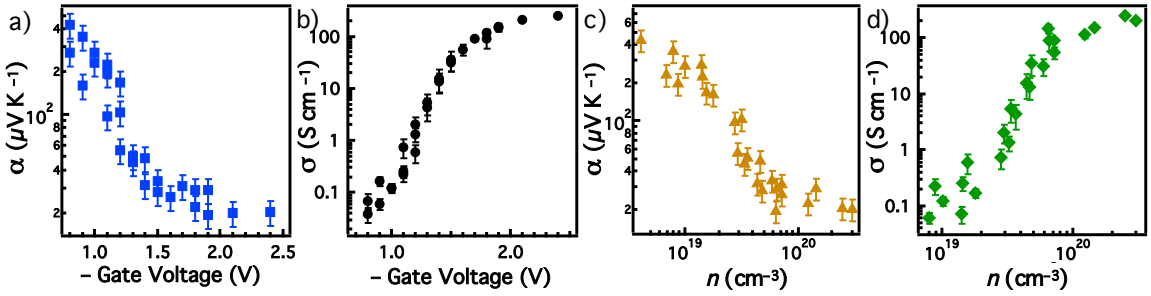

Figure 4.2. (a) Thermopower and (b) electrical conductivity measured over the range of gate voltages used; (c) Thermopower and (d) electrical conductivity as a function of carrier concentration calculated through integrating gate current.

We measured both α and σ over the accessible range of *p* to determine the relationship between the three parameters. As carrier concentration increases, electrical conductivity increases and plateaus around 200 S cm^{-1} while the thermopower decreases followed by a similar plateau. Rather than changing sign, the minimum thermopower of ~20 μV K^{-1} occurs at approximately −1.5 V, meaning that the slope $d(ln(\sigma(E)))/dE$ remains positive for all values of carrier concentration (Equation 4.2). These values are relatively consistent with studies of pBTTT that modulate α and α through acid doping in solution[2] and ion gel gating.[20] However,

carrier concentration must be known to truly compare thermopower values between samples. Conductivity normally acts as a proxy for carrier concentration, but film processing conditions can affect conductivity for a given carrier concentration which enables a range of conductivity values for a given value of the Seebeck coefficient.[5]

4.4 Predictive Models for Density-of-States Indicate Broadening in the High Carrier Concentration Limit

With the knowledge of the conductivity and thermopower, we can apply models previously used to interpret the thermopower of doped semiconducting polymers. One model developed by Emin and co-workers for polaronic species combines entropic and vibronic contributions of carriers to the thermopower described in Equation 4.4 to account for entropy of mixing (N is the total number of sites; n is the occupied number of sites), spin degeneracy, and effects of polarons on molecular vibrations (α_{vib}).[16]

$$\alpha = \frac{k_B}{e}\ln\left(\frac{N-n}{n}\right) + \frac{k_B}{e}\ln(2) + \alpha_{vib} \qquad \text{Equation 4.4}$$

This formalism has been used for previous work in field-effect transistors but is only valid when $n \ll N$, the maximum number of thermally accessible states, which does not strictly apply for the range examined here (**Figure C2**).

Others have turned to electrical conductivity as a proxy for p in conventional doping methods when carrier concentration is difficult to measure. A multitude of semiconducting polymers exhibit a power law trend between thermopower and conductivity, which was observed in previous studies and was fit empirically to $\alpha \propto \sigma^{-1/4}$ in previous work.[32,33]

A recent formalism developed by Kang and Snyder defined a transport function, σ_E, to further explain the α–σ relationship.[34] The transport function is described in Equation 4.5,

where σ_{E0} is a transport coefficient that is dependent on temperature but independent of energy and *s* is the transport parameter. E_T is the transport "edge", below which no conduction is expected to occur.

$$\sigma_E(E,T) = \sigma_{E0}(T)\left(\frac{E-E_T}{k_bT}\right)^s \qquad \text{Equation 4.5}$$

E_T is different from a Mott-like mobility edge E_C, because Mott's model assumes extended state transport only above E_C rather than the possibility of hopping conduction above E_T in the Kang and Snyder model. In the degenerate limit relative to the transport edge, the thermopower can be defined in terms of conductivity, the transport parameter, and the transport coefficient from Equation 4.6, leading to a scaling law of $\alpha \propto \sigma^{-1/s}$ for heavily doped polymers.

$$\alpha = \frac{k_B}{e}\frac{\pi^2}{3}s\left(\frac{\sigma}{\sigma_{E0}}\right)^{-1/s} \qquad \text{Equation 4.6}$$

The value of s is currently not predictable by the model and is a parameter chosen to fit experimental data.

Due to the ability to vary electrical conductivity and thermopower *via* gating, we can access the relationship between conductivity and thermopower and also both as a function of the carrier concentration. The scaling relationship is clearly observed from **Figure 4.3** over a wide range of known carrier concentration. The α–σ power law trend from this work is best fit with a slope of −1/3 (blue trace); a slope of −1/4 is also shown in comparison, which fits reasonably well to the higher conductivity data but deviates below $\sigma \approx 1$ S cm^{-1}.

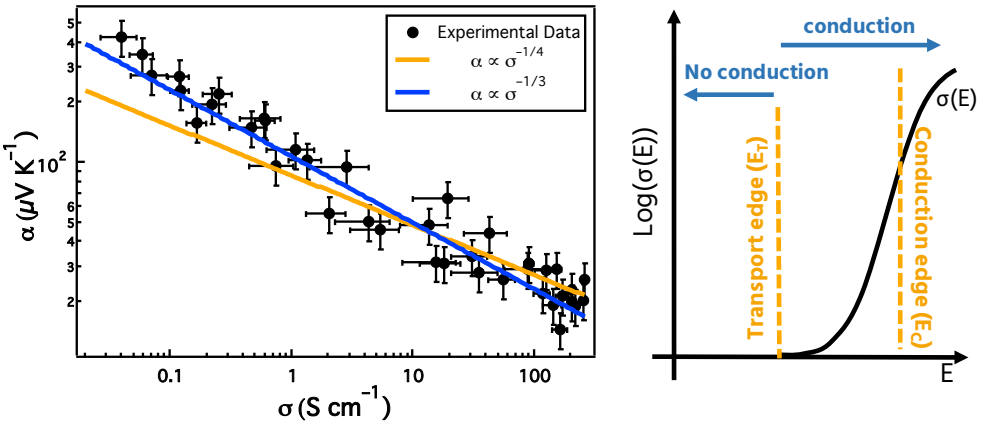

Figure 4.3. (a) Double logarithm plot of thermopower with electrical conductivity. Two power law fits are presented, with power exponents of –1/3 (blue) and –1/4 (orange). Error in thermopower is the standard +/– 20% to account for errors in temperature measurement. For the $\alpha \propto \sigma^{-1/3}$ fit, σ_{E0} = 0.002 S/cm. (b) Schematic demonstrating the difference between the transport edge E_T and the more traditional conduction or "mobility" edge, E_C where extended state conduction occurs. In the Kang and Snyder model, conduction can occur below E_C but not below the transport edge.

The degree of control attained by varying gate bias also modulates the Fermi level over a large energy range. Using Equation 4.6 with s = 3, reduced chemical potential ($\eta = \frac{E_F - E_T}{k_b T}$) was calculated for each experimental value of α to track E_F with respect to the transport edge. In the limit of high thermopower, E_F lies below E_T (i.e., $\eta < 0$), while at low thermopower the Fermi level extends to more than 1 eV past E_T (**Figure C3**). In the semiconductor degenerate limit, Equation 4.3 reduces to Equation 4.7.

$$\alpha = \frac{k_B}{e}\frac{\pi^2}{3} s\eta^{-1} \qquad \text{Equation 4.7}$$

The degenerate approximation becomes valid when η = ~8 or when α = ~100 μV K^{-1} from **Figure C3**. As a result, the $\alpha \propto \sigma^{-1/3}$ relationship should only be valid for α < 100 μV K^{-1} but seems to reasonably fit the entire data range.

We can consider the physical significance of the parameters in light of our experimental system. Our data shows an energetic difference of 1 eV between E_F and the

transport edge at high carrier concentration. This value is relatively large; although the exact bandwidth of semiconducting polymers is unknown, DFT calculations of models of ideal infinite crystals gives a bandwidth along the backbone and π-stacking direction around 0.67 and ~ 1 eV for pBTTT, respectively.[35,36] These models do not account for any local distortions from oxidation of the backbone, i.e., polaron formation. Additionally, the assumption of a static transport model is unlikely, particularly in the limit of high carrier concentration where ions infiltrate into the semiconductor. Therefore, it is imperative to consider a nonstatic density-of-states to understand the origin of seemingly large values of η at the highly doped limit.

The Kang and Snyder model provides a direct connection between thermopower and Fermi level relative to E_T using the transport function. To better connect these results with experimental values, one must understand how gating affects the density-of-states. This has been notoriously difficult in organic semiconductors due to disorder and nonuniform microstructure.[37] One of the most common formalisms was developed by Mott and Davis where σ(E) is calculated for a conduction or "mobility" edge, E_C, given by Equation 4.8 where μ(E) is defined as *microscopic* mobility, the carrier mobility for a given energy level.[7]

$$\sigma(E) = \begin{cases} \mu(E)eN(E)k_BT\,, & E > E_C \\ 0\,, & E \leq E_C \end{cases} \qquad \text{Equation 4.8}$$

The microscopic mobility is not equivalent to the macroscopic mobility measured experimentally because an experimental value is averaged over all accessible energies.

Although utilized in literature for disordered materials such as amorphous silicon, Equation 4.8 holds true only for a specific functional form of the conductivity function. From the Kubo-Greenwood formalism, Cohen *et al.* derive a more general relationship.[38] From the

definition of electrical conductivity, Cohen *et al.* find Equation 4.9 assuming independent carriers which is a more general form than Equation 4.8.

$$\frac{d\sigma(E)}{dE} = e\mu(E)N(E) \qquad \text{Equation 4.9}$$

A more detailed derivation may be found in the Supporting Information. From the goodness-of-fit for s = 3 in **Figure 4.3**, it is evident that $\sigma \propto E^3$ (Equation 4.2). The right side of Equation 4.9 must therefore scale with energy to the power of (s – 1) = 2. Although density-of-states and microscopic mobility are not completely disentangled in Equation 4.6, it allows us to examine cases between these parameters to make reasonable predictions for carrier transport. While they do not consider hopping explicitly, their formalism can still be used with the assumptions here.

The carrier concentration can be used to verify that the parameters used in the fits of the transport data are reasonable. Carrier density is related to the density-of-states through the Fermi–Dirac function, shown in Equation 4.10.

$$p = \int N(E)\big(1 - f(E, E_F)\big)dE \qquad \text{Equation 4.10}$$

We can first model the DOS assuming it is constant with doping via $N(E) = N_0 \times (E - E_T)^m$, where *m* dictates the DOS dependence on energy. This functional form for N(E) is not intuitive a priori but is a direct result of the fit in **Figure 4.3** and the transport function in Equation 4.5. Here, the prefactor, N_0, is chosen such that all models converge to the same point at 1 eV above the transport edge, above which the functional form of the conductivity function cannot be predicted (Appendix C). Assuming this form, it follows that $\mu(E) = \mu_0 \times (E - E_T)^{2-m}$ to be consistent with Equation 4.9. Three values of m were used to compare with experimental values: m = 1/2, m = 1, and m = 2. The former is similar to a free-electron gas model of the

DOS in inorganic semiconductors, and the latter tests the validity of an energy-independent mobility, i.e., a constant mobility for the states above E_T. The carrier density is simulated as a function of E_F using Equation 4.10 and compared to carrier density values attained experimentally.

Use of a static DOS fails to reproduce experimental carrier concentration with respect to the Fermi level (**Figure 4.4**). The successful fit of $\alpha \propto \sigma^{-1/3}$ combined with eqs 5 and 7 substantiates the use of a power-law DOS function assuming a constant mobility, but a constant DOS may oversimplify actual transport behavior. The assumption of constant mobility is plausible at energies above the conduction edge, but the functional form of μ(E) is less clear near the transport edge. The density-of-states and μ(E) could be changing in tandem, but we only consider the former since μ(E) cannot be measured experimentally.

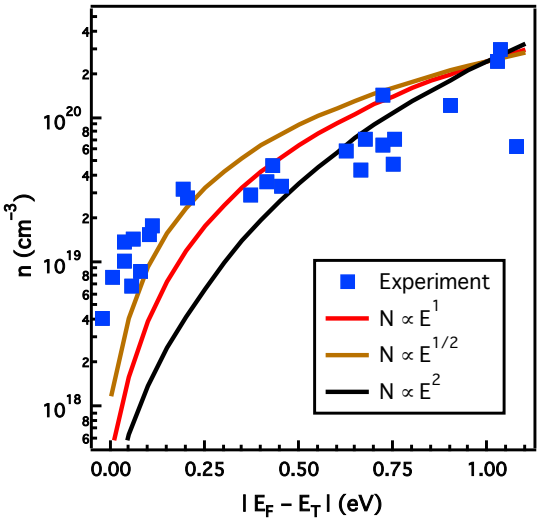

Figure 4.4. Carrier concentration measured experimentally (blue squares) compared to simulated carrier density for three power-law DOS models. The power-law form shown is is for a static DOS function.

A dynamic DOS shape in organic semiconductors has been considered in previous work through modeling a Gaussian density-of-states as well as an exponential form.[8,9,39] It is

possible, then, that (1) the energy dependence of the DOS is changing with E_F (i.e., m is changing along with the functional form of the mobility) or (2) the prefactor, N_0, is changing with E_F. Here, N0 gauges the slope of the density-of-states. Since thermopower is determined by carriers near the Fermi level, N_0 only reflects the local slope of the DOS around E_F.

Using Equation 4.10, we can calculate the value of N_0 necessary for each model to match carrier concentration measured at each energy assuming a constant mobility. **Figure 4.5a** shows that, for all models, N_0 decreases as E_F shifts farther from the transport edge. As N_0 decreases, the slope of the density-of-states at the Fermi level becomes shallower, indicating that the local DOS shape is broadening (**Figure 4.5b**). The most likely cause of this broadening is disorder induced by incorporation of the $TFSI^-$ counterions as the carrier concentration increases. Doping-induced energetic disorder in organic materials was first modeled by Arkhipov et al.[9] and theoretically connected to thermopower by Abdalla *et al.* using a modified Gaussian density-of-states that incorporates Coulombic interactions of ionic dopants.[40] Using this formalism, the α–σ power law trend was found to hold over a relatively wide range of conductivities substantiating the importance of incorporating energetic disorder into transport models for doped polymeric semiconductors.

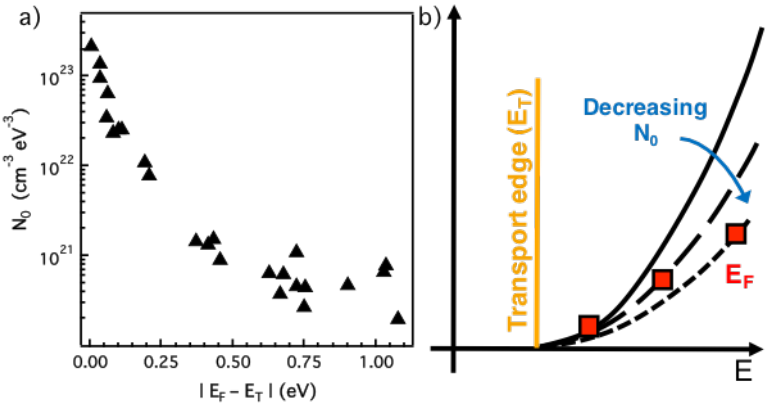

Figure 4.5. (a) Variation of the DOS pre-factor, N_0, with energy; representative data is shown for m = 2. (b) Schematic of evolution of DOS with increasing doping, where the Fermi level moves further past the transport edge as carrier concentration increases.

As previously mentioned, introducing small molecules to dope the semiconductor has been shown to perturb the physical structure at high dopant concentration,[2,41–43] which concomitantly changes the electronic landscape. Similar results have been shown using PPV[44] and more recently P3HT[45] through temperature-dependent measurements using a Gaussian form of the DOS. For a given temperature, a steeper DOS at the Fermi level leads to higher thermopower from Equation 4.2. As a result, increasing carrier concentration reduces thermopower not only from the reduction in entropy per carrier but also through decreasing the slope of *N(E)* through electronic disorder. A balance therefore exists in polymeric semiconductors to increase carrier concentration while minimizing perturbation in the density-of-states, which is affected by molecules infiltrating the material.

4.5 Conclusions

We have studied the thermoelectric properties of a semicrystalline polymer by using a PIL as the gate dielectric in a transistor architecture. A clear power law trend in thermopower and electrical conductivity is observed across four orders of magnitude in σ, revealed through controlling carrier density with gate bias. Modeling the data with a power-law density-of-states shows that a static function does not fit the experimental trend in carrier concentration with energy. In considering a power-law DOS function that varies with carrier concentration, we observe a decrease in the density-of-states prefactor, N_0, with increasing carrier density. This suggests that the local slope of the DOS decreases and energetic disorder increases as E_F moves past the transport edge.

The formalism used here implies that mobility may also be a function of energy for a given Fermi level. Understanding if and how the functional form of μ(E) would change with carrier concentration remains a subject for future studies. While we cannot directly probe μ(E), as experimentally measured mobility values are averaged over all energies, we expect that the microscopic mobility would become relatively independent of energy at high carrier concentration.

Changes observed in the semiconductor energetic landscape raise questions as to the effects of ion infiltration on the polymer microstructure.[46,47] Connecting microstructural changes with thermoelectric properties may offer more insight into a unifying model for charge transport in semiconducting polymers. Designing new semiconducting polymer–ion combinations to minimize structural changes could reduce perturbations in the DOS, leading to new limits in high-performance polymeric thermoelectrics.

4.6 Acknowledgements

The authors gratefully acknowledge support from the Department of Energy Office of Basic Energy Sciences under Grant No. DE-SC0016390. E.M.T. kindly acknowledges a National Science Foundation Graduate Research Fellowship under Award No. 1650114. Synthesis of the PIL was supported by the Air Force Office of Scientific Research through the Multidisciplinary University Research Initiative on Controlling Thermal and Electrical Transport in Organic and Hybrid Materials, Grant No. AFOSR FA95501210002, and measurements under shared facilities were supported through the MRSEC Program of the National Science Foundation under Award DMR-1720256.

4.7 Appendix C

4.7.1 Polymeric ionic liquid synthetic route

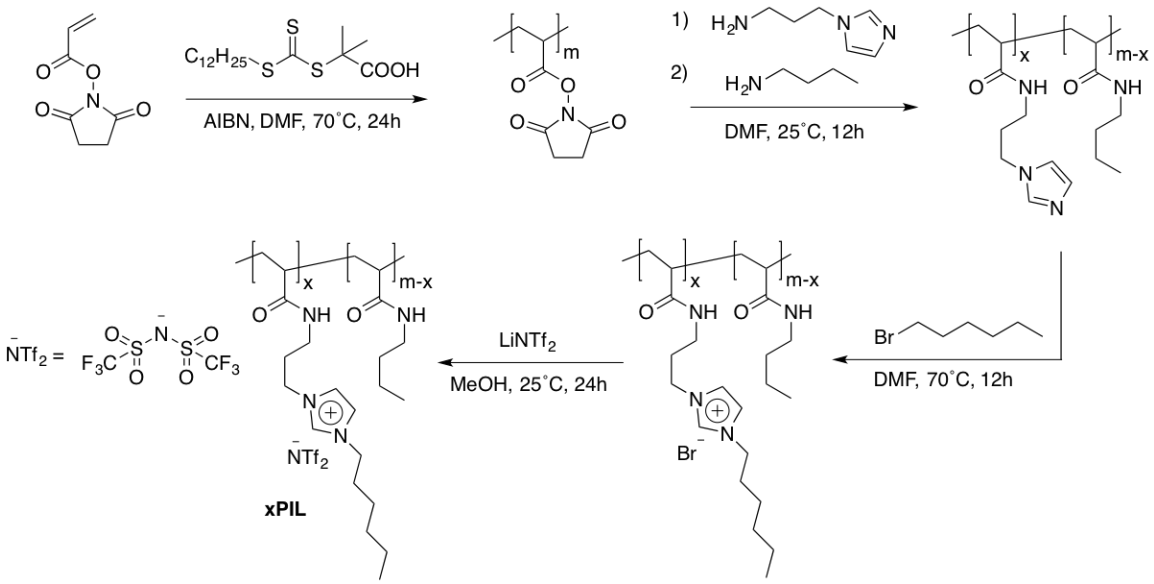

Scheme C1. Synthesis of 90PIL-TFSI. x = 0.9.

4.7.2 RAFT Poplymerization of N-hydroxysuccinimidyl acrylate (PNHSA)

N-acryloxysuccinimide (5.0 g, 29.6 mmol), DDMAT (17.9 mg, 0.05 mmol) and recrystallized AIBN (0.8 mg, 0.005 mmol) were dissolved in anhydrous DMF (30 mL) in a Schlenk flask. The solution was degassed using three freeze-pump-thaw cycles. After the third cycle the flask was filled with dry nitrogen and lowered in a pre-heated oil bath maintained at 70˚C for 24 h. The contents were stirred vigorously for this duration. After cooling to 25˚C, the polymer was precipitated from methanol, filtered and dried in ambient, dissolved in DMF and re-precipitated from methanol, twice. The polymer was filtered and dried under a vacuum at 60˚C for 24 h to yield a pale yellow powder (4 g). ^{1}H NMR (600 MHz, DMSO-d_6): δ 3.13 (1H, br), 2.80 (4H, br), 2.05 (2H, br). (M_n = 12.6 kg/mol, $Đ$ = 1.26, PS standards; M_n = 93.4 kg/mol from ^{1}H NMR end group analysis, D_p = 552).

PNHSA (3 g) was dissolved in anhydrous DMF (25 mL) at 25˚C. A solution of 1-(3-aminopropyl)imidazole (0.1 molar equivalent) in anhydrous DMF (1 mL) was added dropwise to the vigorously stirring polymer solution. The reaction temperature was maintained at 25˚C using a water bath for 12 h. The polymer was precipitated from ethyl acetate, dissolved in methanol and re-precipitated from diethyl ether, twice. The polymer was isolated by centrifugation and dried under a vacuum at 60˚C for 12 h to yield a pale yellow brittle solid. This was then dissolved in anhydrous DMF and the NHSA groups were exhaustively reacted with butylamine at 25˚C for 12 h to afford the neutral random copolymers. Quaternization of the imidazole pendant groups was subsequently achieved by reacting the polymers with 2 x molar excess of 1-bromohexane (with respect to imidazole) at 70˚C in anhydrous DMF for 12 h. The polymer was precipitated from diethyl ether and dried under a vacuum at 90˚C for 24 h. Finally, the PIL was obtained *via* anion metathesis by reacting the precursor random copolymers with 10 x molar excess of $LiNTf_2$ in methanol for 24 h. The polymer was precipitated from deionized water and further purified *via* dialysis using regenerated cellulose membranes (3000 MWCO) for 24 h in methanol/DI water, followed by 24 h in methanol. The solvent was evaporated *in vacuo* and the PIL was dried under a vacuum at 90˚C for 24 h and stored under nitrogen at all times.

4.7.3 Capacitance and thermopower measurement setup for PIL90-TFSI and gated transistors

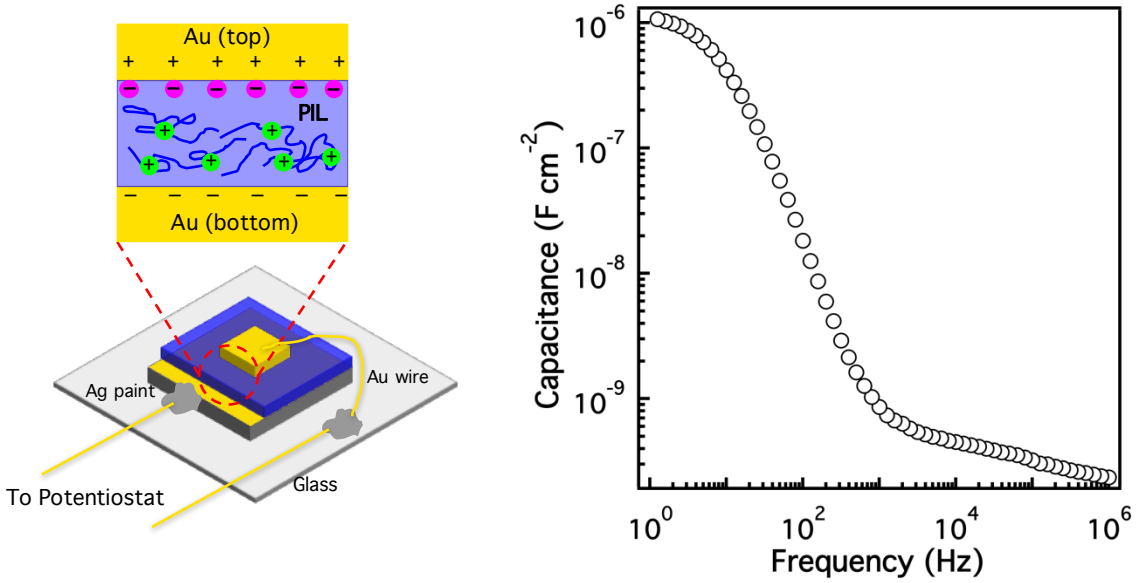

Figure C1. (a) Experimental setup for electrode polarization measurements. (b) Capacitance of PIL as a function of frequency. The PIL reaches a maximum of 1 μF/cm^2 at low frequencies.

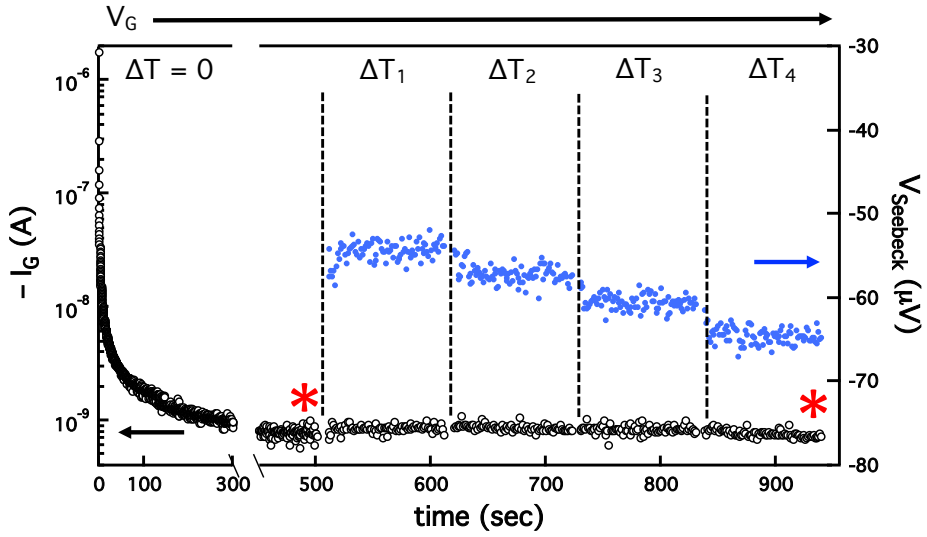

Figure C2. Representative thermopower operation for one gate voltage. Asterisks represent points at which conductivity measurements were taken.

4.7.4 Comparison of transport data to other models and reduced chemical potential η with thermopower

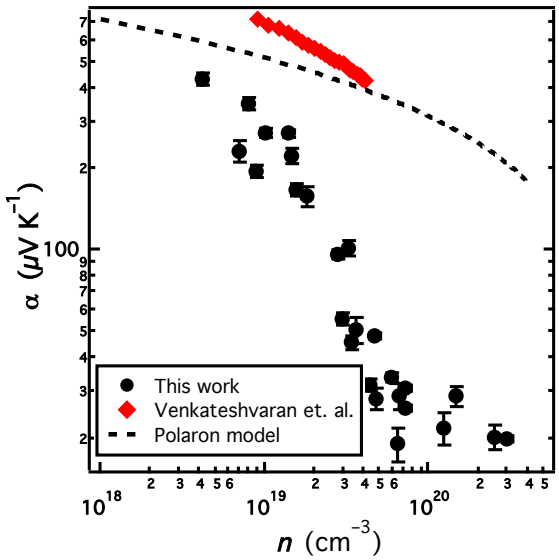

Figure C3. Thermopower comparison to the polaron model developed by Emin and coworkers compared to FET data with pBTTT. N = 2.0x10^{21} cm^{-3}, α_{vib} = 0.

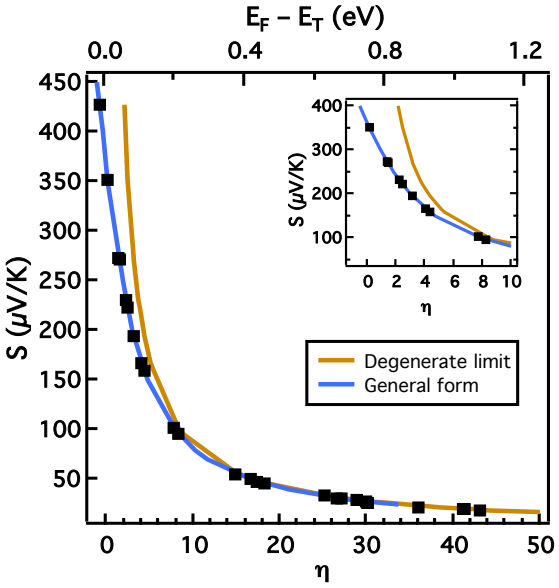

Figure C4. Calculated reduced chemical potential with thermopower. The degenerate assumption becomes most valid at η = ~8.

4.7.5 Derivation of Equation 4.9 in main text

Following the formalism from Cohen *et al.*,[38] the general definition of macroscopic electrical conductivity, assuming independent carriers, is

$$\sigma_M = \int \sigma(E) \left[-\frac{df}{dE} \right] dE \quad \text{(C1)}$$

where *f(E)* is the Fermi-Dirac distribution.

Integrating Equation C1 by parts leads to

$$\sigma_M = \int f(E) \left[-\frac{d\sigma(E)}{dE} \right] dE \quad \text{(C2)}$$

Another definition for macroscopic conductivity arises from semiconductor physics, where

$$\sigma_M = -\int e\mu(E)N(E)f(E)dE \quad \text{(C3)}$$

for any arbitrary function for *f(E)*, the integrands in Equations C2 and C3 can be equated:

$$\frac{d\sigma(E)}{dE} = e\mu(E)N(E) \quad \text{(C4)}$$

4.7.6 Full form of equations used for simulating carrier concentration fits

Three trial functions of the form $N(E) = N_0 \times (E_F - E_T)^m$ were used between carrier density-of-states and energy:

$$N(E) = 3.6 * 10^{20}(E_F - E_T)^{1/2} + 10^{19}$$

$$N(E) = 4.8 * 10^{20}(E_F - E_T)^{1} + 10^{19}$$

$$N(E) = 7.1 * 10^{20}(E_F - E_T)^{2} + 10^{19}$$

with an added constant of 10^{19} corresponding to the density of trap states when E_F lies at the transport edge.

4.8 References

(1) Jacobs, I. E.; Moule, A. J. Controlling Molecular Doping in Organic Semiconductors. *Adv. Mater.* 2017, *29*, 1703063, DOI: 10.1002/adma.201703063

(2) Patel, S. N.; Glaudell, A. M.; Kiefer, D.; Chabinyc, M. L. Increasing the Thermoelectric Power Factor of a Semiconducting Polymer by Doping from the Vapor Phase. *ACS Macro Lett.* 2016, *5*, 268– 272, DOI: 10.1021/acsmacrolett.5b00887

(3) Yim, K. H.; Whiting, G. L.; Murphy, C. E.; Halls, J. J. M.; Burroughes, J. H.; Friend, R. H.; Kim, J. S. Controlling electrical properties of conjugated polymers via a solution-

based p-type doping. *Adv. Mater.* 2008, *20*, 3319– 3324, DOI: 10.1002/adma.200800735

(4) Han, C. C.; Elsenbaumer, R. L. Protonic Acids - Generally Applicable Dopants for Conducting Polymers. *Synth. Met.* 1989, *30*, 123– 131, DOI: 10.1016/0379-6779(89)90648-6

(5) Patel, S. N.; Glaudell, A. M.; Peterson, K. A.; Thomas, E. M.; O'Hara, K. A.; Lim, E.; Chabinyc, M. L. Morphology controls the thermoelectric power factor of a doped semiconducting polymer. *Sci. Adv.* 2017, *3*, e1700434, DOI: 10.1126/sciadv.1700434

(6) Khodagholy, D.; Doublet, T.; Quilichini, P.; Gurfinkel, M.; Leleux, P.; Ghestem, A.; Ismailova, E.; Herve, T.; Sanaur, S.; Bernard, C.; Malliaras, G. G. In vivo recordings of brain activity using organic transistors. *Nat. Commun.* 2013, *4*, 1575, DOI: 10.1038/ncomms2573

(7) Mott, N. F.; Davis, E. A. *Electronic Processes in Non-Crystalline Materials*, 2 ed.; Oxford University Press: New York, 1979.

(8) Zuo, G. Z.; Li, Z. J.; Andersson, O.; Abdalla, H.; Wang, E. G.; Kemerink, M. Molecular Doping and Trap Filling in Organic Semiconductor Host-Guest Systems. *J. Phys. Chem. C* 2017, *121*, 7767– 7775, DOI: 10.1021/acs.jpcc.7b01758

(9) Arkhipov, V. I.; Heremans, P.; Emelianova, E. V.; Bassler, H. Effect of doping on the density-of-states distribution and carrier hopping in disordered organic semiconductors. *Phys. Rev. B: Condens. Matter Mater. Phys.* 2005, *71*, 045214, DOI: 10.1103/PhysRevB.71.045214

(10) Kurpiers, J.; Neher, D. Dispersive Non-Geminate Recombination in an Amorphous Polymer: Fullerene Blend. *Sci. Rep.* 2016, *6*, 26832, DOI: 10.1038/srep26832

(11) Kim, G.; Pipe, K. P. Thermoelectric model to characterize carrier transport in organic semiconductors. *Phys. Rev. B: Condens. Matter Mater. Phys.* 2012, *86*, 085208, DOI: 10.1103/PhysRevB.86.085208

(12) Zuo, G. Z.; Abdalla, H.; Kemerink, M. Impact of doping on the density of states and the mobility in organic semiconductors. *Phys. Rev. B: Condens. Matter Mater. Phys.* 2016, *93*, 235203, DOI: 10.1103/PhysRevB.93.235203

(13) Chen, J.; Heeger, A. J.; Wudl, F. Confined Soliton Pairs (Bipolarons) in Polythiophene - Insitu Magnetic-Resonance Measurements. *Solid State Commun.* 1986, *58*, 251– 257, DOI: 10.1016/0038-1098(86)90212-7

(14) Wang, S.; Ha, M.; Manno, M.; Daniel Frisbie, C.; Leighton, C. Hopping transport and the Hall effect near the insulator-metal transition in electrochemically gated poly(3-hexylthiophene) transistors. *Nat. Commun.* 2012, *3*, 1210, DOI: 10.1038/ncomms2213

(15) Sirringhaus, H. 25th Anniversary Article: Organic Field-Effect Transistors: The Path Beyond Amorphous Silicon. *Adv. Mater.* 2014, *26*, 1319– 1335, DOI: 10.1002/adma.201304346

(16) Venkateshvaran, D.; Nikolka, M.; Sadhanala, A.; Lemaur, V.; Zelazny, M.; Kepa, M.; Hurhangee, M.; Kronemeijer, A. J.; Pecunia, V.; Nasrallah, I.; Romanov, I.; Broch, K.; McCulloch, I.; Emin, D.; Olivier, Y.; Cornil, J.; Beljonne, D.; Sirringhaus, H. Approaching disorder-free transport in high-mobility conjugated polymers. *Nature* 2014, *515*, 384– 388, DOI: 10.1038/nature13854

(17) Khodagholy, D.; Rivnay, J.; Sessolo, M.; Gurfinkel, M.; Leleux, P.; Jimison, L. H.; Stavrinidou, E.; Herve, T.; Sanaur, S.; Owens, R. M.; Malliaras, G. G. High transconductance organic electrochemical transistors. *Nat. Commun.* 2013, *4*, 2133, DOI: 10.1038/ncomms3133

(18) Lee, K. H.; Kang, M. S.; Zhang, S. P.; Gu, Y. Y.; Lodge, T. P.; Frisbie, C. D. ″Cut and Stick″ Rubbery Ion Gels as High Capacitance Gate Dielectrics. *Adv. Mater.* 2012, *24*, 4457– 4462, DOI: 10.1002/adma.201200950

(19) Bubnova, O.; Berggren, M.; Crispin, X. Tuning the thermoelectric properties of conducting polymers in an electrochemical transistor. *J. Am. Chem. Soc.* 2012, *134*, 16456– 16459, DOI: 10.1021/ja305188r

(20) Zhang, F. J.; Zang, Y. P.; Huang, D. Z.; Di, C. A.; Gao, X.; Sirringhaus, H. N.; Zhu, D. B. Modulated Thermoelectric Properties of Organic Semiconductors Using Field-Effect Transistors. *Adv. Funct. Mater.* 2015, *25*, 3004– 3012, DOI: 10.1002/adfm.201404397

(21) Venkateshvaran, D.; Kronemeijer, A. J.; Moriarty, J.; Emin, D.; Sirringhaus, H. Field-effect modulated Seebeck coefficient measurements in an organic polymer using a microfabricated on-chip architecture. *APL Mater.* 2014, *2*, 032102, DOI: 10.1063/1.4867224

(22) McCulloch, I.; Heeney, M.; Bailey, C.; Genevicius, K.; MacDonald, I.; Shkunov, M.; Sparrowe, D.; Tierney, S.; Wagner, R.; Zhang, W. M.; Chabinyc, M. L.; Kline, R. J.; Mcgehee, M. D.; Toney, M. F. Liquid-crystalline semiconducting polymers with high charge-carrier mobility. *Nat. Mater.* 2006, *5*, 328– 333, DOI: 10.1038/nmat1612

(23) Lee, M. J.; Gupta, D.; Zhao, N.; Heeney, M.; McCulloch, I.; Sirringhaus, H. Anisotropy of Charge Transport in a Uniaxially Aligned and Chain-Extended, High-Mobility, Conjugated Polymer Semiconductor. *Adv. Funct. Mater.* 2011, *21*, 932– 940, DOI: 10.1002/adfm.201001781

(24) Lee, J.; Panzer, M. J.; He, Y. Y.; Lodge, T. P.; Frisbie, C. D. Ion gel gated polymer thin-film transistors. *J. Am. Chem. Soc.* 2007, *129*, 4532– 4533, DOI: 10.1021/ja070875e

(25) Said, E.; Crispin, X.; Herlogsson, L.; Elhag, S.; Robinson, N. D.; Berggren, M. Polymer field-effect transistor gated via a poly(styrenesulfonic acid) thin film. *Appl. Phys. Lett.* 2006, *89*, 143507, DOI: 10.1063/1.2358315

(26) Herlogsson, L.; Crispin, X.; Robinson, N. D.; Sandberg, M.; Hagel, O. J.; Gustafsson, G.; Berggren, M. Low-voltage polymer field-effect transistors gated via a proton conductor. *Adv. Mater.* 2007, *19*, 97– 101, DOI: 10.1002/adma.200600871

(27) Lee, J.; Kaake, L. G.; Cho, J. H.; Zhu, X. Y.; Lodge, T. P.; Frisbie, C. D. Ion Gel-Gated Polymer Thin-Film Transistors: Operating Mechanism and Characterization of Gate Dielectric Capacitance, Switching Speed, and Stability. *J. Phys. Chem. C* 2009, *113*, 8972– 8981, DOI: 10.1021/jp901426e

(28) Choi, J. H.; Xie, W.; Gu, Y. Y.; Frisbie, C. D.; Lodge, T. P. Single Ion Conducting, Polymerized Ionic Liquid Triblock Copolymer Films: High Capacitance Electrolyte Gates for n-type Transistors. *ACS Appl. Mater. Interfaces* 2015, *7*, 7294– 7302, DOI: 10.1021/acsami.5b00495

(29) Harada, T.; Ito, H.; Ando, Y.; Watanabe, S.; Tanaka, H.; Kuroda, S.-i. Signature of the insulator–metal transition of a semicrystalline conjugated polymer in ionic-liquid-gated transistors. *Appl. Phys. Express* 2015, *8*, 021601, DOI: 10.7567/APEX.8.021601
(30) Cochran, J. E.; Junk, M. J. N.; Glaudell, A. M.; Miller, P. L.; Cowart, J. S.; Toney, M. F.; Hawker, C. J.; Chmelka, B. F.; Chabinyc, M. L. Molecular Interactions and Ordering in Electrically Doped Polymers: Blends of PBTTT and F(4)TCNQ. *Macromolecules* 2014, *47*, 6836– 6846, DOI: 10.1021/ma501547h
(31) Egginger, M.; Irimia-Vladu, M.; Schwodiauer, R.; Tanda, A.; Frischauf, I.; Bauer, S.; Sariciftci, N. S. Mobile ionic impurities in poly(vinyl alcohol) gate dielectric: Possible source of the hysteresis in organic field-effect transistors. *Adv. Mater.* 2008, *20*, 1018– 1022, DOI: 10.1002/adma.200701479
(32) Glaudell, A. M.; Cochran, J. E.; Patel, S. N.; Chabinyc, M. L. Impact of the Doping Method on Conductivity and Thermopower in Semiconducting Polythiophenes. *Adv. Energy Mater.* 2015, *5*, 1401072, DOI: 10.1002/aenm.201401072
(33) Xuan, Y.; Liu, X.; Desbief, S.; Leclere, P.; Fahlman, M.; Lazzaroni, R.; Berggren, M.; Cornil, J.; Emin, D.; Crispin, X. Thermoelectric properties of conducting polymers: The case of poly(3-hexylthiophene). *Phys. Rev. B: Condens. Matter Mater. Phys.* 2010, *82*, 115454, DOI: 10.1103/PhysRevB.82.115454
(34) Kang, S. D.; Snyder, G. J. Charge-transport model for conducting polymers. *Nat. Mater.* 2017, *16*, 252– 257, DOI: 10.1038/nmat4784
(35) DeLongchamp, D. M.; Kline, R. J.; Lin, E. K.; Fischer, D. A.; Richter, L. J.; Lucas, L. A.; Heeney, M.; McCulloch, I.; Northrup, J. E. High carrier mobility polythiophene thin films: Structure determination by experiment and theory. *Adv. Mater.* 2007, *19*, 833– 837, DOI: 10.1002/adma.200602651
(36) Northrup, J. E. Atomic and electronic structure of polymer organic semiconductors: P3HT, PQT, and PBTTT. *Phys. Rev. B: Condens. Matter Mater. Phys.* 2007, *76*, 245202, DOI: 10.1103/PhysRevB.76.245202
(37) Noriega, R.; Rivnay, J.; Vandewal, K.; Koch, F. P. V.; Stingelin, N.; Smith, P.; Toney, M. F.; Salleo, A. A general relationship between disorder, aggregation and charge transport in conjugated polymers. *Nat. Mater.* 2013, *12*, 1038– 1044, DOI: 10.1038/nmat3722
(38) Cohen, M. H.; Economou, E. N.; Soukoulis, C. M. Microscopic Mobility. *Phys. Rev. B: Condens. Matter Mater. Phys.* 1984, *30*, 4493– 4550, DOI: 10.1103/PhysRevB.30.4493
(39) Rivnay, J.; Noriega, R.; Northrup, J. E.; Kline, R. J.; Toney, M. F.; Salleo, A. Structural origin of gap states in semicrystalline polymers and the implications for charge transport. *Phys. Rev. B: Condens. Matter Mater. Phys.* 2011, *83*, 121306R, DOI: 10.1103/PhysRevB.83.121306
(40) Abdalla, H.; Zuo, G. Z.; Kemerink, M. Range and energetics of charge hopping in organic semiconductors. *Phys. Rev. B: Condens. Matter Mater. Phys.* 2017, *96*, 241262R, DOI: 10.1103/PhysRevB.96.241202
(41) Chew, A. R.; Salleo, A. Spectroscopic studies of dopant-induced conformational changes in poly (3-hexylthiophene) thin films. *MRS Commun.* 2017, *7*, 728– 734, DOI: 10.1557/mrc.2017.88

(42) Tashiro, K.; Kobayashi, M.; Kawai, T.; Yoshino, K. Crystal structural change in poly(3-alkyl thiophene)s induced by iodine doping as studied by an organized combination of X-ray diffraction, infrared/Raman spectroscopy and computer simulation techniques. *Polymer* 1997, *38*, 2867– 2879, DOI: 10.1016/S0032-3861(96)00876-2

(43) Hynynen, J.; Kiefer, D.; Yu, L. Y.; Kroon, R.; Munir, R.; Amassian, A.; Kemerink, M.; Muller, C. Enhanced Electrical Conductivity of Molecularly p-Doped Poly(3-hexylthiophene) through Understanding the Correlation with Solid-State Order. *Macromolecules* 2017, *50*, 8140– 8148, DOI: 10.1021/acs.macromol.7b00968

(44) Hulea, I. N.; Brom, H. B.; Houtepen, A. J.; Vanmaekelbergh, D.; Kelly, J. J.; Meulenkamp, E. A. Wide energy-window view on the density of states and hole mobility in poly(p-phenylene vinylene). *Phys. Rev. Lett.* 2004, *93*, 166601, DOI: 10.1103/PhysRevLett.93.166601

(45) Pingel, P.; Neher, D. Comprehensive picture of p-type doping of P3HT with the molecular acceptor F(4)TCNQ. *Phys. Rev. B: Condens. Matter Mater. Phys.* 2013, *87*, 115209, DOI: 10.1103/PhysRevB.87.115209

(46) Giovannitti, A.; Sbircea, D. T.; Inal, S.; Nielsen, C. B.; Bandiello, E.; Hanifi, D. A.; Sessolo, M.; Malliaras, G. G.; McCulloch, I.; Rivnay, J. Controlling the mode of operation of organic transistors through side-chain engineering. *Proc. Natl. Acad. Sci. U. S. A.* 2016, *113*, 12017– 12022, DOI: 10.1073/pnas.1608780113

(47) Friedlein, J. T.; Rivnay, J.; Dunlap, D. H.; McCulloch, I.; Shaheen, S. E.; McLeod, R. R.; Malliaras, G. G. Influence of disorder on transfer characteristics of organic electrochemical transistors. *Appl. Phys. Lett.* 2017, *111*, 023301, DOI: 10.1063/1.4993776

(48) McCulloch, I.; Heeney, M.; Bailey, C.; Genevicius, K.; JacDonald, I.; Shkunov, M.; Sparrowe, D.; Tierney, S.; Wagner, R.; Zhang, W.; Chabinyc, M. L.; Kline, R. J.; McGehee, M. D.; Toney, M. F. Liquid-crystalline semiconducting polymers with high charge-carrier mobility. *Nat. Mater.* 2006, *5*, 328– 333

Chapter 5

Controlling ion/polaron interactions to modulate polaronic delocalization and temperature stability of doped polymeric semiconductors

The design of high-performance doped semiconductors requires an understanding of the coupling between ionic and electronic carriers. We utilize a method of counter-ion exchange using the polymeric semiconductor PBTTT-C_{14} to deconvolute the effects of ionic/polaronic interactions with the electrical properties of doped semiconducting polymers. Here, the dopant $NOPF_6$ is used following exchange of counter-ions ranging from 5.2 to 11 Å in diameter. The long-range order of the polymeric crystallites is not affected with this exchange process while effectively modifying the counter-ion distance to the charge carrier. Doped films achieve electrical conductivity of 320 S/cm and is not sensitive to an increased ion-polaron distance. We posit that other factors dominate the electrical properties at a device scale, such as the morphology and presence of domain boundaries. Interestingly, the temperature stability of the doped film can be drastically improved with the use of counter-ions containing less labile bonds. This platform serves as a unique way to retain the morphology of polymeric thin films while studying charge interactions at the local scale.

5.1 Introduction

The design of high-performance doped semiconductors requires an understanding of the coupling between ionic and electronic carriers. Doping is an essential way to increase the electrical conductivity in semiconducting polymers and can be accomplished through several routes. Molecular charge transfer dopants either accept electrons from the polymer (oxidation) or donate electrons to the polymer (reduction). In such cases, the neutralizing counter-ion to the charge carrier on the polymer is the (now charged) dopant molecule.[1] Protonating the polymer backbone with a Brønsted acid provides a similar effect with the proton donor acting as the counter-ion.[2,3] Electrochemical methods can be used to supply or remove electrons if the polymer is supported by a conductive substrate.[4]

Most doping methods require processing steps that limit the breadth of dopants used for semiconducting polymers. In the case of solution doping, the dopant and polymer must be miscible in the same solvent. This process becomes particularly challenging when the semiconductor becomes doped, as the solubility of charged polymers sometimes differs from that of its pristine state. Synthetic and processing strategies have partially addressed some of these difficulties.[5,6] For sequential and immersion doping, the dopant must be soluble in an orthogonal solvent in order for the dopant to infiltrate the film without the film dissolving.[5,7]

Utilizing temperature or pressure to introduce dopants from the gas phase into organic materials, defined as vapor doping, eliminates some convolutions of understanding charge coupling in polymers. Vapor doping has been used in a variety of settings, originating with iodine doping in polyacetylene[8] and extending to co-evaporation of organic molecules and dopants for OLEDs and OPVs.[9] However, this doping approach requires that the molecule sublimates without decomposing at temperatures and pressures that do not degrade the

polymeric film. These restrictions constrain the range of dopants commonly used with these methods. Choices for *p*-type vapor dopants include 2,3,5,6-Tetrafluoro-7,7,8,8-tetracyanoquinodimethane (F4TCNQ),[10–12] iron trichloride (FeCl3),[13,14] and bis(trifluoromethanesulfonyl)imide (HTFSI).[3,15]

For all doping mechanisms, the governing rules that exist between a conjugated polymer and dopant are difficult to ascertain. Our lack of understanding stems from a multitude of complications that arise from doping polymers. The thin-film morphology can evolve upon infiltration of dopants, which convolutes the effects of morphology and carrier concentration on the resulting electrical properties.[16] The use of different dopants changes the energetics of charge transfer, leading to a varying driving force for oxidation (or reduction) and the potential for complexation to occur.[17,18] These confounding factors make simple relationships, like how the degree of interaction between the dopant counter-ion and charge carrier impacts the electronic mobility, challenging to rationalize. An ideal system to study these relationships, therefore, requires a single dopant and polymeric morphology but a variable counter-ion diffusivity.

Current research efforts exist to understand the importance of counter-ion/polaron interactions in doped semiconductors through theoretical predictions and experimental methods. Spectroscopy is a powerful technique to analyze how polaronic charges in semiconducting polymers are affected by electronic coupling between chains, Coulombic interactions, and disorder.[19,20] One model developed to simulate these transitions in poly(3-hexylthiophene) uses a Holstein molecular crystal Hamiltonian modified to incorporate disorder that reflects the disorder present in polymeric crystallites.[21] The results of the simulations were found to match quantitatively with experimental results by charge-

modulation spectroscopy.[21] A central conclusion to the results is the importance of disorder within the interchain and intrachain axes of the aggregates.

Recently, this formalism was expanded upon for doped polymeric semiconductors by incorporating a point charge in proximity of the theoretical π-stack of polymer chains.[22,23] One notable feature from these simulations is an apparent shift in the position and intensity of the infrared absorption spectrum of the polaron as a function of distance between the counter-ion and polaron on the backbone. These spectral changes have been observed through strategies that manipulate either the dopant of choice or film processing method. It was found that through changing the crystallinity of the host polymer, more crystalline regions would force dopant counter-ions to exist further away from the polarons formed on the polymeric backbones.[24] A recent dodecaborane-based dopant was also synthesized to explore the limits of counter-ion/polaron distances and its impact on the electronic properties in P3HT.[25] Spectroscopic measurements revealed that the distance between the counter-ion and polaron in P3HT doped with the dodecaborane dopant approached infinity while significantly perturbing the crystalline order of the film.

Recently, work to facilitate charge transfer between the common dopant, F4TCNQ, and PBTTT was achieved in the presence of an ionic liquid.[26] It was found that F4TCNQ dissolved in EMIM-TFSI increased the doping efficiency of F4TCNQ with PBTTT while simultaneously trading the counter-ion in the film to TFSI–. This exchange led to a higher electrical conductivity and increased carrier concentration than when the ionic liquid was not present. The authors attribute the success of this phenomenon to a lower free energy of the doped film depending on the ionic liquid used, although it was unclear how the morphological evolution of the film played a role in its electronic properties.

Herein, we utilize a modified method of counter-ion exchange to deconvolute the effects of ionic/polaronic interactions with the electrical properties of doped semiconducting polymers. Introducing the counter-ion of interest interfacially after the initial doping step effectively exchanges the counter-ion within the film. The long-range order of the polymeric crystallites is not affected with this exchange process. Using a larger dopant counter-ion modifies the counter-ion distance to the charge carrier, in agreement with a theoretical model postulated for doped polymers. Notably, the electrical conductivity is not sensitive to an increased ion-polaron distance, despite the fact that the polaron should be more delocalized. We posit that other factors dominate the electrical properties at a device scale, such as the morphology and presence of domain boundaries. Interestingly, the temperature stability of the doped film can be drastically improved with the use of counter-ions containing less labile bonds.

5.2 Experimental Section

Materials. PBTTT-C_{14} was synthesized using a literature protocol.[32] $NOPF_6$ was purchased from ACROS Organics. All solvents were anhydrous and purchased from Sigma-Aldrich. All ionic liquids with the exception of EMIM-BArF were used as purchased without further purification.

EMIM-BArF Synthesis. EMIM-BArF was synthesized using a modified literature protocol.[40] Equimolar parts of [EMIM]Cl and Na[BArF] were suspended in acetone and stirred in a glovebox for 14 hours. The suspension was filtered through Celite® and the volatiles were removed, leaving an off-white crystalline solid. This was redissolved in dichloromethane and

filtered through a short plug of silica. The final material was dried under vacuum and stored in the glovebox.

Ion size measurements. All computations were performed using Gaussian 16. Anion geometries were optimized in vacuum using restricted DFT at the B3LYP/6-31G++(d,p) level. Anion volumes were taken as the average of ten tight volume calculations.

Thin Film Preparation. Thin films were prepared on silicon substrates (native oxide, University Wafer) for X-ray scattering, and z-cut quartz substrates (University Wafer) for conductivity, UV-Vis, and XPS measurements. Substrates were sonicated for 10 minutes sequentially in DI water and an IPA/acetone mixture, followed by exposure to UV-ozone (Jelight, Model 18) for 5 minutes. Gold contacts (20 nm) were thermally evaporated on the quartz substrates using a shadow mask. A solution of neat PBTTT-C_{14} (5 mg/ml, chlorobenzene) was spun cast hot (100 °C) at 1500 rpm to afford 25-nm thick films. Films were annealed at 180 °C for 10 minutes in a nitrogen-filled glovebox.

Vapor Doping. Vapor doping was performed using a sealed vessel, described in a previous publication.[11] In short, pristine films are attached to the lid of a jar that contains crystals of solid dopant. The jar is closed and heated for a set of exposure times on a hot plate. The $NOPF_6$-doping vessel was heated at 80 °C. Exposures were done incrementally in order to capture several doping levels of the films.

Ion exchange. $NOPF_6$-doped films are subjected to a droplet of ionic liquid (3M, acetonitrile) with a volume large enough to cover the substrate. Exchange proceeds for five minutes before the droplet is removed. Films are briefly immersed in acetonitrile to remove any excess salt remaining on the film surface.

X-*ray Photoelectron Spectroscopy (XPS)*. Measurements were performed with an Escalab Xi+ Spectrometer (ThermoFisher Scientific) using a monochromatic aluminum Kα X-ray source under a vacuum of 10^{-8} Torr. Charge compensation was carried out by injection of low-energy electrons into the magnetic lens of the electron spectrometer. High-resolution spectra were recorded at 20 eV pass energy at intervals of 0.05 eV. Survey spectra were recorded at 100 eV pass energy at intervals of 1 eV. Depth profiling was completed with an Ar^+ cluster gun with a cluster size of 1000 atoms.

UV-visible spectroscopy. UV-visible measurements were taken using an Agilent Cary 60 UV-Vis Spectrophotometer. Spectra were taken on 0.5 mm-thick quartz substrates.

FTIR spectroscopy. FTIR spectroscopy was performed in a nitrogen atmosphere using a Nicolet Magna 850 FTIR Spectrometer with an InSb detector. Samples were spincast on KBr salt plates (13 x 2 mm, PIKE Technologies) using the same conditions as for other characterization techniques.

X-ray Characterization. X-ray scattering was conducted on beamline 7.3.3 at the Advanced Light Source (ALS).[41] Silver behenate was used as a calibration for the beam center and sample-todetector distance. 2D GIWAXS scattering images were collected using a Pilatus 2M area detector at an incidence angle of 0.12° with 5–60 s exposure times. The samples were kept under a helium environment during X-ray exposure to minimize sample degradation and scattering from O_2. The collected data were processed using Nika, a 2D data reduction macro on Igor Pro using established procedures. To correct for the grazing incidence geometry, scattering intensity was integrated along a small sector near the missing wedge to obtain 1D profiles near $q_z = 0$.

Electrical Characterization. All electrical measurements were performed under a nitrogen environment inside a glovebox. Electrical conductivity was measured using a Keithley 6485 picoammeter. Measurements were taken in the in-plane direction using the TLM method to eliminate contact resistance for samples with low conductivity.

5.3 Results and Discussion

5.3.1 $NOPF_6$ is an effective vapor dopant

Introducing dopants from the vapor phase into films of semiconducting polymers can occur without modification of the long-range order of the polymeric crystallites. Since the fastest route of hole conduction is along the polymeric backbone, preserving the long-range crystalline order of the polymer upon doping is beneficial for high carrier mobility.[16,27] Introduction of dopants from a solvent using a sequential casting process leads to minimal perturbation of the crystallites if the solvent does not excessively swell the amorphous and crystalline domains.[5] Previous work has shown that doping in the vapor phase also minimizes evolution of the polymeric crystallites on the length scale of ~50 – 200 nm.[11,12] Both sequentially doped and vapor doped films exhibit superior electronic conductivity to solution doped films, where the crystalline order within the film is partially destroyed.[28] It is critical in this work to induce minimal changes in long-range order for straightforward conclusions to be made about polaron/counter-ion interactions and charge transport.

Unlike many charge transfer dopants, chemical dopants like $NOPF_6$ undergo an irreversible change, which ensures that PF_6 species exist as anions within the film. Previously used as an oxidant for immersion doping,[29,30] nitrosonium hexafluorophosphate ($NOPF_6$) is a salt that undergoes a chemical change when reduced. After oxidizing the polymeric backbone,

nitric oxide (NO) is evolved and leaves PF_6^- as the counter-ion to the polaron formed on the backbone. Although previous work has focused on immersion doping, these metal fluoride complexes can sublimate before decomposition upon heating. $NOPF_6$ sublimes as an ion pair below 100 °C and can infiltrate a polymer film as one compound rather than separate ions.[31] Here, we use a sublimation temperature of 80 °C at nearly atmospheric pressure, which corresponds to a vapor pressure of $NOPF_6$ of approximately 5×10^{-5} atmospheres, or 0.04 torr.[31]

Counter-ion exchange is an effective way to maintain the doping level in semiconducting polymers with the freedom to explore size effects of counter-ions on charge transport. The mechanism of counter-ion exchange operates through establishing a large concentration gradient of both anions in order for the exchange to proceed to completion. Briefly, a vapor-doped film is exposed to a 3M salt solution in acetonitrile containing the anion of interest for five minutes (**Figure 5.1a**). The solution is removed, and the film is washed in acetonitrile to remove any excess salt. Poly[2,5-bis(3-tetradecylthiophen-2-yl)thieno[3,2-b]thiophene] (PBTTT) was employed as the semiconducting polymer (**Figure 5.1b**) due to its semi-crystalline nature and high charge carrier mobility of ~1 V cm^{-2} s^{-1}.[32] In this work, the cation within the salt solution remained constant as 1-ethyl-3-methyl imidazolium ($EMIM^+$). We find that ionic liquid does not infiltrate PBTTT in the neat state, indicating that the driving force for exchange arises from the presence of the dopant counter-ion within the film (Appendix D, **Figure D1**). Five anions were utilized with ionic diameters ranging from 5.2 Å (BF_4^-) to 8.2 Å (PCF^-), whose chemical structures are shown in **Figure 5.1c**.

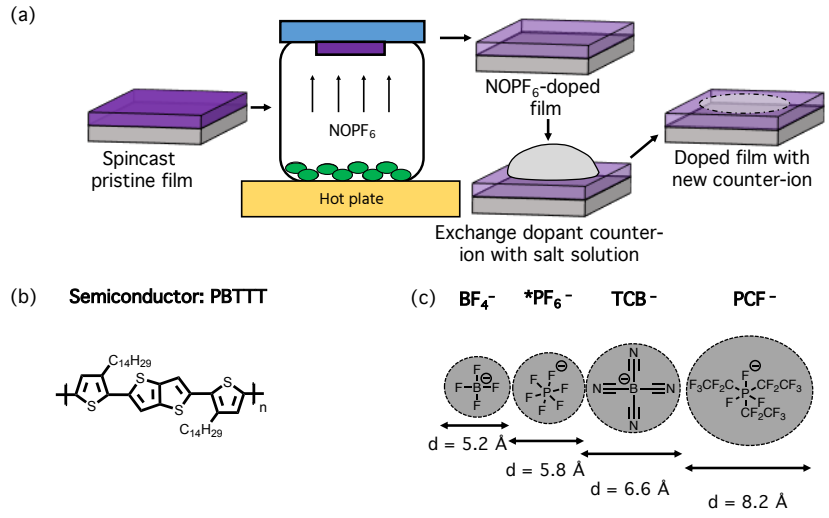

Figure 5.1. (a) Schematic of the counter-ion exchange process. (b) Chemical structures for the polymeric semiconductor and (c) dopant counter-ions used in this work. PF_6^- acts as the original dopant counter-ion from vapor doping.

Depth profiling by ion beam etching with X-ray photoelectron spectroscopy (XPS) to determine composition provided direct evidence of the degree of exchange between dopant and salt counter-ion. To ensure that counter-ion exchange takes place throughout the entirety of the film, an argon cluster gun was used to etch the sample while obtaining XPS spectra as a function of film depth. The clusters of argon atoms ablate the film with a sufficiently low energy as to not disrupt the chemical bonding environment of the analyzed layers.[33,34] The silicon Si_{2p} signal delineates the transition between the polymer film and the quartz substrate.

Depth-profiled XPS spectra of doped and counter-ion exchanged films of PBTTT confirm that PF_6^- anions are successfully replaced through the exchange process. In the PBTTT films doped with $NOPF_6$, a clear signature from the phosphorus P_{2p} peak is present in the XPS spectrum (**Figure 5.2a**). Upon counter-ion exchange with [EMIM][BF_4] and [EMIM][TCB], no detectable phosphorous is present at the surface, indicated by the corresponding traces in **Figure 5.2a**. The doped film exchanged with [EMIM][PCF] also

exhibits a phosphorous peak from the PCF^- anion, but we note that the signal is downshifted by ~ 1.6 eV in binding energy. This shift indicates that the positive charge is more delocalized from the central phosphorous atom for PCF^- than with PF_6^-, which is expected for a larger anion. Atomic concentration is reported as a comparison of the P_{2p} signal to the sulfur S_{2s} signal (from the polymer) and the Si_{2p} signal. **Figure 5.2b** indicates that there exists approximately one phosphorous atom for every nine sulfur atoms throughout the film, which translates to 2 dopants for every 5 monomers for PBTTT, which is consistent with the UV-Vis spectra of the doped film (**Figure 5.3a**). The fraction is similar for PCF^-, indicating that the doping level is comparable between the doped and exchanged film. The phosphorous atomic concentration for other exchanged films remains negligible with etching time, confirming that all PF_6^- counter-ions are removed.

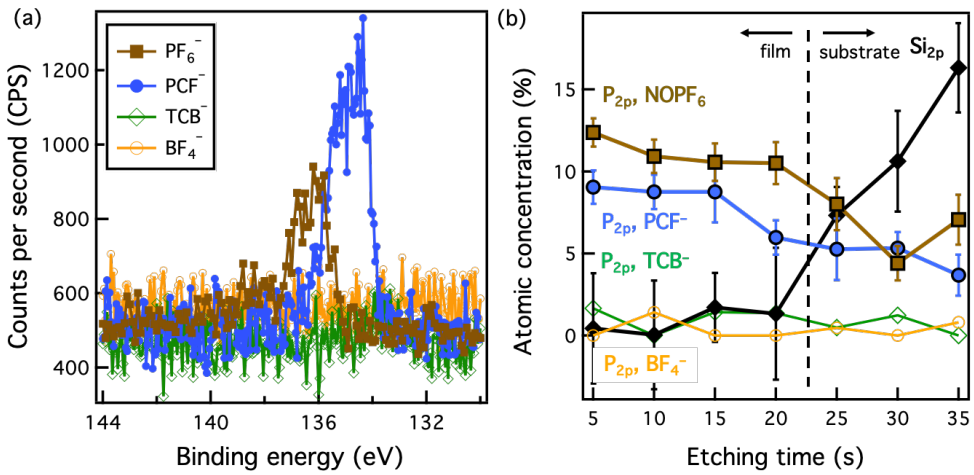

Figure 5.2. XPS depth profile scans of doped and exchanged films. Tracking the atomic concentration of the P_{2p} signal provides direct evidence for the success of ion exchange through the depth of the film. (a) The $NOPF_6$-doped and PCF^--exchanged films of PBTTT exhibit clear signatures from phosphorous, as evidenced by the P_{2p} region of the XPS spectrum. Films exchanged with TCB^- and BF_4^- show no phosphorous signal. (b) Comparing the atomic concentration of phosphorous to the sulfur signature in depth-profiled spectra indicate that exchange is successful throughout the depth of the film. The Si_{2p} signal is used as a marker to differentiate between the film and the substrate which is differentiated by scans with greater than 5% silicon by atomic concentration.

While the phosphorous signal is completely absent throughout the depth of the film upon exchange with [EMIM][BF_4], the fluorine signature is dramatically decreased as well (Appendix D), indicating an inhomogeneous profile of this counter-ion. We postulate that rather than counter-ion exchange, the film is de-doping upon exposure to the BF_4–based salt solution. Since BF_4^- has been used successfully for electrochemical transistors in aqueous conditions,[35] partial de-doping suggests that BF_4^- is not an ideal counter-ion for this strategy, potentially due side reactions with the dopant counter-ion. For all other ions investigated, signatures of ion-specific elements indicate that exchange was effective throughout the depth of the film (Appendix D, **Figure D2**). The direct evidence of full conversion through counter-ion exchange gives confidence that any changes in the electronic and morphological properties are due to the presence of a different counter-ion.

5.3.2 Infrared spectroscopy indicates a more delocalized polaron with larger counter-ions

The ability to exchange the counter-ion while maintaining doping level allows us to corroborate the evolution of the absorption spectra of doped films as a function of counter-ion/charge carrier distance. Two primary absorption features of hole polarons in conjugated polymers exist in the infrared. The transition that occurs between 0.3 and 0.6 eV is attributed to the transition of the polaronic wavefunction to the first excited electronic state (known as peak B or P1). All higher energy transitions have negligible oscillator strengths. A lower energy feature, known as peak A or DP1, is observed on the order of the aromatic/quinoidal stretching mode of thiophene that arises from Herzberg-Teller coupling.[21] Theoretical simulations of the infrared absorption spectrum of doped P3HT indicates that the shift in peak B and the ratio of intensity of peak A to peak B directly correlates to an increase in coherence

length of the polaron within the aggregate. Although many factors influence the absolute average distance between charges and countercharges, infrared spectroscopy provides a valuable way to compare between doped samples, and in this case, counter-ion exchanged samples. Since our system contains a similar host polymer as theoretical calculations performed previously, we expect any variance in the spectra to exist due to the different counter-ion present in the film.

The optical absorbance spectra in the mid-IR (400 – 5000 cm^{-1}) captures a monotonic shift of peak B to lower wavenumbers with increasing counter-ion size, indicating that utilizing a larger counter-ion increases the average ion-polaron distance. The infrared spectra of counter-ion exchanged films all contain clear signatures of peaks A and B, corresponding to the presence of polarons within the films (**Figure 5.3b**). Sharper features observed at < 1000 cm^{-1} correspond to molecule-specific IR-active vibrational modes (IRAVs). There is one additional sharp peak centered around ~ 2920 cm^{-1}, which we expect arises from aliphatic C–H bonds within the film. We also note that ring stretching modes of imidazolium are not observed within the spectrum, which typically occur between 3000 cm^{-1} and 3200 cm^{-1}.[36] Additionally, we observe no features of imidazolium in a pristine film of PBTTT exposed to ionic liquid (Appendix D **Figure D1**). For these reasons, we believe that the cation of the salt solution does not penetrate into the film. With increasing counter-ion diameter, the peak of B shifts monotonically from approximately 0.5 eV (4030 cm^{-1}) to 0.34 eV (2742 cm^{-1}), which indicates a higher polaron coherence length with larger counter-ions. Additionally, the A:B intensity ratio increases from 0.25 for PF_6^- to 0.9 for PCF^- (inset in **Figure 5.3b**), consistent with a greater degree of Herzberg-Teller coupling with more delocalized polarons. It is

apparent that the A:B intensity ratio for BF_4^- is even smaller, but the intense IRAVs at low energy obscures the signal.

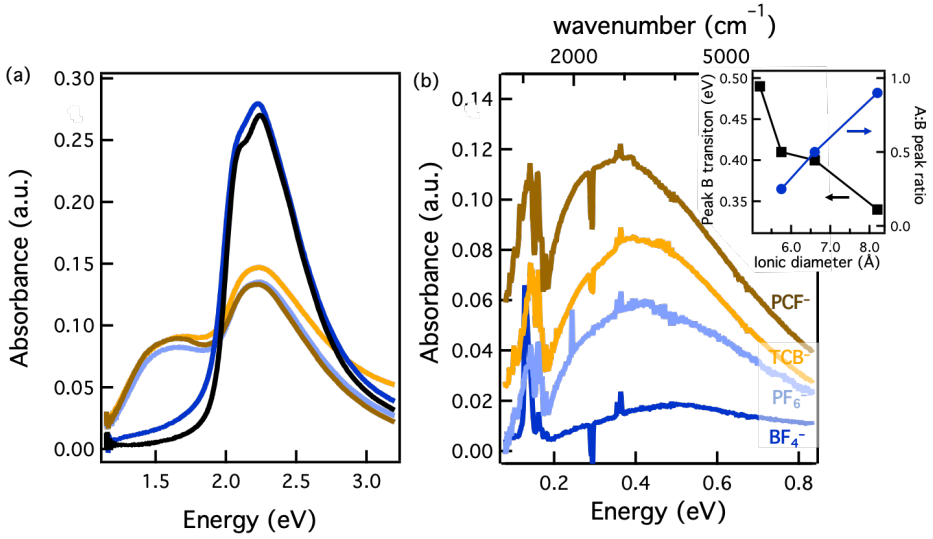

Figure 5.3. (a) UV-vis spectroscopy indicates that a similar doping level is achieved with the exchanged films, with the exception of [EMIM][BF_4], which mostly reverts to the pristine spectra of PBTTT (black trace). (b) FTIR spectra of doped and exchanged films. The energy of peak B decreases and the A:B peak ratio increases with increasing ionic diameter (inset), indicating an increase in polaronic coherence length with more diffuse counter-ions.

5.3.3 Counter-ion exchange exerts minimal change to long-range and crystalline order in doped films

An important parameter in understanding the fundamental dopant counter-ion/hole polaron interactions in polymers is the contribution of morphology. The crystallinity and long-range order govern the ultimate electrical properties and mechanism of charge transport, as seen in both experimental and theoretical work. The process of introducing dopant molecules has been shown to change the morphology of semi-crystalline polymers depending on the nature of the dopant and the way in which it is introduced. These competing effects contribute to the difficulty of realizing the true impact of the interactions between ions and polarons on the polymeric backbone; for this reason, it is desired to influence morphology as little as possible

to more directly probe counter-ion effects on the optical and electronic properties of doped polymers. As doping and use of solvent can impact both the short-range and long-range order of crystallites, it is critical to use complementary methods to ascertain a full picture of the morphological changes induced by doping and counter-ion exchange.

The process of counter-ion exchange does not affect the long-range order of PBTTT crystallites, indicating that introduction of large counter-ions can maintain the crystalline order within doped semiconductors. One metric used to quantify the degree of long-range order within crystalline regions is the orientational correlation length (OCL), or the length scale over which the ordered regions drift out of alignment with one another, measured by resonant soft X-ray scattering (RSoXS). Using a polarized X-ray beam at the energy of the C_{1s} to π^* transition (~ 285.2 eV) allows the scattering to be dominated by the length scale of alignment of edge-on polymer chains. A pristine film of PBTTT exhibits a peak in the Lorentz-corrected scattering profile at q = ~0.002 $Å^{-1}$ (**Figure 5.4**). The OCL is defined as half the characteristic length scale from the primary scattering peak ($d^* = 2\pi/q^*$), leading to an observed OCL of approximately 150 nm. The OCL does not change when exposed to acetonitrile, which is consistent with previous work that showed that the molecular scale ordering did not change with acetonitrile exposure.[11] Upon vapor doping with $NOPF_6$ and counter-ion exchange, we find that the OCL varies very little within the range of counter-ion sizes used in this study. This invariance is likely due to the processing methods used in this work, as doping from solution was found to dramatically lower the OCL of PBTTT. As a result, we assert that effects of the dopant counter-ion on electronic properties are due to modulation of the counter-ion/polaron distance since the orientation of the backbones is largely maintained.

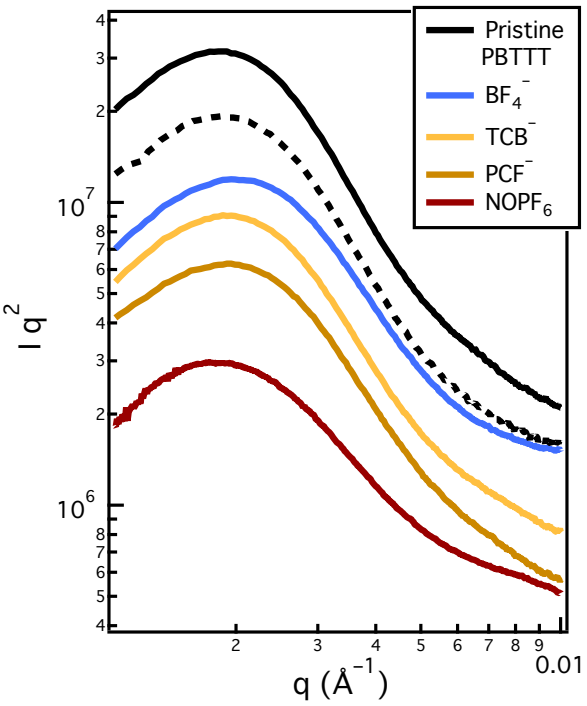

Figure 5.4. Lorentz-corrected, circularly averaged RSoXS scattering profiles of ion-exchanged films at a resonance energy of 285.2 eV. The OCL of the PBTTT crystallites is not impacted through the ion exchange process.

The molecular scale coherence of the PBTTT crystallites is also maintained through ion exchange, but individual crystallites expand to incorporate larger dopant anions. Grazing-incidence wide angle X-ray scattering (GIWAXS) yields two-dimensional information about the local order of polymeric crystallites. One-dimensional intensity line cuts in both the out-of-plane and in-plane directions of the scattering pattern provide a quantitative way to discern effects of doping and counter-ion exchange in both directions of the crystallite. Intensity line cuts in the out-of-plane (alkyl stacking) direction of the crystallites initially indicates that doping with $NOPF_6$ in the vapor phase and counter-ion exchange does not destroy the crystalline regions of PBTTT, as at least three higher-order peaks of the alkyl stacking is seen for all films (Appendix D).

Fitting the alkyl stacking and π–stacking peaks from GIWAXS show that the crystallites expand to incorporate larger dopant counter-ions, indicating that all counter-ions exist within the side chain region of the crystallites. The alkyl stacking distance of PBTTT crystallites increases up to 24Å (compared to 21.3 Å prior to doping) (**Figure 5.5**). Expansion in the alkyl stacking direction is coupled to a decrease in the π–stacking direction from 3.73 Å to approximately 3.6 Å. The change in π–stacking distance is less sensitive to ionic diameter, signifying that other variables are at play to determine the final dimensions of the unit cell in the crystalline domains. Recent theoretical work concludes that the charge along the backbone may contribute to structural changes in the π–spacing distance of polymeric crystallites.[37] Although molecules as large as PCBM-C_{84} (molecular diameter of approximately 1 nm) have been observed to intercalate into the side chains of PBTTT,[38] we expect that there exists a limit to the molecular size that can infiltrate the crystallites.

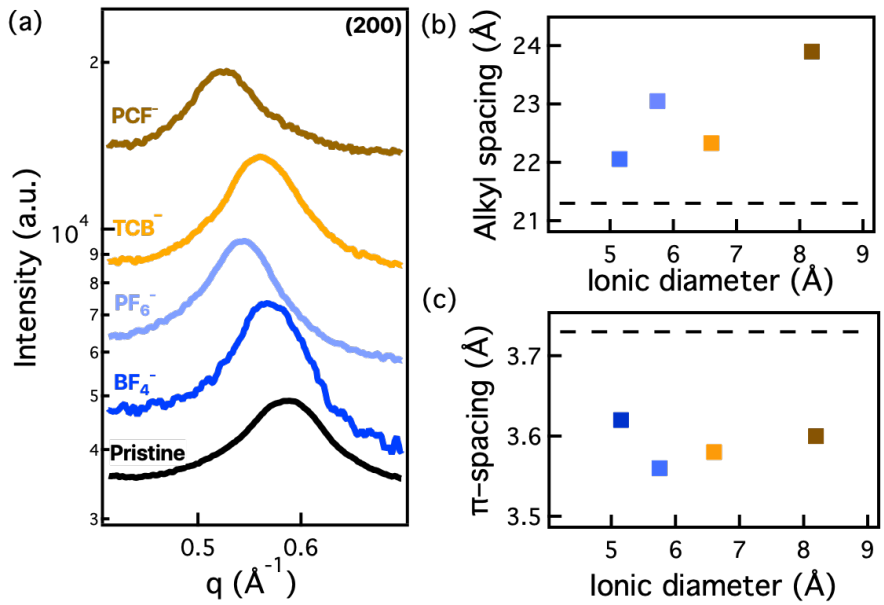

Figure 5.5. (a) GIWAXS line cuts near the missing wedge of doped and exchanged films. The molecular distance shows a monotonic increase in the alkyl spacing with ionic diameter (b), but a clear plateau in the π-spacing (c).

5.3.4 Counter-ion identity has little effect on electronic mobility but governs temperature stability

The electrical conductivity of doped films does not depend on the degree of delocalization between hole polaron and the charge-neutralizing counter-ion, indicating that other factors of the semiconductor dominate the macroscopic electronic properties. Films with counter-ions that are smaller than the PF_6^- ion exhibited a lower electrical conductivity, since there seemed to be a degree of dedoping from optical and XPS measurements in exchanging for a smaller counter-ion (**Figure 5.6**). It is possible here that these counter-ions react with either the polymer or the PF_6^- within the film to affect the doping level, as BF_3 is a common Lewis acid. However, XPS and UV-Vis indicate that the doping level of films remained consistent for larger dopant counter-ions, and the counter-ion/polaron distance is also larger from infrared spectroscopy. This result is unique from previous studies that correlated a more delocalized polaron to a higher electrical conductivity, either through varying the polymeric crystallinity or through use of a bulky dopant. However, these strategies also introduce morphological variations that convolute straightforward conclusions from being made about the direct effect of interactions between the counter-ion and polaron on the carrier mobility. For this work, delocalization effects at the molecular scale do not translate into higher electrical conductivity. Although the local mobility of carriers may be higher in films with large counter-ions, mesoscopic factors such as grain boundaries and long-range order are most likely to dominate the electrical properties at the device scale. Since we expect these factors to be invariant between films, the electronic mobility remains constant even for large counter-ions.

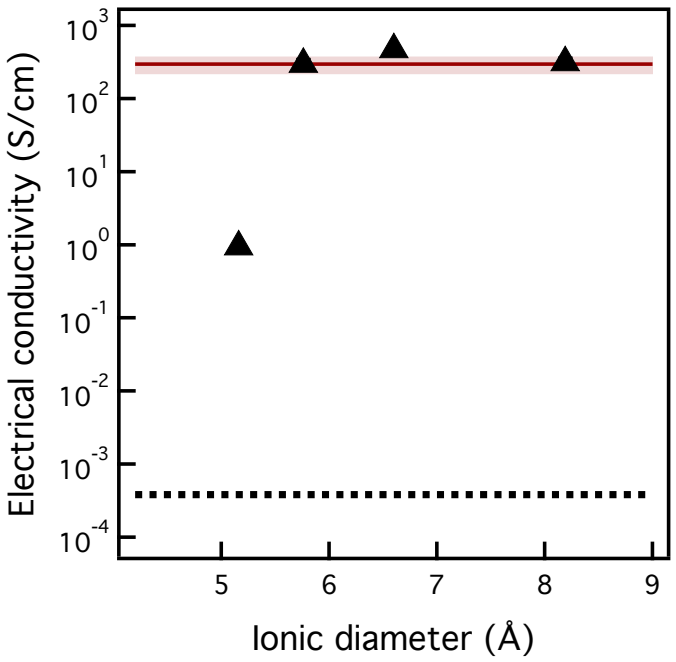

Figure 5.6. Electrical conductivity of doped and counter-ion exchanged films. Above a threshold ionic diameter, the electrical conductivity is insensitive to the polaron/ion distance. The shaded region for the doped $NOPF_6$ electrical conductivity corresponds to 1 standard deviation between triplicate samples. Error bars for other samples are smaller than the symbol size.

One crucial aspect that counter-ion exchange can explore within doped semiconductors is the thermal stability of doped films with different charge neutralizing ions. The thermal behavior of doped polymeric semiconductors has been difficult to study mainly due to dopants reacting or desorbing at relevant temperatures. For instance, F_4TCNQ, a prototypical dopant for *p*-type semiconductors, begins to desorb around 115-120 °C for systems with alkyl side chains; this temperature is below the pertinent thermal transitions of many semiconductors used today. Understanding how the thermal transitions of polymers evolve upon doping is important for high-temperature processing and formulating. Additionally, several applications for which doped polymeric semiconductors could be used require some degree of thermal stability, from thermoelectrics to integration into wearable devices. Thus, a need for a thermally stable polymer in its doped state has great technological relevance.

Counter-ion exchange leads to conductive films that are more thermally stable at elevated temperatures relative to the doped state before exchange, which indicates that this process could bring new insight for stably doped polymers at elevated temperatures. **Figure 5.7a** shows that temperatures as low as 80 °C provides sufficient thermal energy for PF_6^- to degrade in the film. While the degradation mechanism is not clear, the electronic charges are no longer supported by the dopant counter-ion, which leads to lower conductivity. The identity of the counter-ion dictates the thermal stability of the doped film, with PCF^- leading to the most stable films whose conductivity remains unchanged until ~140 °C. Conductive stability at these levels is surprising, as these temperatures approach the liquid crystalline transition of pristine PBTTT. We find that the stability correlates with the thermal decomposition temperature of the ion in the neat ionic liquid (**Figure 5.7b**), indicating that molecular bond lability is a more predictive factor of thermal stability of the doped film.[39] We believe the BF_4-exchanged films degrade at anomalously low temperatures due to side reactions in the film. These results indicate that it is the stability of the dopant, rather than the polymer, that dictates the ultimate thermal stability of doped films at high temperature.

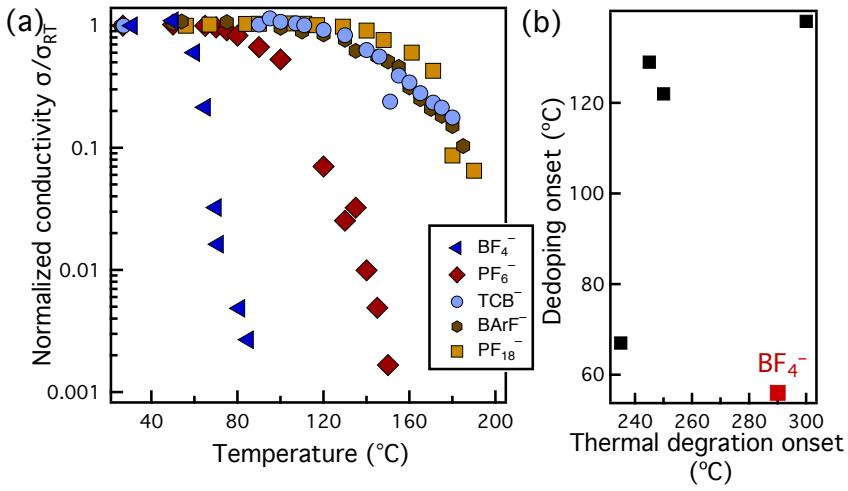

Figure 5.7. (a) Temperature stability of doped films. Rather than size, the bonding chemistry of the counter-ion plays a more important role in the temperature stability of doped films. (b) There exists a correlation between the onset of thermal degradation of the neat ionic liquid and the onset temperature of dedoping, indicating that counter-ion chemistry is crucial for high-temperature applications. The red symbol corresponds to BF_4-exchanged films, which likely dedope at anomalously low temperatures due to side reactions within the film.

5.4 Conclusions

Counter-ion exchange is a powerful approach to controllably investigate the effect of different dopant counter-ions on the stability of doped polymers. Vapor doping combined with counter-ion exchange post-processing effectively replaces the dopant counter-ion while maintaining doping level, while inducing minimal changes in the crystalline long-range order of PBTTT. While local counter-ion/polaron distances are influenced by ionic diameter, ultimately the morphology plays the dominant role in the electrical properties. However, we find that the counter-ion resistance to degradation plays the dominant role in the thermal stability of the doped film, with some counter-ions remaining stable up to 140 °C.

This exchange process allows us for the first time to investigate the thermal transitions of polymeric semiconductors in their charged state. Understanding the thermal behavior of polymers is critical to obtain meaningful conditions required for their processing and operation. However, the impact of charge carriers on the thermal behavior of polymers is unknown. This lack of knowledge arises from instability of most dopants at temperatures where pertinent phase transitions may occur. Future work will investigate these thermal transitions to ascertain how charge impacts the thermal properties of polymeric semiconductors.

Counter-ion exchange also provides a unique avenue to study charge transport at elevated temperatures, many of which are relevant to applications of doped polymeric

semiconductors. For example, semiconducting polymers show immense potential for use in thermoelectric generators. Few studies have investigated their utility at temperatures greater than 50 °C, although applications for low grade waste heat capture occurs at temperatures between 80 and 100 °C. Investigating the thermopower and thermoelectric power factor changes at relevant operation temperatures will provide valuable information about optimal conditions for high performance operation of polymer-based thermoelectrics and next-generation polymeric devices.

5.5 Acknowledgements

The authors acknowledge funding support from the Department of Energy Office of Basic Energy Sciences under grant no. DE-SC0016390. Infrared spectroscopy made use of shared facilities of the UCSB MRSEC (NSF DMR 1720256), a member of the Materials Research Facilities Network (www.mrfn.org). This research used resources of the Advanced Light Source, which is a U.S. Department of Energy Office of Science User Facility under contract no. DE-AC02-05CH11231. Use was made of computational facilities purchased with funds from the National Science Foundation (CNS-1725797) and administered by the Center for Scientific Computing (CSC). The CSC is supported by the California NanoSystems Institute and the Materials Research Science and Engineering Center (MRSEC; NSF DMR 1720256) at UC Santa Barbara. E.M.T. gratefully acknowledges support from the NSF Graduate Fellowship (DGE-1650114). The authors thank Nicole Schauser and Beihang Yu for initial scattering experiments and Tom Mates for assistance in XPS analysis.

5.6 Appendix D

5.6.1 FTIR of pristine PBTTT/IL

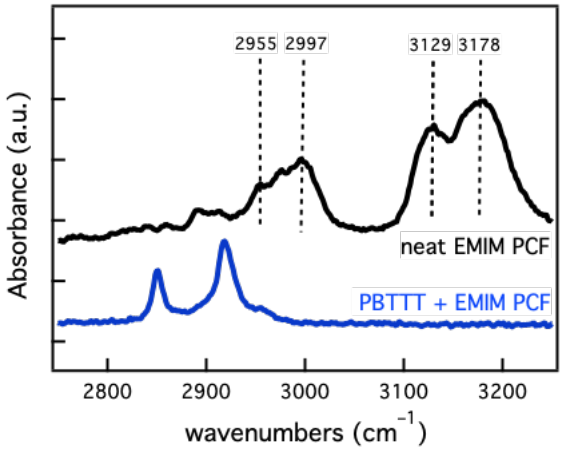

Figure D1. IR spectra of neat EMIM PCF (black trace) and a neat PBTTT film exposed to the ionic liquid for 5 minutes (blue trace). Features corresponding to the imidazolium ring in EMIM+ are not visible in the blue trace, which indicates that cations do not penetrate the film in its undoped state.

5.6.2 Full XPS survey spectra of doped and exchanged films

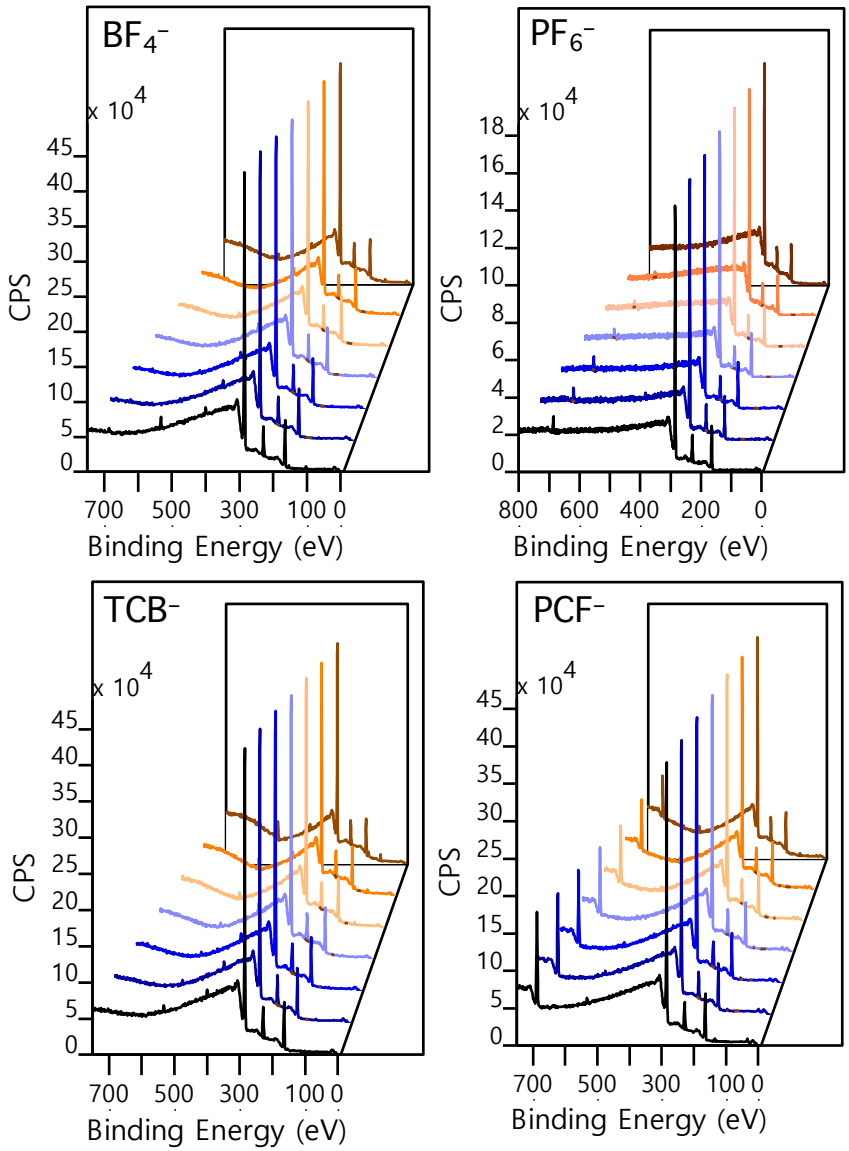

Figure D2. Depth-profiled XPS spectra of doped and counter-ion exchanged films. The atomic concentration of silicon served as the delineation between the film and underlying substrate.

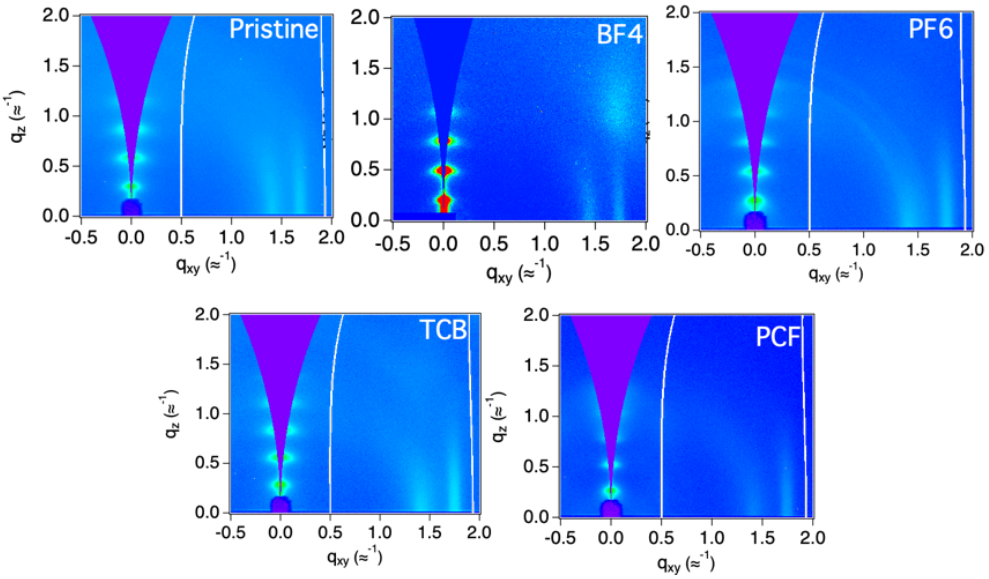

Figure D3. 2D GIWAXS images of pristine, doped, and counter-ion exchanged films.

5.7 References

(1) Jacobs, I. E.; Moulé, A. J. Controlling Molecular Doping in Organic Semiconductors. *Advanced Materials* **2017**, *29* (42), 1703063. https://doi.org/10.1002/adma.201703063.

(2) Han, C. C.; Elsenbaumer, R. L. Protonic Acids: Generally Applicable Dopants for Conducting Polymers. *Synthetic Metals* **1989**, *30* (1), 123–131. https://doi.org/10.1016/0379-6779(89)90648-6.

(3) Hofmann, A. I.; Kroon, R.; Yu, L.; Müller, C. Highly Stable Doping of a Polar Polythiophene through Co-Processing with Sulfonic Acids and Bistriflimide. *J. Mater. Chem. C* **2018**, *6* (26), 6905–6910. https://doi.org/10.1039/C8TC01593G.

(4) White, H. S.; Kittlesen, G. P.; Wrighton, M. S. Chemical Derivatization of an Array of Three Gold Microelectrodes with Polypyrrole: Fabrication of a Molecule-Based Transistor. *J. Am. Chem. Soc.* **1984**, *106* (18), 5375–5377. https://doi.org/10.1021/ja00330a070.

(5) Scholes, D. T.; Hawks, S. A.; Yee, P. Y.; Wu, H.; Lindemuth, J. R.; Tolbert, S. H.; Schwartz, B. J. Overcoming Film Quality Issues for Conjugated Polymers Doped with F $_4$ TCNQ by Solution Sequential Processing: Hall Effect, Structural, and Optical Measurements. *The Journal of Physical Chemistry Letters* **2015**, *6* (23), 4786–4793. https://doi.org/10.1021/acs.jpclett.5b02332.

(6) Mazaheripour, A.; Thomas, E. M.; Segalman, R. A.; Chabinyc, M. L. Nonaggregating Doped Polymers Based on Poly(3,4-Propylenedioxythiophene). *Macromolecules* **2019**, *52* (5), 2203–2213. https://doi.org/10.1021/acs.macromol.8b02389.

(7) Jacobs, I. E.; Aasen, E. W.; Oliveira, J. L.; Fonseca, T. N.; Roehling, J. D.; Li, J.; Zhang, G.; Augustine, M. P.; Mascal, M.; Moulé, A. J. Comparison of Solution-Mixed and Sequentially Processed P3HT:F4TCNQ Films: Effect of Doping-Induced Aggregation on Film Morphology. *J. Mater. Chem. C* **2016**, *4* (16), 3454–3466. https://doi.org/10.1039/C5TC04207K.

(8) Chiang, C. K.; Fincher, C. R.; Park, Y. W.; Heeger, A. J.; Shirakawa, H.; Louis, E. J.; Gau, S. C.; MacDiarmid, A. G. Electrical Conductivity in Doped Polyacetylene. *Phys. Rev. Lett.* **1977**, *39* (17), 1098–1101. https://doi.org/10.1103/PhysRevLett.39.1098.
(9) Lüssem, B.; Riede, M.; Leo, K. Doping of Organic Semiconductors. *physica status solidi (a)* **2013**, *210* (1), 9–43. https://doi.org/10.1002/pssa.201228310.
(10) Salzmann, I.; Heimel, G.; Oehzelt, M.; Winkler, S.; Koch, N. Molecular Electrical Doping of Organic Semiconductors: Fundamental Mechanisms and Emerging Dopant Design Rules. *Accounts of Chemical Research* **2016**, *49* (3), 370–378. https://doi.org/10.1021/acs.accounts.5b00438.
(11) Patel, S. N.; Glaudell, A. M.; Kiefer, D.; Chabinyc, M. L. Increasing the Thermoelectric Power Factor of a Semiconducting Polymer by Doping from the Vapor Phase. *Acs Macro Lett* **2016**, *5*, 268–272. https://doi.org/10.1021/acsmacrolett.5b00887.
(12) Lim, E.; Glaudell, A. M.; Miller, R.; Chabinyc, M. L. The Role of Ordering on the Thermoelectric Properties of Blends of Regioregular and Regiorandom Poly(3-Hexylthiophene). *Adv. Electron. Mater.* **2019**, 1800915. https://doi.org/10.1002/aelm.201800915.
(13) Yamamoto, J.; Furukawa, Y. Electronic and Vibrational Spectra of Positive Polarons and Bipolarons in Regioregular Poly(3-Hexylthiophene) Doped with Ferric Chloride. *The Journal of Physical Chemistry B* **2015**, *119* (13), 4788–4794. https://doi.org/10.1021/jp512654b.
(14) Vijayakumar, V.; Zhong, Y.; Untilova, V.; Bahri, M.; Herrmann, L.; Biniek, L.; Leclerc, N.; Brinkmann, M. Bringing Conducting Polymers to High Order: Toward Conductivities beyond 105 S Cm−1 and Thermoelectric Power Factors of 2 MW M−1 K−2. *Advanced Energy Materials* **2019**, *9* (24), 1900266. https://doi.org/10.1002/aenm.201900266.
(15) Thomas, E. M.; Davidson, E. C.; Katsumata, R.; Segalman, R. A.; Chabinyc, M. L. Branched Side Chains Govern Counterion Position and Doping Mechanism in Conjugated Polythiophenes. *ACS Macro Lett.* **2018**, 1492–1497. https://doi.org/10.1021/acsmacrolett.8b00778.
(16) Noriega, R.; Rivnay, J.; Vandewal, K.; Koch, F. P. V.; Stingelin, N.; Smith, P.; Toney, M. F.; Salleo, A. A General Relationship between Disorder, Aggregation and Charge Transport in Conjugated Polymers. *Nature Materials* **2013**, *12* (11), 1038–1044. https://doi.org/10.1038/nmat3722.
(17) Salzmann, I.; Heimel, G.; Duhm, S.; Oehzelt, M.; Pingel, P.; George, B. M.; Schnegg, A.; Lips, K.; Blum, R.-P.; Vollmer, A.; et al. Intermolecular Hybridization Governs Molecular Electrical Doping. *Physical Review Letters* **2012**, *108* (3). https://doi.org/10.1103/PhysRevLett.108.035502.
(18) Nikolka, M.; Nasrallah, I.; Rose, B.; Ravva, M. K.; Broch, K.; Sadhanala, A.; Harkin, D.; Charmet, J.; Hurhangee, M.; Brown, A.; et al. High Operational and Environmental Stability of High-Mobility Conjugated Polymer Field-Effect Transistors through the Use of Molecular Additives. *Nature Materials* **2017**, *16* (3), 356–362. https://doi.org/10.1038/nmat4785.
(19) Spano, F. C. Modeling Disorder in Polymer Aggregates: The Optical Spectroscopy of Regioregular Poly(3-Hexylthiophene) Thin Films. *J. Chem. Phys.* **2005**, *122* (23), 234701. https://doi.org/10.1063/1.1914768.

(20) Spano, F. C.; Silva, C. H- and J-Aggregate Behavior in Polymeric Semiconductors. *Annual Review of Physical Chemistry* **2014**, *65* (1), 477–500. https://doi.org/10.1146/annurev-physchem-040513-103639.
(21) Pochas, C. M.; Spano, F. C. New Insights on the Nature of Two-Dimensional Polarons in Semiconducting Polymers: Infrared Absorption in Poly(3-Hexylthiophene). *J. Chem. Phys.* **2014**, *140* (24), 244902. https://doi.org/10.1063/1.4882696.
(22) Ghosh, R.; Chew, A. R.; Onorato, J.; Pakhnyuk, V.; Luscombe, C. K.; Salleo, A.; Spano, F. C. Spectral Signatures and Spatial Coherence of Bound and Unbound Polarons in P3HT Films: Theory Versus Experiment. *J. Phys. Chem. C* **2018**, *122* (31), 18048–18060. https://doi.org/10.1021/acs.jpcc.8b03873.
(23) Ghosh, R.; Luscombe, C. K.; Hambsch, M.; Mannsfeld, S. C. B.; Salleo, A.; Spano, F. C. Anisotropic Polaron Delocalization in Conjugated Homopolymers and Donor–Acceptor Copolymers. *Chem. Mater.* **2019**, *31* (17), 7033–7045. https://doi.org/10.1021/acs.chemmater.9b01704.
(24) Scholes, D. T.; Yee, P. Y.; Lindemuth, J. R.; Kang, H.; Onorato, J.; Ghosh, R.; Luscombe, C. K.; Spano, F. C.; Tolbert, S. H.; Schwartz, B. J. The Effects of Crystallinity on Charge Transport and the Structure of Sequentially Processed F4TCNQ-Doped Conjugated Polymer Films. *Advanced Functional Materials* **2017**, *27* (44), 1702654. https://doi.org/10.1002/adfm.201702654.
(25) Aubry, T. J.; Axtell, J. C.; Basile, V. M.; Winchell, K. J.; Lindemuth, J. R.; Porter, T. M.; Liu, J.-Y.; Alexandrova, A. N.; Kubiak, C. P.; Tolbert, S. H.; et al. Dodecaborane-Based Dopants Designed to Shield Anion Electrostatics Lead to Increased Carrier Mobility in a Doped Conjugated Polymer. *Advanced Materials* **2019**, *31* (11), 1805647. https://doi.org/10.1002/adma.201805647.
(26) Yamashita, Y.; Tsurumi, J.; Ohno, M.; Fujimoto, R.; Kumagai, S.; Kurosawa, T.; Okamoto, T.; Takeya, J.; Watanabe, S. Efficient Molecular Doping of Polymeric Semiconductors Driven by Anion Exchange. *Nature* **2019**, *572* (7771), 634–638. https://doi.org/10.1038/s41586-019-1504-9.
(27) Bao, Z.; Dodabalapur, A.; Lovinger, A. J. Soluble and Processable Regioregular Poly(3-hexylthiophene) for Thin Film Field-effect Transistor Applications with High Mobility. *Applied Physics Letters* **1996**, *69* (26), 4108–4110. https://doi.org/10.1063/1.117834.
(28) Patel, S. N.; Glaudell, A. M.; Peterson, K. A.; Thomas, E. M.; O'Hara, K. A.; Lim, E.; Chabinyc, M. L. Morphology Controls the Thermoelectric Power Factor of a Doped Semiconducting Polymer. *Science Advances* **2017**, *3* (6), e1700434. https://doi.org/10.1126/sciadv.1700434.
(29) Lazzaroni, R.; Lögdlund, M.; Stafström, S.; Salaneck, W. R.; Brédas, J. L. The Poly-3-hexylthiophene/NOPF $_6$ System: A Photoelectron Spectroscopy Study of Electronic Structural Changes Induced by the Charge Transfer in the Solid State. *The Journal of Chemical Physics* **1990**, *93* (6), 4433–4439. https://doi.org/10.1063/1.458725.
(30) Xuan, Y.; Liu, X.; Desbief, S.; Leclère, P.; Fahlman, M.; Lazzaroni, R.; Berggren, M.; Cornil, J.; Emin, D.; Crispin, X. Thermoelectric Properties of Conducting Polymers: The Case of Poly(3-Hexylthiophene). *Phys. Rev. B* **2010**, *82* (11), 115454. https://doi.org/10.1103/PhysRevB.82.115454.

(31) Sato, N.; Kigoshi, A. The Sublimation of Some Metal Fluoride Complexes at Elevated Pressures. *Thermochimica Acta* **1981**, *47* (3), 253–260. https://doi.org/10.1016/0040-6031(81)80104-9.
(32) Mcculloch I; Heeney, M.; Bailey, C.; Genevicius, K.; Macdonald I; Shkunov, M.; Sparrowe, D.; Tierney, S.; Wagner, R.; Zhang, W. M.; et al. Liquid-Crystalline Semiconducting Polymers with High Charge-Carrier Mobility. *Nat Mater* **2006**, *5*, 328–333. https://doi.org/10.1038/nmat1612.
(33) Szakal, C.; Sun, S.; Wucher, A.; Winograd, N. C60 Molecular Depth Profiling of a Model Polymer. *Applied Surface Science* **2004**, *231–232*, 183–185. https://doi.org/10.1016/j.apsusc.2004.03.113.
(34) Nobuta, T.; Ogawa, T. Depth Profile XPS Analysis of Polymeric Materials by C60+ Ion Sputtering. *J Mater Sci* **2009**, *44* (7), 1800–1812. https://doi.org/10.1007/s10853-009-3274-5.
(35) Cendra, C.; Giovannitti, A.; Savva, A.; Venkatraman, V.; McCulloch, I.; Salleo, A.; Inal, S.; Rivnay, J. Role of the Anion on the Transport and Structure of Organic Mixed Conductors. *Advanced Functional Materials* **2019**, *41* (3), 1807034. https://doi.org/10.1002/adfm.201807034.
(36) Kiefer, J.; Fries, J.; Leipertz, A. Experimental Vibrational Study of Imidazolium-Based Ionic Liquids: Raman and Infrared Spectra of 1-Ethyl-3-Methylimidazolium Bis(Trifluoromethylsulfonyl)Imide and 1-Ethyl-3-Methylimidazolium Ethylsulfate. *Appl Spectrosc* **2007**, *61* (12), 1306–1311. https://doi.org/10.1366/000370207783292000.
(37) Liu, W.; Müller, L.; Ma, S.; Barlow, S.; Marder, S. R.; Kowalsky, W.; Köhn, A.; Lovrincic, R. Origin of the π–π Spacing Change upon Doping of Semiconducting Polymers. *J. Phys. Chem. C* **2018**, *122* (49), 27983–27990. https://doi.org/10.1021/acs.jpcc.8b10845.
(38) Miller, N. C.; Cho, E.; Gysel, R.; Risko, C.; Coropceanu, V.; Miller, C. E.; Sweetnam, S.; Sellinger, A.; Heeney, M.; McCulloch, I.; et al. Factors Governing Intercalation of Fullerenes and Other Small Molecules Between the Side Chains of Semiconducting Polymers Used in Solar Cells. *Advanced Energy Materials* **2012**, *2* (10), 1208–1217. https://doi.org/10.1002/aenm.201200392.
(39) Druy, M. A. The Role of the Counterion in the Reactivity of Conducting Polymers. *Synthetic Metals* **1986**, *15* (2), 243–248. https://doi.org/10.1016/0379-6779(86)90030-5.
(40) Levason, W.; Pugh, D.; Reid, G. Imidazolium-Based Ionic Liquids with Large Weakly Coordinating Anions. *New J. Chem.* **2017**, *41* (4), 1677–1686. https://doi.org/10.1039/C6NJ03674K.
(41) Hexemer, A.; Bras, W.; Glossinger, J.; Schaible, E.; Gann, E.; Kirian, R.; MacDowell, A.; Church, M.; Rude, B.; Padmore, H. A SAXS/WAXS/GISAXS Beamline with Multilayer Monochromator. *Journal of Physics: Conference Series* **2010**, *247*, 012007. https://doi.org/10.1088/1742-6596/247/1/012007.

Chapter 6

Failed experiments and what I learned from them

Most students who are granted a PhD are aware that 90 percent of the work that is completed, whether theoretical or experimental, is never published in a scientific journal. Through trial and error and a lot of failure, a student learns why things work one way and not another. It is the hope of these students (and their advisors) that younger labmates will not repeat the same mistakes and failed experiments of their predecessors.

This chapter details a few of the experiments that were unsuccessful and some tips for why some things were done the way they were. I maintain that if a journal existed to document such failed experiments, scientific progress would increase dramatically. However, until such a journal becomes mainstream, doctoral theses remain the harbor for these stories.

6.1 The danger of uncontrollable experiments

Part of attending graduate school is learning how to be someone who does good science, which is characterized by a few attributes. In good science, published results are repeatable, such that you can replicate your own measurements using your materials and instrumentation. These results should also be reproducible, such that if others had access to the same materials they would be able to get the same results. It is of utmost importance to develop protocols for your

own research that fit these requirements. Lack of reproducibility leads to a research community that lacks a sense of shared trust.

One study that highlights these difficulties is a project focusing on the effects of film crystallinity on mixed transport and thermoelectric properties. I chose the polymer poly[5,5'-bis(3-dodecyl-2-thienyl)-2,2'-bithiophene] (PQT-12) for this study. PQT-12 has a thiophene-based backbone with side chains on every two monomers, and was shown to exhibit high mobility in field-effect transistors.[1] One interesting feature about PQT-12 is its evolution in morphology upon quenching, which occurs with only a few conjugated homopolymers. This system seemed like an ideal choice to investigate, since the morphological changes could deconvolute the contributions of amorphous and crystalline regions to the thermoelectric power factor and charge mobility.

I chose several quenching conditions for films of PQT-12 that were available to me, with the most drastic temperature change being from annealing temperature (150 °C) to liquid nitrogen temperature (-196 °C). The quenching process was done in the glovebox by physically moving a film from the hot plate to a cold finger chamber in the glovebox floor, a glovebox freezer (-37 °C), and the uncooled glovebox floor (25 °C). **Figure 6.1** shows how the X-ray scattering pattern evolved with quenching versus a slow cool on the hot plate.

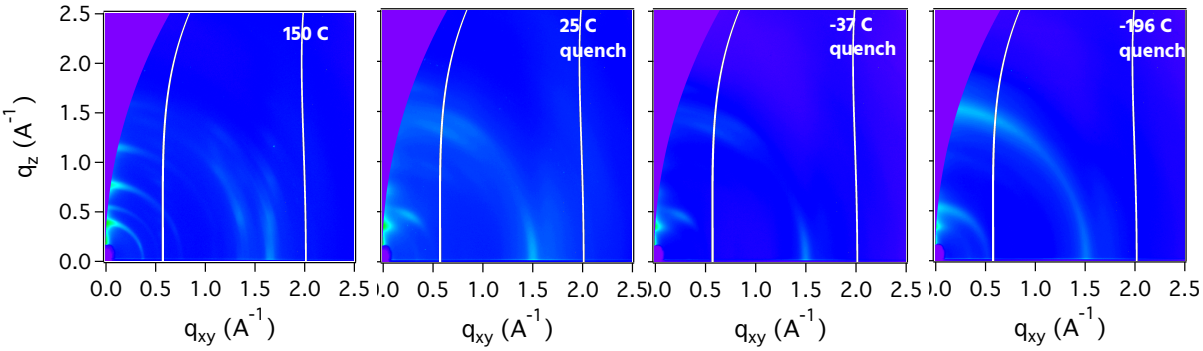

Figure 6.1. 2D GIWAXS images of PQT-12 films with different processing conditions. The first is a film slow cooled on the hot plate after annealing at 150 °C. Others were annealed at 150 °C for 10 minutes followed by quenching to 25 °C, -37 °C, and -196 °C.

I realized that a simple quenching experiment turned out be more complicated that I had envisioned. The scattering patterns show that quenching drastically modified the crystalline structure, with many of the higher order peaks visible in the slowly cooled sample not visible in the liquid-nitrogen quenched sample. The sample also became less textured with vitrification. There appear to be scattering peaks corresponding to different sets of unit cells, the population of which seems to be changing with quenching temperature. These unit cells have been identified as polymorphs in more recent literature on PQT-12.[2,3]

It was clear after a few months that a well-controlled study would be difficult with PQT-12, stemming from issues of repeatability and the formation of polymorphs with quenching. The kinetics of quenching is extremely important, so relying on manual techniques to quench will prevent straight-forward conclusions from being made. Additionally, it was necessary to consider the separate contributions of crystalline polymorphs to thermoelectric transport, rather than just amorphous and crystalline domains.

Although this project did not continue, there are several lessons that can be learned. The first lesson is the importance of identifying the correct system for the hypothesis you would like to test. If a current materials system is not ideal, it is useful to seek other systems that will generate more repeatable results. In my case, the polymer P3EHT in Chapter 2 crystallizes slowly over time without the formation of polymorphs, which shows promise for these types of studies. A more important lesson is knowing when to stop working on a project. That is a conversation to have between you and your advisor, which requires transparency

when you have doubts of the success for a given system. There is always something to learn through failure, which I share a few examples of in the next sections.

6.2 Electrochemical transistor fabrication

With devices that require several processing steps like transistors, many things can go wrong along the way. It is important to be methodical when troubleshooting an issue to identify the problem quickly. The PIL-based devices in Chapters 3 and 4 were made using different methods, each with their own set of intricacies. Some of the biggest hurdles that I came across in these studies are discussed below.

6.2.1 Top-gate-bottom-contact devices

The method of creating a transistor with the PIL-based dielectric atop the semiconductor can be fabricated from the bottom up, which involves fewer steps to completion. However, there remain a few difficulties that can be avoided.

6.2.1.1 The PIL solution must create a homogenous film atop the (nonpolar) semiconductor

It is imperative for any electrochemical transistor that the dielectric be homogenous at both the active channel/dielectric interface and the gate electrode/dielectric interface. For the devices in Chapter 4, the PIL solution was dropcast into a PDMS well that isolates the active layer. Typically, several layers are needed to fully cover the channel. If insufficient material is used, the PIL will segregate to the sides of the (more polar) PDMS well and not on the channel.

Important to creating a homogenous layer is slow evaporation of the solvent and a PIL T_G below the casting temperature. A polymer with low T_G is also beneficial to create a good contact with the top electrode upon lamination. In contrast, PILs with T_Gs above 70 °C are more amenable to gate electrode deposition through thermal evaporation, a feat that proves

to be more challenging with low-T_G polymers. Acetonitrile behaves well for casting since it does not dissolve most conjugated polymers and evaporates within ~5 minutes with slightly elevated temperatures (50-60 °C). Prior to pulling vacuum on the sample (to further dry the dielectric), be sure that most of the solvent has evaporated to avoid bubbling and surface roughening of the PIL layer.

6.2.1.2 Aging effects of devices

These transistors perform best when tested directly after being fabricated. Our observation is that after approximately one week in the glovebox, the devices will short and no longer be testable. This phenomenon is potentially due to a few reasons. Since the PIL used here is above its T_G at room temperature, segmental motion is possible at 25-30 °C. If the gate electrode rearranges such that it is in contact with another electrode, the device will short. Interfacial mixing between the semiconductor and dielectric is also possible, but difficult to probe with these devices.

Leaving the transistors in air for extended periods of time will degrade the device characteristics, as seen in more conventional organic FETs. It is postulated in our case that water uptake in the dielectric slows down the device, either because the ions are associating with water or from some contribution of water within the semiconductor.

6.2.2 Bottom-gate-top-contact transistors/operando devices

This method of transistor fabrication involves more steps than in Section 6.2.1, which makes things more complicated. Most of the challenges have been addressed through several rounds of trial and error. These, along with other tips to maximize fabrication success, are detailed below.

6.2.2.1 The semiconductor transfer method

This step took the most work to optimize. If you attempt to replicate this procedure, here are a few items you should keep in mind.

6.2.2.1.1 OTS treatment

A self-assembled monolayer (SAM) of octyltrichlorosilane (OTS) on the silicon substrate prior to spincasting the semiconductor modifies the surface energy to make the polymer more amenable to delamination. The detailed recipe is mainly credited to Michael Chabinyc from his time at the Palo Alto Research Center.

The procedure used in Chapter 3 used a 10 mM solution of octyltrichlorosilane (OTS) in hexadecane. Toluene works fine, but it will pick up water over time and polymerize the trichlorosilane which forms a white precipitate in the solution. If you see any white precipitates, even on the cap of the OTS, do not use it for this process. Store the OTS in the glovebox to increase its shelf life.

Hexadecane is ideal for this process since it does not evaporate quickly and does not pick up much water due to evaporative cooling (and solubility considerations). That said, a little bit of water is actually needed for the reaction; lab humidity is usually enough. There have been many papers written on the subject, but it should not be a concern unless you aim to achieve a perfect SAM. Prepare the solution in a glass petri dish and add the silicon substrates, ensuring that the solution fully covers each surface.

The reaction time for a chip is ~15 minutes depending on the concentration. Rinse the substrate well with hexane first (any nucleophilic solvent such as IPA or methanol will cause the residual trichlorsilane solution to polymerize). After a hexane wash, rinsing in acetone serves as a quality check to ensure the SAM formed. IPA should be the final rinse of the substrates. Dry quickly with an air or nitrogen gun.

The substrate should look the same before and after the OTS treatment. If the silicon looks cloudy or there are streaks on the surface, there may be some polymerized OTS on the surface and the SAM is likely not high quality. This could also occur if you used old acetone or IPA.

6.2.2.1.2 Transferring the semiconductor

Once the semiconductor is spincast on the treated substrate (followed by any necessary thermal treatment for the polymer), the thin film is ready to be transferred. PDMS is used as a transfer agent since it has a lower water contact angle than the SAM, making it a preferred surface for the semiconductor.[4] PDMS can also be readily made with materials available commercially. For measurements in Chapter 3, we used PDMS with 15-20% of the crosslinking agent by weight. PDMS with higher crosslinking is difficult to work with and more flexible PDMS is less successful at delaminating films. Letting the mixture sit overnight should be sufficient time for the crosslinking reaction to complete, but humidity >50% slows this process.

For best results, scratch the film edges to define a clear area of film for transferring. Laminate the stamp from one edge to another, avoiding the formation of bubbles. From one corner of the stamp, slowly lift the PDMS from the substrate. If you notice one corner is not coming with the PDMS, try another corner or apply a slight pressure. Try not to bend the PDMS too much during transfer as that can induce cracks in the film. Relaminate on the desired surface, continuing to avoid the formation of bubbles, and slowly remove the PDMS.

It should be noted that this process does not work for all polymeric semiconductors. It seems that if the film is too crystalline, the small amount of mechanical strain from the PDMS stamping will induce too many cracks for a functional device. Amorphous regions

within a semicrystalline film alleviate these issues. As a result, P3HT was used as the active layer in Chapter 3, rather than PBTTT, which suffered from these issues. Previous publications have also used PQT-12 successfully with this transfer method.[4]

6.2.2.2 Source/drain contacts

The distance between the source and drain contacts is important to consider for operando measurements. Scattering from any metal will dominate the 2D pattern captured by the detector, as scattering from polymeric crystallites is much weaker in comparison. As a result, the channel length must be sufficiently large as to not have the beam encounter the gold contacts on its path to the detector. The gradual channel approximation also dictates that the ratio of channel width to length (W/L) should be > 10.[5]

The critical minimal channel length depends on X-ray footprint. In the grazing geometry, there is some degree of beam spreading along the sample in the x and y direction that depends on the incident angle.[6] For the typical spot sizes of synchrotron hard X-rays, and remining within the constraints of the W/L requirement, the channel length/width was designed to be 2 mm/10 mm. This length gave us about ± 0.5 mm to avoid any dust or other defects in the active layer.

6.2.2.3 Transparent gold contacts

Spectroscopy is an important method to determine how carriers are distributed within the semiconductor. It was critical for the results in Chapter 3 to run devices in conjunction with transmission UV-Vis measurements. Our goal was to make the UV-Vis device as similar to the actual transistor as possible; as a result, we opted for thin gold as the electrodes rather than ITO, which is less stable electrochemically. Gold is not typically considered a transparent conductor, so it was important to balance the transmission properties with the resistance.

Figure 6.2 describes the trend of electrical resistivity as a function of gold thickness. A film thickness of between 6 and 8 nm is sufficient to obtain resistance values comparable with bulk gold resistivity.[7] The devices in Chapter 3 used substrates with 10 nm of gold that were conductive but also allowed transmission measurements to take place (with the proper blanking procedures prior to taking data). Many thanks for Hidenori Nakayama for the help in providing this reference.

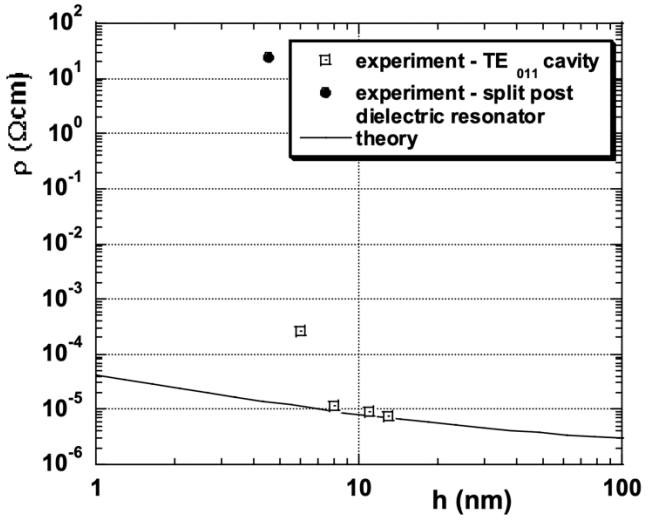

Figure 6.2. gold resistivity as a function of film thickness. Reproduced with permission from ref. 7.

6.3 Difficulties in chemical doping

Two of the projects in my dissertation centered around doping polymers *via* vapor phase infiltration. Vapor doping has several advantages over other doping methods, including eliminating the use of solvents after casting and controlling morphology of the pristine film prior to doping. However, there are still aspects of improvement that should be addressed in future studies.

The current doping setup comprises a 4-ounce glass jar (ThermoFischer) on a hot plate in an N_2-glovebox. Double-sided tape is used to affix substrates to the underside of the lid, and 3-5 mg of the dopant is placed at the bottom of the jar. The sealed jar is placed on the hot plate for several minutes before being removed. In this case, time on the hot plate is the independent variable.

The biggest shortcoming of this setup is the necessity for an additional characterization tool to calculate the doping level in the film. The most straightforward method for this has been UV-Vis spectroscopy, as it is a widely-available technique for laboratories around the world. To use UV-Vis for calculating doping level, the dopant anion must absorb either visible or ultraviolet light, and its extinction coefficient must be known. F_4TCNQ has worked for this protocol, and UV-Vis spectra of the anion have been obtained in previous works from either the salt form[8] or through taking advantage of cross-polarizers in doped polymeric films.[9] With the spectra of the doped film and the spectra of the dopant anion, one can use Beer's Law to calculate the doping level and the carrier concentration.

F_4TCNQ is an ideal case for this application because of the unique anion absorption at 1.4 and 1.6 eV. Most other dopants do not have an anion absorption in the ultraviolet or visible spectrum, and other methods must be used. Other techniques to determine doping level include X-ray photoelectron spectroscopy[10] and quartz crystal microbalance (QCM) measurements.[11] QCM has significant advantages as it can be integrated into a doping chamber such that doping level can potentially be measured *in situ*.

Improvements for a more controlled vapor doping setup include temperature control of the substrate and QCM integration for qualitative monitoring of doping level. One route for an improved design is to integrate a QCM head in the plane of the substrates within the

doping chamber. Since the accuracy of the of the quartz crystal reading decreases with elevated temperatures, active cooling of the chamber top must be employed. Certain limitations still remain with this method since the amount of dopant within the film does not always equate with the number of electronic carriers. A calibration curve should be generated to track the doping efficiency with total amount of dopant present for a given temperature.

6.4 Sample preparation details that are important to consider

6.4.1 FTIR

Not all substrates exhibit the same degree of transparency in the infrared. Additionally, not all substrates are the same price or may be reactive with your sample. Depending on the range of wavenumbers that you are interested in probing, different substrates will work better than others. **Figure 6.3** contains a few examples of FTIR substrates typically used for transmission measurements.

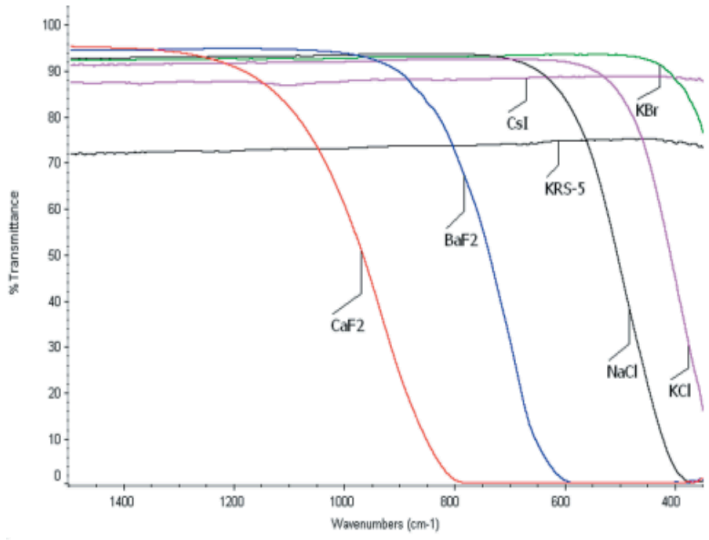

Figure 6.3. Transmittance of common FTIR substrates as a function of wavenumber. Used with permission from ref. 12.

KBr exhibits the greatest degree of transparency from the 1500 – 400 cm^{-1} range, and was used for results shown in Chapters 2 and 5. One drawback of using KBr is its tendency to uptake water, which clouds the substrate if left in air. These and other factors, such as the chemical sensitivity of a sample, are crucial to consider for high quality results.

6.4.2 RSoXS

Silicon nitride (Si_3N_4) is a common material for transmission RSoXS due to its transparency to the X-ray beam. In reality, there is some fraction of incident X-rays that the substrate absorbs; this fraction depends on the energy of the X-ray and the thickness of the window. For instance, **Figure 6.4** shows the fraction of light transmitted for a Si_3N_4 window that is 100 nm thick:

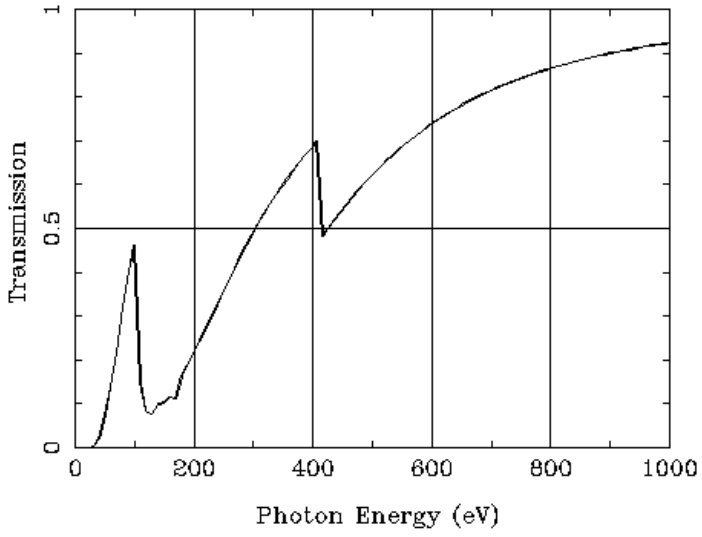

Figure 6.4. Percentage of X-rays transmitted with photon energy of a blank 100 nm-thick Si_3N_4 window. Generated from the Center for X-ray Optics through Lawrence Berkeley National Laboratory.

Figure 6.4 demonstrates that near the carbon edge (~ 300 eV), a relevant energy range for polymers, 50% of incident light is absorbed through the window. Doubling the Si_3N_4 thickness decreases the fraction of transmitted light to 20% at 300 eV. Thinner Si_3N_4 windows exist but are quite fragile and hard to work with. Decreasing the window dimensions can prevent the substrate from cracking but increases the chance of shadowing effects from the window edges on the 2D pattern. Our group has historically found that 1.5 × 1.5 mm, 100 nm windows offer the optimal balance of signal to mechanical stability.

These principles apply to the sample as well as the substrate. For scattering at the carbon edge, it is necessary for samples to be no thicker than 1 μm, but ideally between 50 – 200 nm. This requires most samples to be spuncast rather than dropcast. This requirement presents a unique problem in doped semiconductors if it is desired to look at scattering of molecules other than the polymer. Since dopants are usually > 4× less abundant in the film than the polymer, attempts to get scattering at different edges, such as the nitrogen or fluorine, are difficult. Modifications such as tilting the sample to increase the amount of material that the beam interacts with have proven to be somewhat successful. Dropcasting samples have potential for studies on ordering of dopants at binding energies other than the carbon edge, since higher energies have a larger penetration depth in the sample and can interact with more dopant molecules in the thicker film.

6.5 References

(1) Jimison, L. H.; Salleo, A.; Chabinyc, M. L.; Bernstein, D. P.; Toney, M. F. Correlating the Microstructure of Thin Films of Poly[5,5-Bis(3-Dodecyl-2-Thienyl)-2,2-Bithiophene] with Charge Transport: Effect of Dielectric Surface Energy and Thermal Annealing. *Phys. Rev. B* **2008**, *78* (12), 125319. https://doi.org/10.1103/PhysRevB.78.125319.

(2) Grigorian, S.; Escoubas, S.; Ksenzov, D.; Duche, D.; Aliouat, M.; Simon, J.-J.; Bat-Erdene, B.; Allard, S.; Scherf, U.; Pietsch, U.; et al. A Complex Interrelationship between Temperature-Dependent Polyquaterthiophene (PQT) Structural and Electrical Properties. *J. Phys. Chem. C* **2017**, *121* (41), 23149–23157. https://doi.org/10.1021/acs.jpcc.7b02489.

(3) Kang, S.-J.; Song, S.; Liu, C.; Kim, D.-Y.; Noh, Y.-Y. Evolution in Crystal Structure and Electrical Performance of Thiophene-Based Polymer Field Effect Transistors: A Remarkable Difference between Thermal and Solvent Vapor Annealing. *Organic Electronics* **2014**, *15* (9), 1972–1982. https://doi.org/10.1016/j.orgel.2014.05.026.

(4) Chabinyc, M. L.; Salleo, A.; Wu, Y.; Liu, P.; Ong, B. S.; Heeney, M.; McCulloch, I. Lamination Method for the Study of Interfaces in Polymeric Thin Film Transistors. *Journal of the American Chemical Society* **2004**, *126* (43), 13928–13929. https://doi.org/10.1021/ja044884o.

(5) Zaumseil, J.; Sirringhaus, H. Electron and Ambipolar Transport in Organic Field-Effect Transistors. *Chem. Rev.* **2007**, *107* (4), 1296–1323. https://doi.org/10.1021/cr0501543.

(6) Smilgies, D.-M. Scherrer Grain-Size Analysis Adapted to Grazing-Incidence Scattering with Area Detectors. *J Appl Crystallogr* **2009**, *42* (Pt 6), 1030–1034. https://doi.org/10.1107/S0021889809040126.

(7) Zychowicz, T.; Krupka, J.; Mazierska, J. Measurements of Conductivity of Thin Gold Films at Microwave Frequencies Employing Resonant Techniques. In *2006 Asia-Pacific Microwave Conference*; 2006; pp 572–574. https://doi.org/10.1109/APMC.2006.4429490.

(8) Kiefer, D.; Kroon, R.; Hofmann, A. I.; Sun, H.; Liu, X.; Giovannitti, A.; Stegerer, D.; Cano, A.; Hynynen, J.; Yu, L.; et al. Double Doping of Conjugated Polymers with Monomer Molecular Dopants. *Nat. Mater.* **2019**, *18* (2), 149–155. https://doi.org/10.1038/s41563-018-0263-6.

(9) Hamidi-Sakr, A.; Biniek, L.; Bantignies, J.-L.; Maurin, D.; Herrmann, L.; Leclerc, N.; Lévêque, P.; Vijayakumar, V.; Zimmermann, N.; Brinkmann, M. A Versatile Method to Fabricate Highly In-Plane Aligned Conducting Polymer Films with Anisotropic Charge Transport and Thermoelectric Properties: The Key Role of Alkyl Side Chain Layers on the Doping Mechanism. *Adv. Funct. Mater.* **2017**, *27* (25), 1700173. https://doi.org/10.1002/adfm.201700173.

(10) Xuan, Y.; Liu, X.; Desbief, S.; Leclère, P.; Fahlman, M.; Lazzaroni, R.; Berggren, M.; Cornil, J.; Emin, D.; Crispin, X. Thermoelectric Properties of Conducting Polymers: The Case of Poly(3-Hexylthiophene). *Phys. Rev. B* **2010**, *82* (11), 115454. https://doi.org/10.1103/PhysRevB.82.115454.

(11) Méndez, H.; Heimel, G.; Opitz, A.; Sauer, K.; Barkowski, P.; Oehzelt, M.; Soeda, J.; Okamoto, T.; Takeya, J.; Arlin, J.-B.; et al. Doping of Organic Semiconductors: Impact of Dopant Strength and Electronic Coupling. *Angewandte Chemie International Edition* **2013**, *52* (30), 7751–7755. https://doi.org/10.1002/anie.201302396.

(12) Pike Technologies. Crystal Selection for Transmission Sampling.

Chapter 7

Conclusions and Future Outlook

In summary, this Dissertation demonstrates the importance of dopant counter-ions on the behavior of doped polymeric semiconductors, from the molecular-scale interactions to its effects on the crystalline structure and device-scale electron mobility. A variety of doping methods were used in this work to elucidate these fundamental mechanisms, and we believe that the conclusions herein apply to a broad range of semiconducting polymers.

Chapter 2 focused on a comparison of two prototypical semiconductors to explore the impact of steric hindrance on the doping mechanism in semiconducting polymers. We found that introducing a degree of steric hindrance from a branched side chain chemistry can lead to two forms of charge transfer (integer charge transfer versus charge transfer complex) with the same oxidative dopant and semiconducting backbone. This role of steric hindrance on the formation of a charge transfer complex has implications for low-voltage loss organic solar cells, where donor:acceptor complexes are the sites of charge generation and recombination.

Chapter 3 detailed a study on the correlation of structural changes observed in doped polymeric semiconductors and the measured carrier mobility. We found that the distribution of ions in poly(3-hexylthiophene), a model semicrystalline semiconducting polymer, is not heterogeneous, and the structural changes that ion infiltration induces has a large impact on its electronic properties. The dopant-induced morphological changes of P3HT rationalize the

dependence of mobility on carrier concentration and suggests that the doped polymer should be considered as a distinct phase from the neutral polymer.

Chapter 4 summarized our work on how infiltration of ions during doping modifies the electronic density of states (DOS) of semiconducting polymers. The DOS of semiconducting polymers sets the energetic landscape that carriers move through during electrical transport. Using thermopower measurements, we found that the electronic DOS broadens with increasing carrier density in a semiconducting polymer. The dopant-induced disorder at high carrier density rationalizes a widely observed power law relationship between thermopower and conductivity and suggests routes to increase the thermoelectric power factor in organic thermoelectrics by minimizing energetic disorder at high doping levels. Because the DOS broadens upon doping, there exists a balance between a well-defined electronic structure and high conductivity necessary for mixed conduction in thermoelectrics.

Chapter 5 introduced a platform to investigate the impact of Coulombic interactions on the electronic properties and thermal stability of doped polymers. Through exposing a doped film to a concentrated salt solution, the negatively-charged counter-ions within the doped film efficiently exchanged for the anion of the salt solution. The long-range order was not disrupted upon doping and counter-ion exchange. While infrared spectroscopy indicated that the distance between the dopant counter-ion and charge on the polymer increased with an increasing counter-ion diameter, these molecular interactions did not lead to an increased conductivity. We expect that since the morphology was not affected by these doping processes, the degree to which the long-range order of crystallites is what ultimately governs the transport properties at the macroscale. However, the dopant counter-ion ultimately governs doping stability at high temperatures, where films containing counter-ions with less labile

bonds remain conductive past 140 °C, in the range of critical thermal transitions of the host polymer.

While the studies detailed in this Dissertation answered a few questions regarding the importance of counter-ion/polaron interactions in doped semiconducting polymers, the results opened up several new questions and exciting new directions for the field. Characterization and synthetic advances will both be critical in guiding materials design for the intended applications at a commercial scale.

Side chain design is a unique avenue for imparting mixed conduction with control over ion position within the polymeric film. The use of alkyl-based side chains is an overwhelmingly popular choice for many commercially available semiconducting polymers today but is a relatively arbitrary choice with respect to other functional groups. Recently, ether-oxygen-containing side chains have been gaining popularity in the semiconducting polymer community. Studies show that polymers with EO-based side chains can be oxidized but remain soluble in a variety of solvents,[1] remain conductive to high temperatures,[2] and sustain di-anions of oxidative dopants.[3] EO- and imidazole-functionalized side chains have also found utility for ion conduction for lithium-based salts;[4] although the electronic mobility is lower in some cases than the non-functionalized equivalent, strategies are underway to utilize dual modes of conduction through these next-generation materials.

It is also important to explore the origin of changes in electrical properties to separate effects from energetic disorder and trap-filling and morphology. The carrier mobility of doped semiconducting polymers depends strongly on the carrier concentration due to changes in the Coulombic interaction between the carrier and its associated counter-ion. A powerful technique to probe ionic effects on the electronic structure of semiconductors at the mesoscale

is thermopower measurement. Chapter 4 focused on the idea that ionic effects drastically affects the DOS, and Chapter 5 indicates that the degree of interaction can be controlled by changing the dopant counter-ion of choice. Future studies can utilize these ideas to use thermopower as a tool to understand how the degree of interaction between ions and electrons impacts the electronic density of states. The thermopower of these polymers with different side chain chemistry, but at the same doping level, will yield how the density of states in the polymer is influenced by branch point proximity to the backbone.

Doped polymeric semiconductors will continue to be at the forefront of innovative technology, with improvement in air and temperature stability bringing these materials closer to viability at commercial scales. Synergistic efforts in simulation and synthetic strategies will ultimately be the key to rationalizing and predicting the complicated phenomena in these charged materials.

7.1 References

(1) Mazaheripour, A.; Thomas, E. M.; Segalman, R. A.; Chabinyc, M. L. Nonaggregating Doped Polymers Based on Poly(3,4-Propylenedioxythiophene). *Macromolecules* **2019**, *52* (5), 2203–2213. https://doi.org/10.1021/acs.macromol.8b02389.

(2) Kroon, R.; Kiefer, D.; Stegerer, D.; Yu, L.; Sommer, M.; Müller, C. Polar Side Chains Enhance Processability, Electrical Conductivity, and Thermal Stability of a Molecularly p-Doped Polythiophene. *Advanced Materials* **2017**, *29* (24), 1700930:1-7. https://doi.org/10.1002/adma.201700930.

(3) Kiefer, D.; Kroon, R.; Hofmann, A. I.; Sun, H.; Liu, X.; Giovannitti, A.; Stegerer, D.; Cano, A.; Hynynen, J.; Yu, L.; et al. Double Doping of Conjugated Polymers with Monomer Molecular Dopants. *Nat. Mater.* **2019**, *18* (2), 149–155. https://doi.org/10.1038/s41563-018-0263-6.

(4) Dong, B. X.; Nowak, C.; Onorato, J. W.; Strzalka, J.; Escobedo, F. A.; Luscombe, C. K.; Nealey, P. F.; Patel, S. N. Influence of Side-Chain Chemistry on Structure and Ionic Conduction Characteristics of Polythiophene Derivatives: A Computational and Experimental Study. *Chem. Mater.* **2019**, *31* (4), 1418–1429. https://doi.org/10.1021/acs.chemmater.8b05257.